



Democratic and People's Republic of Algeria
Ministry of Higher Education and Scientific
Research, University Echahid Cheikh Larbi Tebessi,
Tebessa.
Faculty of Natural Sciences and Life Sciences.
Department: Material Sciences.



Thesis
Presented for the graduation of PhD LMD
Stream: Physical
Option: Physics of materials

Submitted by
Boudiar Meriem.

12/11/ 2024

Theme

**Synthesis and characterization of thin films of metallic oxides
and pair oxides based on doped TiO₂.**

Jury:

Pr. Chemam Faïçal	President	Echahid Cheikh Larbi Tebessi University in Tebessa.
Dr. Hanini Faouzi	Rapporteur	Echahid Cheikh Larbi Tebessi University in Tebessa.
Dr. Kermiche Fouad	Examiner	The Higher Normal School of Setif.
Dr. Lakel Abdelghani	Examiner	University Mohamed Khider of Biskra.
Dr. Khechba Mourad	Examiner	Echahid Cheikh Larbi Tebessi University in Tebessa.

ملخص

تمت دراسة طبقات رقيقة من أكسيد وأكاسيد معدنية مبنية على TiO_2 المطعم باستخدام تقنيات متنوعة لدراسة خصائصها الهيكلية والبنية المجهرية والبصرية. تشمل طرق التوصيف المستخدمة حيود الأشعة السينية (XRD)، المجهر الإلكتروني الماسح (SEM)، مطيافية الأشعة فوق البنفسجية-المرئية (UV-Vis)، مطيافية الخط (MLS)، مجهر القوة الذرية (AFM)، مطيافية رامان (Raman)، ومطيافية الأشعة تحت الحمراء بتحويل فورييه (FTIR).

تم تحضير الطبقات الرقيقة من TiO_2 المطعم بالزنك باستخدام طريقة **محلول-هلام** وترسيبها على ركائز زجاجية بواسطة عملية الطلاء الدوراني، تليها معالجة حرارية عند 500 درجة مئوية لمدة 90 دقيقة. كشف تحليل حيود الأشعة السينية (DRX) للطبقات غير المطعم من TiO_2 عن تكوين طور الأناز مع المستوي (101) A كاتجاه مفضل. أدى زيادة تركيزات الزنك إلى تثبيط النمو البلوري في طبقات TiO_2 . أظهرت صور المجهر الإلكتروني الماسح (MEB) للطبقات غير المطعم و المطعم بالزنك من TiO_2 أن إضافة الزنك غيرت بشكل كبير البنية المجهرية للطبقات. تتميز الطبقات بنفاذية متوسطة تتراوح بين 70 إلى 90% في نطاق الأطوال الموجية من 350 إلى 900 نانومتر وفجوة بصرية بين 3.6 و 3.51 إلكترون فولت. أظهرت مطيافية خطوط (MLS) أن أدلة الموجات المستوية $Zn: TiO_2$ تدعم أنماطاً موجهة مقيدة بسيطة للاستقطابين TE و TM. أشارت قياسات MLS إلى أن تطعيم الزنك يزيد من معامل الانكسار، مما يحسن خصائص توجيه الموجات. بالإضافة إلى ذلك، تقل الأزواجية البصرية مع زيادة تركيز الزنك حتى 7% بالوزن.

بخصوص الطبقات الرقيقة من الأكسيد وأزواج الأكاسيد المعدنية القائمة على TiO_2 (CuO/TiO_2 & ZnO/TiO_2) التي تم تحضيرها باستخدام طريقة **محلول-هلام** (الطلاء الدوراني) عند درجة حرارة 500 درجة مئوية على ركائز من الزجاج والسليكون، فقد تم دراسة خصائصها الهيكلية وتحديدتها بواسطة تحليل مطيافية رامان. تزداد خشونة **Rms** لأزواج الأكاسيد المعدنية القائمة على TiO_2 ، مما يعني أن لديها سطحاً أكثر خشونة من أفلام TiO_2 . تكشف الملاحظات البصرية أن الطبقات الرقيقة من TiO_2 و ZnO و ZnO/TiO_2 تظهر نفاذية عالية تتراوح من 60 إلى 80%. في المقابل، تظهر الطبقات الرقيقة من CuO و CuO/TiO_2 نفاذية منخفضة. وأخيراً، تتراوح الفجوة البصرية للأفلام الرقيقة من الأكسيد وأزواج الأكاسيد المعدنية القائمة على TiO_2 من 3.69 إلى 4.05 إلكترون فولت.

الكلمات المفتاحية: محلول-هلام، أغشية $Zn:TiO_2$ ، حيود الأشعة السينية (XRD)، رامان، المجهر الإلكتروني الماسح (SEM)، مجهر القوة الذرية (AFM)، الأشعة فوق البنفسجية-المرئية (UV-Vis)، مقياس الطيف الضوئي بالأشعة تحت الحمراء (FTIR)، CuO/TiO_2 ، ZnO/TiO_2 .

Abstract

Thin films of metallic oxides and pair oxides based on doped TiO₂ have been characterized using various techniques to study their structural, microstructural, and optical properties. The characterization methods used include X-ray diffraction (XRD), scanning electron microscopy (SEM), ultraviolet-visible spectrophotometry (UV-Vis), M-line spectroscopy (MLS), atomic force microscopy (AFM), Raman spectroscopy (Raman), and Fourier transform infrared spectroscopy (FTIR).

The Zn doped TiO₂ thin films were prepared via the *Sol-Gel* method and deposited on glass substrates using the spin-coating process, followed by thermal treatment at 500°C for 90 minutes. XRD analysis of the undoped TiO₂ films revealed the formation of the anatase phase with the A (101) plane as the preferred orientation. Increasing zinc concentrations inhibited crystal growth in the TiO₂ films. SEM images of both undoped and Zn doped TiO₂ films showed that the addition of zinc significantly altered the microstructure of the TiO₂ films. The films exhibited an average transmittance of 70 to 90% in the wavelength range of 350 to 900 nm and an band gap between 3.6 and 3.51 eV. M-lines spectroscopy demonstrated that the Zn: TiO₂ planar waveguides support single confined guided modes for both TE and TM polarizations. MLS measurements indicated that zinc doping increases the refractive index, thereby enhancing their waveguiding properties. Additionally, birefringence decreases as the zinc concentration increases up to 7 % wt.

Regarding, the thin films of metallic oxides and pair oxides based on TiO₂ (ZnO, CuO, ZnO/TiO₂ and CuO/TiO₂) prepared by the *Sol-Gel* method (spin-coating) at 500 °C on glass and silicon substrates, their structural properties were studied and identified by Raman spectroscopy analysis. The *Rms* roughness values of thin films of metallic oxides and pair oxides based on TiO₂ were high, indicating that their surface is rougher compared to that of TiO₂ single films. Optical observations reveal that the thin films of TiO₂, ZnO, and ZnO/TiO₂ exhibit high transmittance, ranging from 60 to 80%. In contrast, the thin films of CuO and CuO/TiO₂ show low transmittance. Finally, the band gap of thin films of metallic oxides and pair oxides based on TiO₂ varies from 3.69 to 4.05 eV.

Keywords: Sol-Gel, Zn:TiO₂ films, XRD, Raman, SEM, AFM, UV-Vis, MLS, FTIR, ZnO/TiO₂, CuO/TiO₂.

Résumé

Des couches minces d'oxyde et de couple d'oxydes métalliques à base de TiO_2 dopé ont été caractérisées par diverses techniques pour étudier leurs caractéristiques structurales, microstructurelles et optiques. Les méthodes de caractérisation utilisées comprennent la diffraction des rayons X (DRX), la microscopie électronique à balayage (MEB), la spectrophotométrie ultraviolet-visible (UV-Vis), la spectroscopie M-line (MLS), la microscopie à force atomique (AFM), la spectroscopie Raman (Raman) et la spectroscopie infrarouge à transformée de Fourier (FTIR).

Les couches minces de TiO_2 dopés au zinc ont été préparées via la méthode *Sol-Gel* et déposés sur des substrats en verre par le procédé de spin-coating, suivis d'un traitement thermique à 500 °C pendant 90 minutes. Une analyse DRX des couches de TiO_2 non dopés a révélé la formation de la phase anatase avec le plan A (101) comme orientation préférée. L'augmentation des concentrations de zinc a inhibé la croissance cristalline dans les couches de TiO_2 . Les images MEB des couches de TiO_2 non dopés et dopés au zinc ont montré que l'ajout de zinc changeait significativement la microstructure des couches de TiO_2 . Les couches présentent une transmittance moyenne de 70 à 90% dans la gamme de longueurs d'onde de 350 à 900 nm et un gap optique entre 3,6 et 3,51 eV. La spectroscopie M-lines a démontré que les guides d'ondes plans Zn: TiO_2 supportent des modes guidés confinés simples pour les 02 polarisations TE et TM. Les mesures MLS ont indiqué que le dopage en zinc augmente l'indice de réfraction, en améliorant ainsi leurs propriétés de guidage d'ondes. De plus, la biréfringence diminue à mesure que la concentration de zinc augmente jusqu'à 7% wt.

Concernant, les couches minces d'oxyde et de couple d'oxydes métalliques à base de TiO_2 (ZnO/TiO_2 & CuO/TiO_2) préparées par la méthode *Sol-Gel* (spin-coating) à 500 °C sur des substrats en verre et en silicium, leurs propriétés structurales ont été étudiées et identifiées par analyse spectroscopie Raman. La rugosité *Rms* de couple d'oxydes métalliques à base de TiO_2 , augmente, ce qui signifie qu'ils ont une surface plus rugueuse que les films de TiO_2 . Les observations optiques révèlent que les couches minces de TiO_2 , ZnO et ZnO/TiO_2 présentent une haute transmittance, allant de 60 à 80 %. En revanche, les couches minces de CuO et CuO/TiO_2 montrent une faible transmittance. Enfin, le gap optique des films minces d'oxyde et de couple d'oxydes métalliques à base de TiO_2 varie de 3,69 à 4,05 eV.

Mots-clés: Sol-Gel, films Zn: TiO_2 , DRX, Raman, MEB, AFM, UV-Vis, MLS, FTIR, ZnO/TiO_2 , CuO/TiO_2 .

Dedication

I dedicate this work to:

- ✓ *My self,*
- ✓ *My parents, who have provided me with their encouragement, love, and understanding,*
- ✓ *My sisters and my brother, for their whole-hearted support,*
- ✓ *All my extended family,*
- ✓ *All my friends and teachers at the University of Tebessa,*
- ✓ *Everyone who has supported, cared for, and encouraged me, I dedicate this humble work to you.*

Acknowledgement

This thesis was conducted as part of a doctoral project in materials physics at Echahid Cheikh Larbi Tebessi University, Tebessa. First and foremost, I would like to express my gratitude to Almighty Allah for giving me the determination and courage to complete this work. My most sincere thanks go to my dear mother and my dear father, who have supported me throughout my life and given me the strength and determination to achieve this on my own.

The completion of this work owes immense gratitude to the multitude of individuals who generously offered their assistance and intellectual support during the four-year journey of my doctoral thesis. I am profoundly thankful to my supervisor, ***Faouzi Hanini***, whose guidance and encouragement were invaluable, for his help, support, and encouragement throughout every stage of this work. Despite his busy schedule, he consistently provided me with encouragement and advice. His availability made the thesis writing and revision process swift and efficient. His constant guidance and insightful instruction were crucial to the development of this thesis. It was a great pleasure for me to work with him.

I would also like to thank ***Professor. Chemam Faïçal***, a faculty member at Echahid Cheikh Larbi Tebessi University in Tebessa, for the honor of presiding over my thesis jury. I sincerely thank ***Dr. Fouad Kermiche***, a faculty member at the Higher Normal School of Setif, for agreeing to be on my thesis jury. I am sincerely grateful to ***Dr. Lakel Abdelghani***, a faculty member at the University Mohamed Khider of Biskra, for his willingness to serve on my thesis jury. I warmly thank ***Dr. Khechba Mourad***, a faculty member at Echahid Cheikh Larbi Tebessi University in Tebessa, for agreeing to be a member of my thesis jury.

We also want to thank all the people who guided, observed, helped, advised, and supported us with kindness throughout these years of study. We express our gratitude to everyone who contributed significantly to the success of this work. Whether for a long time, several years, or just a few months, many people have contributed to our growth. We thank them from the bottom of our hearts.

I wish to express my gratitude to all the people in the Laboratory of Applied and Theoretical Physics (LPAT).

List of contents

Introduction	1
<u>Chapitre I : Etude bibliographique</u>	
I. 1 Thin film	3
I. 2 Thin film formation	4
I. 3 Thin films growth modes	5
I.3.1. Volmer-Weber or island	6
I.3.2. Frank-van der Merwe	6
I.3.3. Stranski-Krastanov	7
I. 4 Thin film deposition techniques	7
I.4.1. Historical descriptions and recent compilations	7
I.4.2. Different PVD and CVD	9
I. 5 sol-gel	10
I.5.1. History and development of the sol-gel process	10
I.5.2. Hydrolysis and condensation reactions	11
I.5.2.1 Hydrolysis reactions	11
I.5.2.1 Condensation reactions	11
I.5.3. The Sol-Gel Process	13
I.5.4. The advantages of the sol-gel method	14
I.5.4. The disadvantages of the sol-gel methods	14
I. 6 Different sol-gel method	14
I.4.2. Spin-Coating	14
I.4.2. Dip coating	17
I. 7 Titanium dioxide	18
I. 8 Properties of TiO₂	19
I.8.1. Structural properties	19
I.8.2. Morphological properties	23
I.8.3. Optical properties	23
I.8.4. Electrical properties	24
I. 9 Applications of TiO₂	25
I.9.1. Current uses of TiO ₂	26

I.9.2. Potential Future Uses of TiO ₂	27
I. 10 Metal oxides	28
I.10.1. Synthesis of metal oxides	28
I.10.2. Applications of metal oxides	29
I.10.3. Bulk structure	29
I. 11 Doping of TiO₂	29
I. 12 Zinc oxide (ZnO)	30
I. 13 Coupling of TiO₂ with ZnO	31
I. 14 Copper oxide	32
I. 15 Iron Oxides	33
I. 16 Coupling of TiO₂ with Fe₂O₃	34
<i>Chapitre II : Nonlinear optics</i>	
II.1 Principles of Guidance and Multimodal Fiber	35
II.2 Nonlinear optics	36
II.3 Materials for nonlinear optics	39
II.4 Fiber characteristics	39
II.5 Nonlinear fiber optics	40
II.6 Origin of Nonlinear Effects in optical Fibers	42
II.7 Theory of Four-Wave Mixing	42
II.8 Single-Mode Fiber	44
<i>Chapitre III : Experimental Procedures</i>	
III. 1 Experimental protocols	45
III.1.1 Steps for Cleaning Substrates	47
1. Glass substrate	47
2. Si substrate	47
III. 2 Synthesis procedure thin films	47
III.2.1. Materials	47
III.2.2. Deposition by Sol-Gel	48
III.2.3. Synthesis of undoped TiO ₂ film	49
III.2.4. Synthesis of Zn-doped TiO ₂ films	49
III.2.5. Synthesis of metallic oxides and pair oxides based on TiO ₂ thin films	49

III.2.5.1. Preparation of ZnO, and CuO solutions	49
III. 3 Characterization of deposited thin films	51
III.3.1. X-ray Diffraction	51
III.3.1.1. Principle of XRD	51
III.3.2. Raman spectroscopy	54
III.3.2.1. Rayleigh scattering	55
III.3.2.2. Anti-Stokes Raman scattering	55
III.3.2.3. Stokes Raman scattering	55
III.3.3. UV–Vis spectroscopy	55
III.3.3.1. Optical phenomena of thin films	56
III.3.3.2. The index refraction	57
III.3.3.3. Band gap	58
III.3.3.3. calculation of the band gap	59
III.3.4. Fourier Transform Infrared Spectroscopy (FTIR)	60
III.3.4.1. Principle of FTIR	60
III.3.5. M-line spectroscopy (MLS)	60
III.3.6. scanning electron microscopy SEM	62
III.3.7. Energy Dispersive X-ray Spectrometry (EDX or EDS)	64
III.3.8. Atomic force microscopy (AFM)	65
<u>Chapitre IV : Results and discussions</u>	
IV.1 Zn-doped TiO₂ thin films	67
IV.1.1. X-ray Diffraction Analysis	67
IV.1.2. Morphology analysis	70
IV.1.3. Optical analysis	71
IV.1.4. M-lines analysis	75
IV.2 Synthesis metallic oxides and pair of oxides based on TiO₂ thin films	81
IV.2.1. Raman Analysis	81
IV.2.2. FTIR analysis	85

IV.2.3. AFM analysis	87
IV.2.3. Optical analysis	89
Conclusion	92
References	94

List of table

Tableau.I.1	The difference between the material's bulk state and its thin state	4
Tableau.I.2	Structural properties of TiO ₂ .	19
Tableau I.3	The main crystal faces of TiO ₂ .	21
Tableau.I.4	Basic properties of zinc oxide.	31
Tableau. I.5	Various types of Copper oxides and their physical applications.	32
Tableau. I.6	Various types of iron oxide and their physical properties.	33
Tableau. III.1	Comparison of glass substrate and silicon substrate.	46
Tableau. III.2	List of chemicals employed in the study.	48
Tableau. IV.1	Microstructural properties of Zn: TiO ₂ thin films.	69
Tableau. IV.2	Thickness, band gap, shift in band gap and grain size calculated from transmittance spectra.	74
Table.IV.3	Valuable for N _{eff} Zn: TiO ₂ thin films.	76
Table.IV.4	Comparison of the calculated values of refractive index from various models.	79
Table.IV.5	Modes vibration of TiO ₂ , ZnO, and CuO.	81
Table.IV.6	Positions and FWHM of Raman peaks for as prepared for monolayers and bilayers based on TiO ₂ thin films.	84
Table.IV.7	Modes of TiO ₂ , ZnO, and CuO.	86
Table.IV.8	Roughness parameters.	88
Table.IV.9	Band gap and refractive index for monolayers and bilayers based on TiO ₂ thin films.	90

List of figures

Figure.I.1	Classification of films courtesy.	3
Figure.I.2	Schematic of thin film deposited on a substrate	3
Figure.I.3	Interfacial surface energies involved in nucleation and film growth	5
Figure.I.4	The growth modes: a) Frank-van der Merwe, b) Stranski–Krastanov, c) Volmer-Weber.	7
Figure.I.5	Broad classification of thin-film deposition processes.	9
Figure.I.6	Synthesis steps involved in the sol-gel chemical method.	12
Figure.I.7	Schematic of spin coating technique for the deposition thin films.	15
Figure.I.8	TiO ₂ structures (a) anatase, (b) rutile and (c) brookite.	18
Figure.I.9	TiO ₂ nanostructures: 0D, 1D, 2D, and 3D.	22
Figure.I.10	Schematic of an ideal TiO ₂ lattice a) that is free of point defects (stoichiometric) and b) . A lattice involving point defects in both cation and oxygen sublattices (defect disorder).	24
Figure.I.11	A comparison of the number of publications on pure, doped, and composite TiO ₂ thin films from 2000 to 2023. Inset: illustration of the last five years.	25
Figure.I.12	Application of TiO ₂ .	26

Figure.I.13	Illustration of TiO ₂ /ZnO bilayer thin film onto substrate.	32
Figure.II.1	Principal elements of an optical fiber.	35
Figure.II.2	Diagram of nonlinear effects in optical fibers.	42
Figure.II.3	Single pump and dual pump.	43
Figure.III.1	Experimental spin coating device for thin films.	48
Figure.III.2	A photograph of the furnace for the thermal treatment.	50
Figure.III.3	XRD instrument schematic.	52
Figure.III.4	X-ray diffraction pattern by a family of lattice planes.	52
Figure.III.5	Mechanism of Raman scattering.	54
Figure.III.6	V-730 UV-Visible Spectrophotometer.	56
Figure.III.7	Transmission spectrum for thin films.	57
Figure.III.8	Comparison of indirect and direct band gaps.	59
Figure.III.9	The schematic depiction of FTIR.	60
Figure.III.10	Scheme of prism coupling in the MLS and MWMLS apparatus.	62
Figure.III.11	Schematic diagram of SEM.	63

Figure.III.12	General Mechanism of emitting X-ray.	65
Figure.III.13	Schematic of an atomic force microscope.	66
Figure.IV.1	XRD pattern of a) undoped TiO ₂ thin films, b) 3wt. % Zn: TiO ₂ thin film, c) 7wt. % Zn: TiO ₂ thin film.	68
Figure.IV.2	SEM images of the: a) undoped TiO ₂ and b) 7 wt% Zn: TiO ₂ films.	70
Figure.IV.3	Transmittance spectra of the Zn: TiO ₂ films of (a) 0 wt% Zn: TiO ₂ , (b) 3 wt% Zn: TiO ₂ , and (c) 7 wt% Zn: TiO ₂ .	71
Figure.IV.4	Indirect band gap energy (Tauc's plot) estimations of Zn-TiO ₂ .	72
Figure.IV.5	Thickness and band gap.	73
Figure.IV.6	TE and TM mode spectra of Zn: TiO ₂ films (a) 0, (b) 3, (c) 7 wt% Zn; (d) effective indices vs. Zn concentration.	76
Figure.IV.7	n _{TE} and n _{TM} refractive indexes and birefringence of Zn: TiO ₂ thin films.	78
Figure.IV.8	Results of the Raman spectroscopy analyses for the synthesized thin films.	83
Figure.IV.9	FTIR measurement patterns of TiO ₂ , ZnO, CuO, ZnO/TiO ₂ , and CuO/TiO ₂ thin films.	85
Figure.IV.10	The AFM results surface images of 2D on TiO ₂ , ZnO, CuO thin films, and ZnO /TiO ₂ , CuO/TiO ₂ bilayer thin films.	87
Figure.IV.11	The transmittance spectra of TiO ₂ , ZnO, CuO thin films, and ZnO/TiO ₂ , CuO/TiO ₂ bilayer thin film in the wavelength.	89
Figure.IV.12	The band gap energy for monolayers and bilayers based on TiO ₂ thin films is estimated from the tauc plot.	91

Introduction

Titanium dioxide (TiO₂) thin films possess remarkable technological potential due to their specific characteristics, such as excellent chemical stability, high refractive index, high dielectric constant, wide band gap, and transparency to visible light. These attributes make TiO₂ films suitable for various applications in optical and optoelectronic components, detectors, photocatalysts, waveguides, solar cells, sensors, and energy storage. TiO₂ exists in three main crystalline forms, known as polymorphs, each with unique structural and chemical properties. These polymorphs are: anatase (tetragonal), rutile (tetragonal), and brookite (orthorhombic) [1-4].

Anatase is indeed well-known for its strong photocatalytic activity. However, its photocatalytic activity is primarily limited to the utilization of ultraviolet (UV) radiation, which constitutes only a small portion of the solar radiation spectrum. The limited response of anatase TiO₂ to visible light has proven to be a significant challenge in harnessing solar energy for photocatalytic applications. However, researchers have made considerable efforts to extend the photocatalytic activity of TiO₂ to the visible light range. This has led to the development of various strategies and modifications aimed at enhancing the visible light absorption and overall efficiency of TiO₂ based photocatalysts. Additionally, TiO₂ presents a promising alternative to carbon-based anodes in lithium-ion batteries. TiO₂ NPs offer numerous advantages, including notable photocatalytic activity, hydrophilicity, UV-blocking properties, enhancement of specific physicochemical characteristics, reinforcement of nanocomposites, and antibacterial capabilities [5-7].

The synthesis of TiO₂ thin films can be achieved through various techniques, including physical vapor deposition (PVD) and chemical vapor deposition (CVD), sol-gel methods, and atomic layer deposition (ALD). Each synthesis method offers advantages in terms of film quality, thickness control, and scalability, allowing for the production of high-quality TiO₂ thin films in different forms and structures.

Metallic oxides are compounds composed of a metal element bonded to oxygen. These oxides exhibit a range of properties and are widely used in various fields due to their unique characteristics. When TiO₂ and ZnO are combined in a bilayer structure, they can exhibit synergistic effects and complementary properties. The TiO₂ layer can act as a UV absorber and generate electron-hole pairs, while the ZnO layer can provide improved electrical

conductivity and efficient charge transport. This combination enhances the overall performance of the thin film for various applications. In solar cells, the ZnO/TiO₂ bilayer structure can be used as an electron transport layer or as a part of the photoactive layer. The sample's optical characteristics were characterised using UV-Vis. The capacity to absorb and transmit light is a key feature in evaluating the optical performance of conductive oxide films. When TiO₂ and CuO are combined also in a bilayer thin film structure, it can lead to interesting properties and potential applications [8,9].

This study involves the synthesis of Zn doped nanocrystallite TiO₂ films and the synthesis of metallic oxides and pair of oxides based on TiO₂ thin films: ZnO/TiO₂ and CuO/TiO₂ bilayer thin films, through a sol-gel process. Initial materials included solutions containing titanium isopropoxide, zinc acetate dehydrate, and copper (II) diacetate hydrate. The films were produced using spin-coating. The study examines the films' structural, microstructural, topological, and optical characteristics, with a focus on investigating waveguides in the Zn doped TiO₂ film.

The thesis is structured as follows:

- ✓ **In chapter I**, we provide a general description of thin films and their growth and deposition mechanisms, with a particular focus on the sol-gel method, which offers several advantages, including good control over film composition and the ability to produce films with various morphologies. We focus on TiO₂ and explore its main properties, including its crystalline structure, electronic band structure, optical characteristics, and electrical properties. In the concluding section of this chapter, we present an overview of the synthesis of metal oxide and its application,
- ✓ **In chapter II**, we will explore the nonlinear properties, since we studied nonlinear properties (M-Lines),
- ✓ **Chapter III** presents the procedures used to grow the Zn-doped TiO₂ films and metallic oxides and pair of oxides based on TiO₂ thin films and the main devices employed to determine the structural, microstructural, topological, and optical characteristics of the obtained thin film,
- ✓ **In chapter IV**, we present the experimental results relating to the samples prepared for the study.

Chapitre I: Etude bibliographique.

I. 1. Thin film

Thin film is a layer that extends infinitely along any two directions but is restricted along the third direction. Most thin films have thicknesses ranging from monolayer to nanometer levels up to several micrometers (**figure I.1**) i.e. layer quasi two-dimensionality. Thin films can consist of different materials, such as metals, semiconductors, insulators, and polymers. They are often deposited on substrates or surfaces to modify their properties or add specific functionalities.

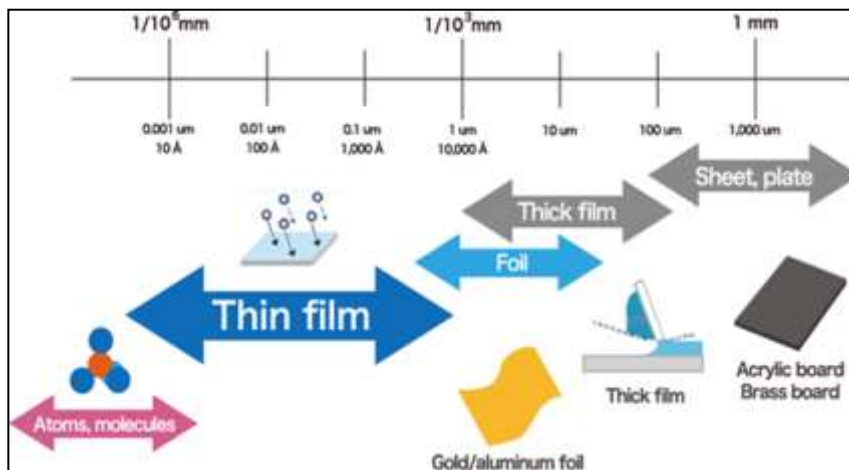


Figure I.1. Classification of films courtesy https://www.susumu.co.jp/usa/tech/know_how_02.php.

The small distance show in **figure I.2** between the two boundary surfaces gives a disturbance of the chemical, physical and mechanical properties [10].

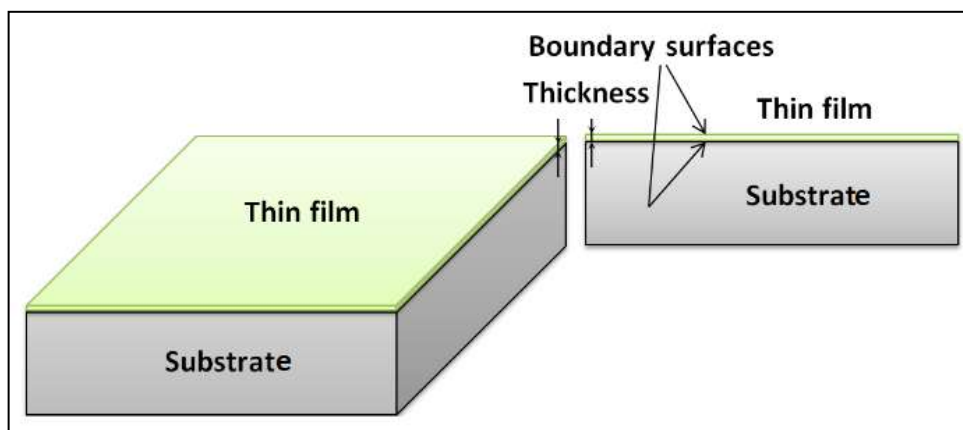


Figure I.2: Schematic of thin film deposited on a substrate.

Table I.1: The difference between the material's bulk state and its thin state [10, 11].

Materials	Bulk	Thin Film
Role of the boundaries in the properties	Neglected	not neglected
Ionic Conductivity	Generally lower due to more uniform and isotropic volume.	Potentially higher due to reduced path for ion migration and enhanced surface effects.
Interfacial Stability	Less of a concern due to homogeneous material properties.	More challenging due to increased surface-to-volume ratio, leading to potential instability at interfaces.
Growth Control	Easier to control due to well-established techniques for bulk synthesis.	More difficult, requires precise control over deposition processes to achieve uniform thin films.
Thermal Conductivity	Measured using techniques like steady-state methods, assuming uniform properties throughout.	Requires specialized techniques like the 3ω method or transient thermorefectance, due to significant surface and interface effects.
Application	Used in applications where large volume and isotropic properties are beneficial, like bulk storage batteries.	Suitable for applications requiring miniaturization and enhanced surface properties, like solid-state thin-film batteries and microelectronics

I. 2. Thin film formation

The capillarity idea explains the first steps in the formation of thin films from vapors phase. This technique is qualitative in nature, and while quantitatively inaccurate, it makes valuable predictions. The nucleation process occurs during the initial phases of film formation. Atoms and molecules collide with the substrate and get physisorbed as a result of a permanent or fluctuating dipole moment, which causes *Van der Waals* attraction. Physisorbed species then chemisorb and contribute to nucleus formation (see **figure I.3**).

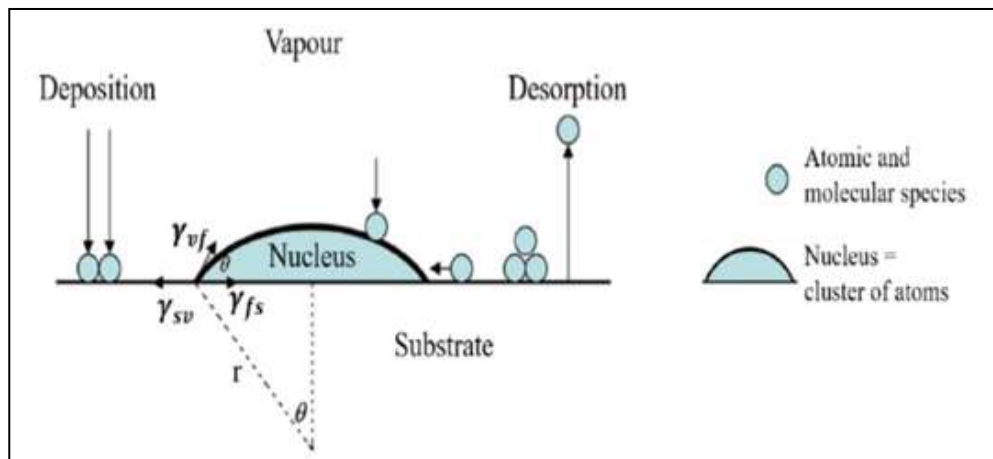


Figure I.3. Interfacial surface energies involved in nucleation and film growth [12].

The thin film growth demonstrates the following features [13, 14]:

1. The formation of thin films from various materials begins with a random nucleation process. This is followed by stages of nucleation and growth, including island growth, coarsening and coalescence, and percolation,
2. The nucleation and growth stages are influenced by a variety of deposition parameters, including growth rate, growth temperature, and the substrate's surface chemistry.
3. The nucleation stage can be altered through external interventions, such as bombardment by electrons or ions.
4. The film microstructure, accompanying defect structure, and film stress are determined by the nuclear stage deposition conditions.
5. The crystal phase and orientation of thin films are determined by the deposition circumstances. The structure influences the thin film's properties, whereas the reaction conditions and deposition procedure affect the film's mechanical and thermal properties.

I. 3. Thin films growth modes

Nucleation and subsequent film growth is understood by considering the relative interfacial surface energies between the substrate and film. The nucleation process depends on the tension between the substrate-vapour denoted as γ_{sv} , substrate-film γ_{sf} , and vapour-film γ_{vf} interfaces. That is linked to Young's equation [12, 15, 16, 17, 18]:

$$\gamma_{sv} = \gamma_{sf} + \gamma_{vf} \cos \theta \dots\dots\dots (I.1)$$

The " θ " denotes the angle of contact between the substrate and the nucleus.

Thin films growth is classified into three categories [16]:

I. 3.1. Volmer-Weber or island (VW)

$$\gamma_{sv} < \gamma_{sf} + \gamma_{vf} \dots\dots\dots (I.2)$$

The growth mode is 3D. This type of growth occurs when the interaction between the atoms or molecules of the deposit is greater than the interaction between the atoms or molecules and the substrate in **(figure I.4.a)**. The nucleation of the condensed phase first occurs in the form of small, distinct clusters on the substrate surface. This nucleation can occur at random locations on the substrate, and with the arrival of other atoms, the clusters grow into islands. These islands can be of various sizes and shapes, and voids (regions devoid of material) separate them from one another. As the islands continue to grow, they may eventually touch and merge with neighboring islands. This coalescence process leads to the formation of a continuous film. This mode is observed in numerous metal systems that grow on insulators. This growth mode can have both advantages and disadvantages. On the positive side, it can be used to create quantum dots, nanoclusters, or other nanostructures with unique properties. On the negative side, island growth can result in surface roughness and discontinuities in the final film, which may be undesirable in some applications. To mitigate these issues, researchers and engineers often use techniques such as annealing or strain engineering to control island growth and achieve smoother, more continuous films when needed.

I. 3.2. Frank-van der Merwe (FM) or layer by layer

$$\gamma_{sv} \geq \gamma_{sf} + \gamma_{vf} \dots\dots\dots (I.3)$$

The growth mode is 2D, when the atoms are more tightly bonded to the substrate than to each other in **(figure I.4.b)**. The first atoms that come together create a single layer on the surface, which then gets overlaid by a second layer that is slightly less tightly bound, with each new layer conforming to the lattice structure of the layer below it, and from there, the growth process occurs layer by layer. This type of growth is commonly observed in homogen growth, such as in metal on metal or semiconductor on semiconductor systems.

I. 3.3. Stranski-Krastanov (SK)

Often known as The Layer + island, is a growth mode of mixed type in (figure I.4.c). This growth mode is a combination of the two previous growth modes and represents an interesting intermediate case. When forming the first monolayer, the growth is 2D, but it becomes 3D beyond one or more monolayers. There are now numerous instances of its presence in various systems, such as metal/metal, metal/ semiconductor, such as indium films deposited on <100> single crystal Si substrates, gas/metal, and gas/layer compound systems.

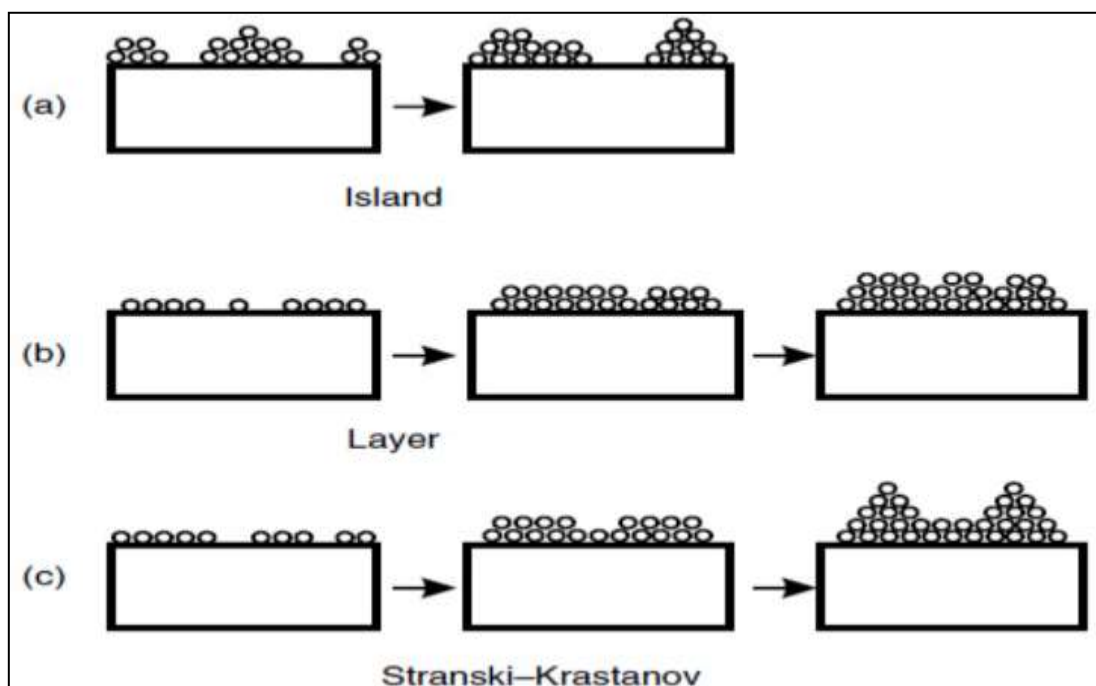


Figure I.4. The growth modes: a) Frank-van der Merwe, b) Stranski–Krastanov, c) Volmer-Weber.

I. 4. Thin film deposition techniques

I. 4.1. Historical descriptions and recent compilations

Thin films have been produced since the advent of vacuum systems. However, the use of deposition to produce films for device purposes is a more recent advancement, occurring within the last 40 years. Initially, thin metallic film coatings on glass or plastic were utilized for optical applications such as mirrors and sunglasses, this remains a significant business conducted under high vacuum conditions. These films typically exhibit polycrystalline island

growth. Over the past 25 years, thin film deposition processes have rapidly advanced, especially in relation to semiconductor devices. These processes have evolved into highly specialized and are extensively documented in textbooks like *Smith (1995)* and compilations like the Handbook of Thin Film Process Technology (*Glocker & Shah 1995*), which feature multiple authors and regularly updated sections. The following sections provide an overview of some of these developments [19]. Various physical and chemical techniques can be employed to create thin films. The transfer of thin film material, which is deposited through physical processes, from a source target to the substrate is facilitated by utilizing a form of energy. This technique is frequently used for single component films like metal films. Vacuum evaporation and sputtering are examples of physical processes where the thin film is deposited after converting the substance into a gas through evaporation or impact action. On the other hand, chemical reactions are utilized in chemical methods [20].

Thin film deposition techniques (**Figure I.5**) are methods used to deposit thin films of material onto different substrates such as glass, metallic, ceramic, etc.

- ✓ **Chemical Vapor deposition CVD:** A fluid precursor experiences a chemical transformation at a solid surface, resulting in the formation of a solid layer.
- ✓ **Physical Vapor deposition PVD:** Uses mechanical, electromechanical, or thermodynamic methods to create a thin solid film.

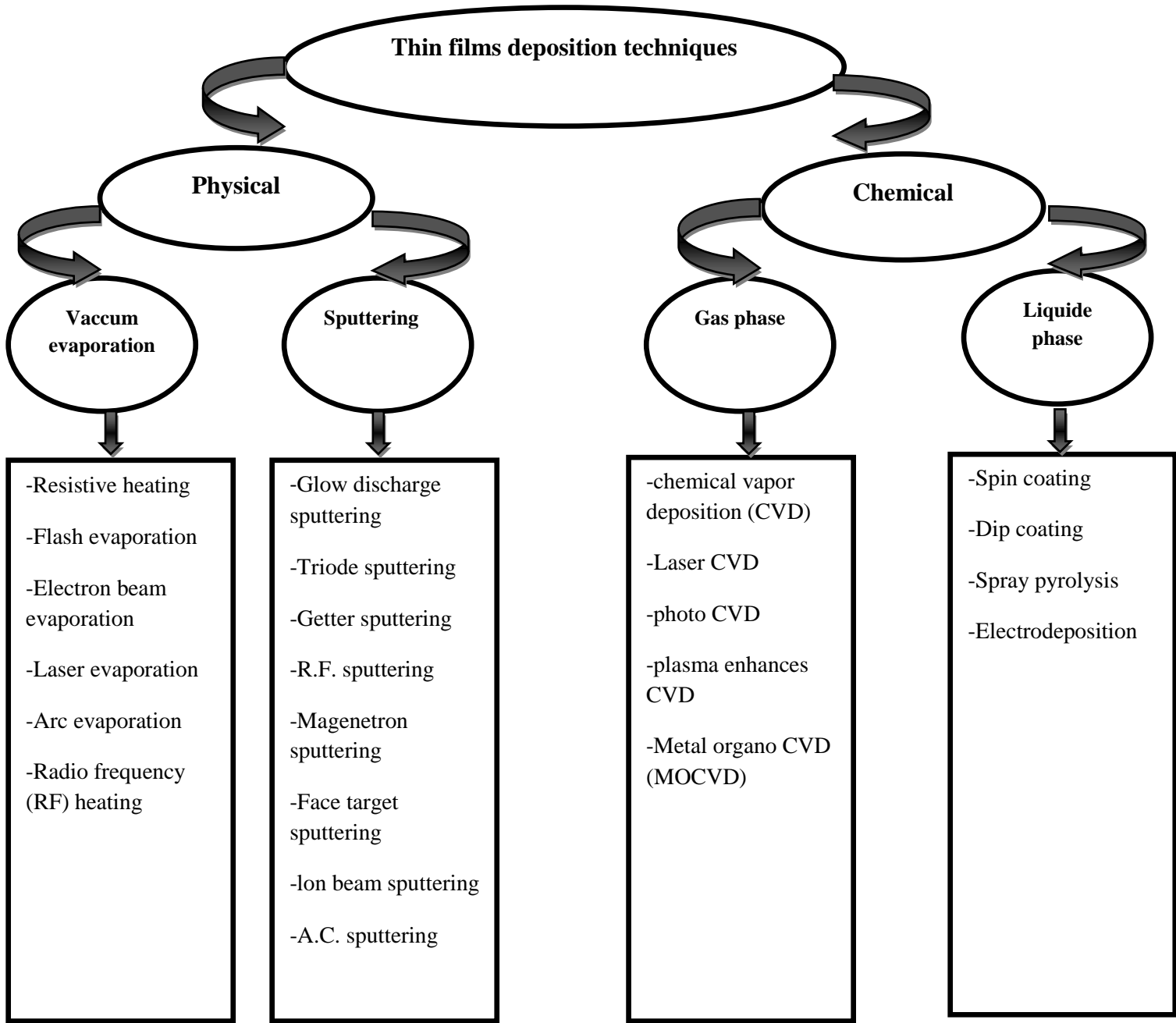


Figure I.5: broad classification of thin-film deposition processes.

I. 4.2. Different PVD and CVD [21]:

- Chemical methods are less expensive and simpler than physical methods,
- PVD coatings are produced more quickly than CVD coatings because of a higher deposition rate: this is because in PVD, the

material is physically ejected from a target and directly deposited onto the substrate, leading to a faster coating deposition. CVD processes involve chemical reactions at the substrate surface, which may proceed at a slower rate,

- CVD coatings are typically produced at much higher temperatures compared to PVD coatings: The elevated temperatures in CVD are necessary to activate the chemical reactions between the precursor gases and the substrate surface. This is in contrast to PVD, where the material is transferred in the vapor phase through physical processes like evaporation or sputtering, often at lower temperatures.

I. 5. sol-gel

I. 5.1. History and development of the sol-gel process

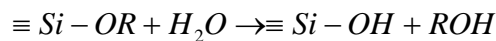
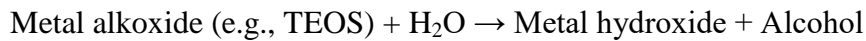
The contraction for solution-gelification would be "sol-gel". The synthesis method is called "soft chemistry" because it is generally carried out from hydroalcoholic solutions at ambient temperature and pressure, unlike methods based on the melting of raw materials, which require extreme synthesis conditions. In the mid-19th century, J.J. Ebelmen demonstrated that a silicon ester solidifies into a transparent mass when exposed to a wet atmosphere. This process, known as the acidic hydrolysis of silicon alcohols, results in the formation of SiO₂ silicon oxides with excellent optical transparency. In 1939, the Schott Glaswerke Company patented the deposition of thin films on glass through immersion, leading to the development of thin layers that are easier to shape and dry faster than massive gels. This innovation prevented the problem of frost cracking during drying. For example, the German company Scott & Genossen developed silica coatings by extending colloidal solutions of silica acid on a glass plate. The ceramic-gel process made it possible to produce ceramic materials based on aluminum, silica, titanium, and zirconium oxide in the 1950s and 1960s that were previously impossible to grow using conventional techniques. Thus, through the sol-gel process, it is possible to obtain dense, thin layers, fibers, or monoliths [22].

I. 5.2. Hydrolysis and condensation reactions

The main chemical reactions in the sol-gel process are hydrolysis and condensation. These change precursor compounds in solution (sol) into a gel and then into a solid (**figure I.6**). These reactions are critical for controlling the composition, structure, and properties of the final product

I. 5.2.1. Hydrolysis reactions

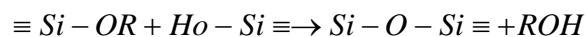
The hydrolysis reaction leads to the substitution of an alkoxy group (OR) by a hydroxyl group (OH). Where it is considered is the initial stage of the sol-gel process, where the precursor compounds are exposed to water (H₂O) to break chemical bonds between elements in the precursor molecules. Typically, the precursor compounds used in the sol-gel process are metal alkoxides, such as tetraethyl orthosilicate (TEOS) for silica-based materials or metal chlorides, nitrates, or acetates. In the hydrolysis reaction, the metal alkoxide reacts with water to produce metal hydroxides and alcohol molecules as byproducts



The "R" denotes a proton or other ligand (if R is an alkyl, then "OR" represents an alkoxy group), and ROH represents an alcohol, It is generally catalyzed by a base or an acid [22, 23]. The hydrolysis reaction is usually performed under controlled conditions to control the extent of hydrolysis, which influences the properties of the resulting gel.

I. 5.2.2. Condensation reactions

The hydrolyzed or partially hydrolyzed molecules $\equiv\text{Si-OH}$ (silanols) then reacts with each other or with non-hydrolyzed alkoxydes to form siloxane bridges, Si-O-Si. The condensation occurs either by the elimination of a water molecule or by the elimination of an alcohol molecule.



The successive reactions (polycondensation) lead to the polymerization of silanols. Thus, an interconnected network of silicate polymer chains gradually forms in the mother solution. To obtain a polymeric gel, one must place themselves under experimental conditions that shift these reactions towards condensation, meaning that in the case of slow hydrolysis or alcoholysis compared to condensation, the relative kinetics of hydrolysis and condensation

reactions are directly linked to the final structure of the material: pore size, optical quality, rigidity, etc. The main parameters influencing the relative speeds of these two reactions are pH, water proportion, solvent proportion, and precursor nature. What interests us here specifically is the size of the pores in the obtained sol-gel matrix [22].

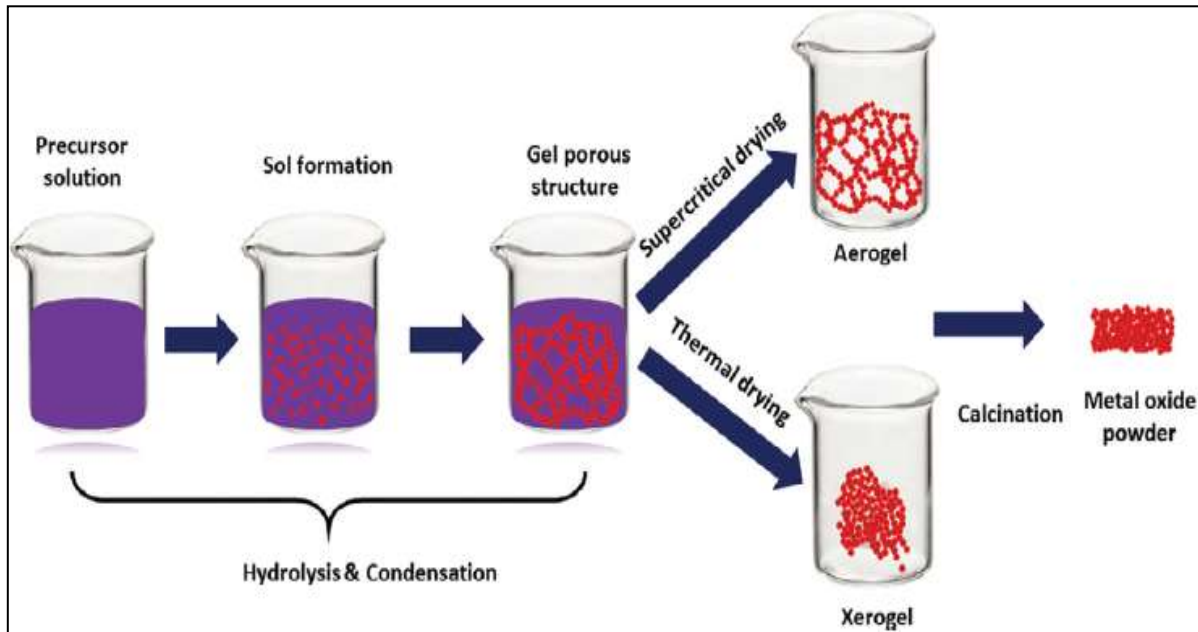


Figure I.6: Synthesis steps involved in the sol-gel chemical method [20].

Various chemical and physical methods are being used to create metal oxide materials with varying sizes, such as nano, micro, macro, and mesoporous, to enhance their nonlinear, electrical, optical, and magnetic properties. Factors such as PH, temperature, solvent, time, and catalyst play a crucial role in sol-gel chemistry. PH is particularly significant in colloidal chemical reactions involving water as a solvent. During the polymerization process that forms nanoparticles, the solvent serves two key functions: preventing the nanoparticles from precipitating out of the liquid and aiding in their connection with each other. Temperature affects the chemical kinetics involved in creating nanoparticles within a gel complex and influences gel formation time. Gelation is a slow process that can span several days at reduced temperatures ($\leq 100^{\circ}\text{C}$) but occurs much more quickly at elevated temperatures ($\geq 100^{\circ}\text{C}$). Adjusting the gelation temperature is important for optimizing reaction time. The speed of the chemical process in sol-gel reactions can be accelerated by the presence of a catalyst that is sensitive to PH. Several research groups have successfully synthesized metal oxides using sol-gel reactions [20, 23].

I. 5.3. The Sol-Gel Process

The sol-gel process, also known as soft chemistry or chimie douce [24]. The Sol-Gel Process The word 'sol' refers to the creation of a colloidal suspension, while 'gel' refers to the transform of 'sol' into solid substances or viscous gels. The sol-gel method is a highly popular chemical technique for fabricating thin films, and it is also an environmentally friendly technique. This technique includes the creation of a sol and gel by hydrolysis and condensation reactions. The instances of alkoxides employed in the sol-gel process include a range of elements such as transition metals like iron, nickel, and cobalt; pre-transition metals like titanium and aluminum; and post-transition metals like silicon. In general, the sol-gel process may understood through the following steps:

1. **Mixing:** the process begins with the mixing of precursors, often metal alkoxides, in a solvent. The choice of precursors and solvent depends on the desired properties of the final material,
2. **Deposition:** involves applying the sol onto a substrate. This can be done using various methods, like as spin coating, dip coating, or spraying. The goal is to achieve a uniform and controlled coating on the substrate, Deposition occurs at atmospheric pressure over a large area, making it a cost-effective and rapid method.
3. **Gelation:** is the transformation of the sol into a gel. This step is often initiated by adding a gelation agent or by controlling the solute concentration in the solution. The gelation process can be controlled to produce materials with specific structures and porosities,
4. **Drying:** is to remove the solvent from the gel. This can be achieved through various drying methods, such as evaporation or supercritical fluid extraction. The drying process helps to stabilize the gel structure and prevent its collapse,
5. **Heat Treatment (Calcination):** The dried gel is subsequently exposed to heat treatment. During calcination, the material undergoes a series of chemical and physical transformations, such as elimination of organic constituents and the crystallization of the inorganic components phase. This step is crucial for obtaining structure achieving the desired.

I. 5.4. The advantages of the sol-gel method [20, 25, 26, 27, 28]:

- ❖ environmentally friendly,

- ❖ Simple and easy,
- ❖ The temperature generally remains low, close to room temperature. As a result, thermal volatilization is minimized,
- ❖ Inexpensive and consumption of energy,
- ❖ Shape and size control,
- ❖ produce highly pure and homogeneous oxides and permits
- ❖ The easy incorporation of dopants,
- ❖ Controllability,
- ❖ Reliability,
- ❖ Reproducibility,
- ❖ Speedy deposition on large area with good homogeneity.

I. 5.5. The disadvantages of the sol-gel methods [20, 28]:

- ❖ applicable to a limited range of metal oxides,
- ❖ Complicated,
- ❖ high permeability,
- ❖ Gives better homogeneity for multicomponent materials.

I. 6. Different sol-gel method

I. 6.1. Spin-Coating

Spin coating is a commonly used method for depositing thin films onto substrates (**figure I.7**). It offers the primary advantage of easily producing uniform films. The process involves spinning a solution of a particular material at elevated speeds, which creates centripetal force and surface tension that evenly covers the substrate. As the excessive solvent evaporates, a thin film with thickness ranging from a few nanometers to a few microns is produced. This method can be employed to coat substrates of different sizes, to coat small substrates ranging from a few millimeters to over a meter in diameter. The key advantages of spin coating are its simplicity and ease of setup, as well as the resulting thinness and uniformity of the films produced [29].

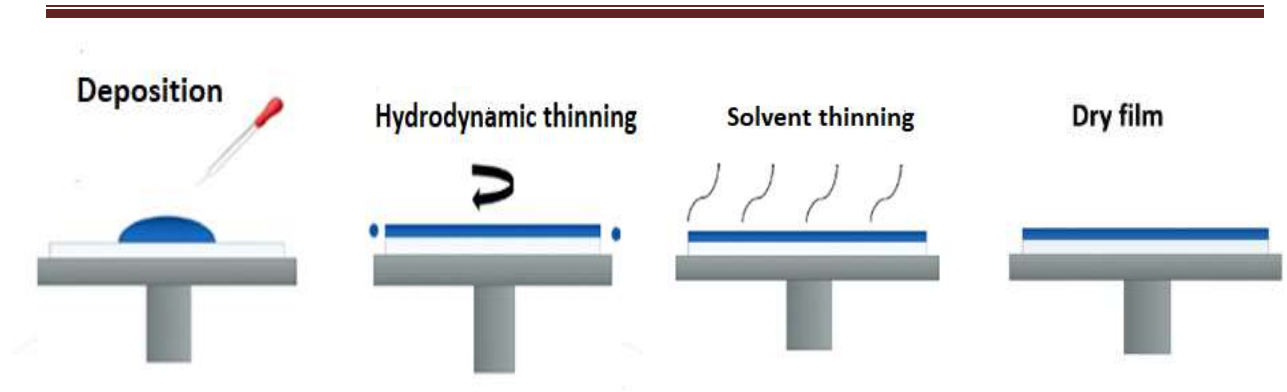


Figure I.7: Schematic of spin coating technique for the deposition thin films [30].

The spin coating process generally consists of four key stages [20, 29]:

- a) **Deposition:** The initial step is done by dispensing the solution onto the substrate surface, a droplet of material is kept at the center of the substrate. To spread the fluid takes place due to centrifugal force, when the substrate has already started spinning (dynamic spin deposition) or has been set on spin after deposition (static spin deposition).
- b) **Spin up:** In this process, once the solution has been transferred to the substrate surface, the substrate is accelerated up to its desired speed. The rotation disc is speeded up to achieve the desired rotation speed. This can be done either immediately or through a gradual speed-up steps. At first, the solution rotates at a different speed than the substrate. However, over time, when the drag force equalizes the rotational accelerations, the two rotational speeds will coincide, resulting in the creation of a thin fluid layer.
- c) **Spin off:** During the spin-off third stage, which is characterized by the thinning of the fluid and a constant spin speed, viscous forces dominate the solution's transformation into a thin film. The film's thinning behavior is overcome by the fluid's viscous force. As a result, the film thins out so that shear drag can counteract the centrifugal force, resulting in a uniform thickness. If the solution flows uniformly outward, it indicates edge effects. Mathematical treatments show that if the fluid has Newtonian viscosity and initially has a uniform thickness across the wafer, then the thickness profile will remain uniform at any subsequent time. This ultimately results in the creation of a consistent final coating.
- d) **Evaporation:** This stage is characterized by the dominant evaporation of the solvent and rate of depends on the solvent vapor pressure, ambient temperature, and volatility. These processes are repeated multiple times in order to achieve the desired thickness

of the film being studied. Where leading evaporation of the solvent the thinning of the coating. The viscosity of the solvent becomes less influential on fluid flow as the solvent thickness decreases. During this process, volatile species evaporate, causing an increase in viscosity and effectively freezing the coating. Typically, the freezing occurs on the film's surface, resulting in a skin layer with a higher viscosity than the primary fluid due to solvent removal. This leads to a decrease in fluid flow rate and film evaporation rate.

When using the spin coating technique to prepare the coating, certain technical parameters have the strongest influence on the final film thickness, these parameters include the following [20, 31]:

- **Spin speed:** The centrifugal force acting on the fluid depends upon the spin speed of the substrate and the velocity of the air directly above it. The final film thickness of the coating is entirely influenced by the spin speed, as the maximum speed leads to a decrease in film thickness. This reduction is caused by the increased evaporation rate, which in turn increases the viscosity of the solution.
- **Fluid viscosity:** The viscosity of the solution being spin-coating affects the film thickness. Higher viscosity solutions tend to result in thicker films, as the fluid has more resistance to spreading at higher spin speeds.
- **Solvent Evaporation Rate:** The rate at which the solvent evaporates during the spin-coating process can impact film thickness. Faster solvent evaporation tends to result in thinner films because the material is deposited before it has a chance to spread further.
- **Spin Time:** The duration of the spin-coating process, or spin time, is a crucial parameter. Longer spin times generally lead to thinner films as the coating solution has more time to spread out over the substrate.

The effect of spin acceleration [31]

- Acceleration
- Ambient

Spin coating involves two stages: one dominated by viscous flow and the other by evaporation. The estimation of the final coating thickness h_f , is determined based on various crucial solution parameters:

$$h_f = x \left(\frac{e}{2(1-x)K} \right)^{\frac{1}{3}} \dots\dots\dots (I.4)$$

Referring to the solution's evaporation and flow constants, as well as the effective solids content, denoted by e, K, and x respectively, the evaporation and flow constants are explicitly described as follows:

$$e = C\sqrt{\omega} \dots\dots\dots (I.5)$$

$$K = \frac{\rho\omega^2}{3\eta} \dots\dots\dots (I.6)$$

ω , ρ , η , and C represent the rotation rate, solution density, viscosity, and a constant of proportionality, respectively, the value of C is contingent upon the airflow flow regime (whether laminar or turbulent) and the diffusivity of solvent molecules in the air. It is noteworthy that the spin coating deposition method for preparing sol-gel films typically yields a coating thickness that is less than 1 μm [32].

I. 6.2. Dip coating

Also known as immersion coating, this is a simple, traditional, and straightforward method of depositing onto substrates that have both large areas and complex shapes, especially small slabs and cylinders. The process entails submerging the substrate in a solution and then removing it. As the substrate is withdrawn from the coating fluid, a coherent liquid film adheres to it. Afterwards, the film is dried and subjected to chemical reactions in order to consolidate it.

The formation of the film results from a fluid mechanical balance between the receding liquid and the entrained film. Various forces come into play to maintain this balance, including viscous drag, gravity, and surface tension. The thickness of the deposited film is determined by the equilibrium between viscous drag and gravity, allowing for precise film thicknesses of up to 1 μm to be achieved [33, 34].

Other factors such as surface tension, inertial force, and disjoining pressure also have a significant impact. The film thickness is controlled by the competition of these forces in the deposition region, where the *Landau-Levich* equation provides the measurement of the thickness of the film.

$$h = 0.94 \frac{\eta U^{2/3}}{\gamma^{1/6} \rho g^{1/2}} \dots\dots\dots (I.7)$$

Where U: the withdrawal speed, η : the liquid viscosity, γ : the surface tension, ρ : the Liquid density and g: gravity. The dip-coating process was described by *Scriven* [33] in five stages: immersion, start-up, deposition, drainage, and evaporation.

I. 7.Titanium dioxide

Titanium dioxide (TiO₂), also known as Titania, is a white crystalline powder that is insoluble in water. It is a nontoxicity substance that can be utilized to make nanomaterials with a high concentration of hydroxyl groups. Is known for its outstanding chemical stability, resistance to heat, and low electron conductivity, which make it an ideal material for preventing corrosion, and catalytic efficiency. It has a very high refractive index, which makes it the material of choice for coating photovoltaic cells and optical instruments. TiO₂ has three different polymorphs in (**Figure I.8**) anatase, rutile and brookite [35]. Additionally, other phases such as TiO₂B, TiO₂H (hollandite), TiO₂R (ramsdellite), TiO₂II (α -PbO₂), akaogiite (baddeleyite, 7 coordinated Ti), TiO₂O, cubic form, and TiO₂II (cotunnite PbCl₂) can be synthesized. The synthesis of anatase, rutile, and brookite TiO₂ nanoparticles involves hydrolysis, condensation, and calcination processes [36].

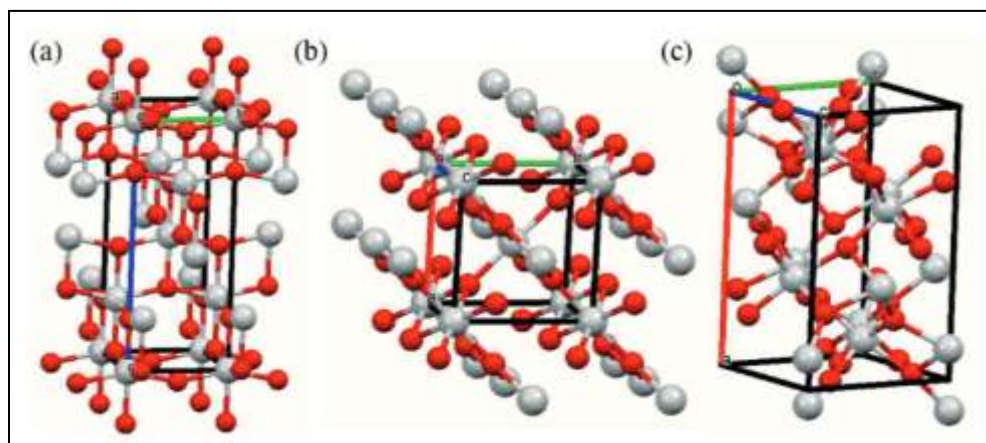


Figure I.8. TiO₂ structures (a) anatase, (b) rutile and (c) brookite.

I. 8. Properties of TiO₂

I. 8.1. Structural properties

These polymorphs can have different properties (**table I.2**). The basic structural features of rutile and anatase materials have been evaluated, as the less commonly used brookite structure is not frequently studied in exploratory investigations.

Table I.2.Structural properties of TiO₂ [16, 37].

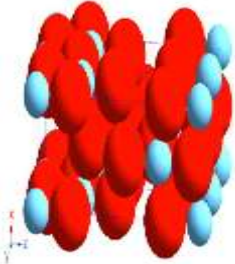
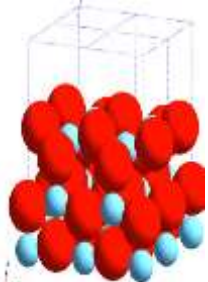
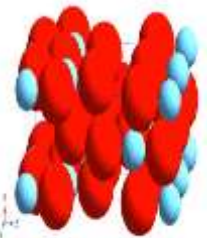
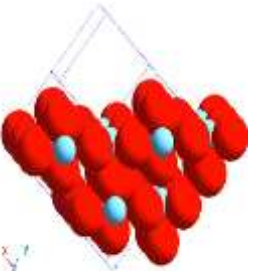
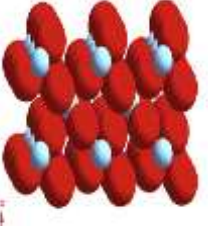
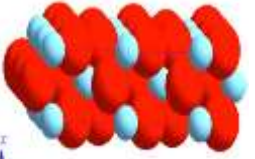



Property	Anatase	Rutile	Brookite
Crystal structure	Tetragonal	Tetragonal	Orthorhombic
Point group	4/mmm	4/mmm	mmm
Space group	^I 4 ₁ /amd	^P 4 ₂ /mnm	Pbca
(Z) (formula units per unit cell)	4	2	8
Lattice parameters (nm)	a = 0.3785 c = 0.9514	a = 0.4594 c = 0.29589	a = 5,4558 b = 9,1819 c = 5,1429
Refractive index (589 nm)	2,49 – 2,55	2.61-2.9	2,58 – 2,70
E_g (eV)	3.2	3.06	3.5
Density (g cm⁻³)	3.895	4.274	4.123 , 4.08-4.2
T_m: melting temperature (°C)	1843	1843	1830-1850
Hardness (Mohs Scale)	5,5 – 6,0	7,0 – 7,5	5,5 – 6,0

- **Anatase TiO₂** on the surface can be described as a crucial parameter because different surfaces can exhibit various properties. Anatase has two surfaces (001) and (101) with thermally stable and low energy of 0.90 Jm⁻² and 0.44 Jm⁻², respectively, typical nanocrystals rarely have the (100) surface [38, 39]. As table (03) shows, the (101) surface is the most common face for anatase nanocrystals and has a corrugated structure with alternating rows of five-coordinate titanium atoms and edge-bridging

oxygen in the corrugations [40, 41], the anatase form of TiO₂ is highly favored in photovoltaics, solar cells, and gas sensing applications due to its better electron mobility and chemical stability when compared to the rutile and brookite phases [42]. According to *Gopal et al.*, it was found (that the anatase phase of TiO₂ is more stable than the rutile phase under normal room temperature conditions (27 °C) and atmospheric pressure (760 mmHg) [43].

- **Rutile** the phase that is the most stable in thermodynamics and has three main crystal faces: (110), (100), and (001). The (110) and (100) faces are quite low in energy, making them important for powder materials or polycrystalline [44]. The (110) surface, in particular, is extensively researched because of its high surface energy and the valuable insights it provides into the structural characteristics of rutile. It is considered to be the most thermally stable face [38]. It consists of rows of bridging oxygens connected to two titanium atoms, which are 6-coordinate. On the other hand, there are rows of 5-coordinate titanium atoms running parallel to the rows of bridging oxygens. TiO₂, rutile, and anatase structures are commonly utilized for photocatalysis activity.
- **The brookite phase**, which is less common and more challenging to prepare, has also been investigated as a photocatalyst. The stability order of crystal faces is .010/ < .110/ < .100)

Table I.3: The main crystal faces of TiO₂.

Crystal phase	Main crystal faces		
Anatase [38]	 (101)	 (100)	 (001)
Rutile [38]	 (110)	 (100)	 (001)
Brookite [45]	 (110)	 (100)	 (110)

Due to the growing need for nanostructured materials, considerable investigations have been carried out to create technologies capable of producing the requirements for specific applications that can be met by nanocrystalline TiO₂ structures. Researchers have shown that reducing the particle size enhances a number of properties of TiO₂, showing how nanocrystallites work better (**figure I.9**), which depicts the dimensional range of TiO₂

nanostructures. The structures of TiO₂ nanoparticles range from (0D) to hierarchical or complex (3D). This is a crucial factor in deciding among the various applications of TiO₂. By manipulating the synthesis parameters, particularly pH, temperature, and thermal annealing, diverse morphologies with enhanced properties can be attained. Therefore, a variety of nanostructures were prepared through synthesis techniques, including classical methods (for nanorods, nanosheets, nanoflakes, and nanoflowers) or ultrasonic-assisted hydrothermal approach (for quantum dots), electrospinning (for nanofibers), spin coating, dip coating, and hydrothermal routes (for nanowires), anodization (for nanotubes), and template-assisted approaches (for nanospheres). Utilizing the aforementioned structured hierarchies led to improvements in various parameters, such as an augmented active surface area, enhanced charge carrier separation resulting in a reduced recombination rate, etc [46, 47].

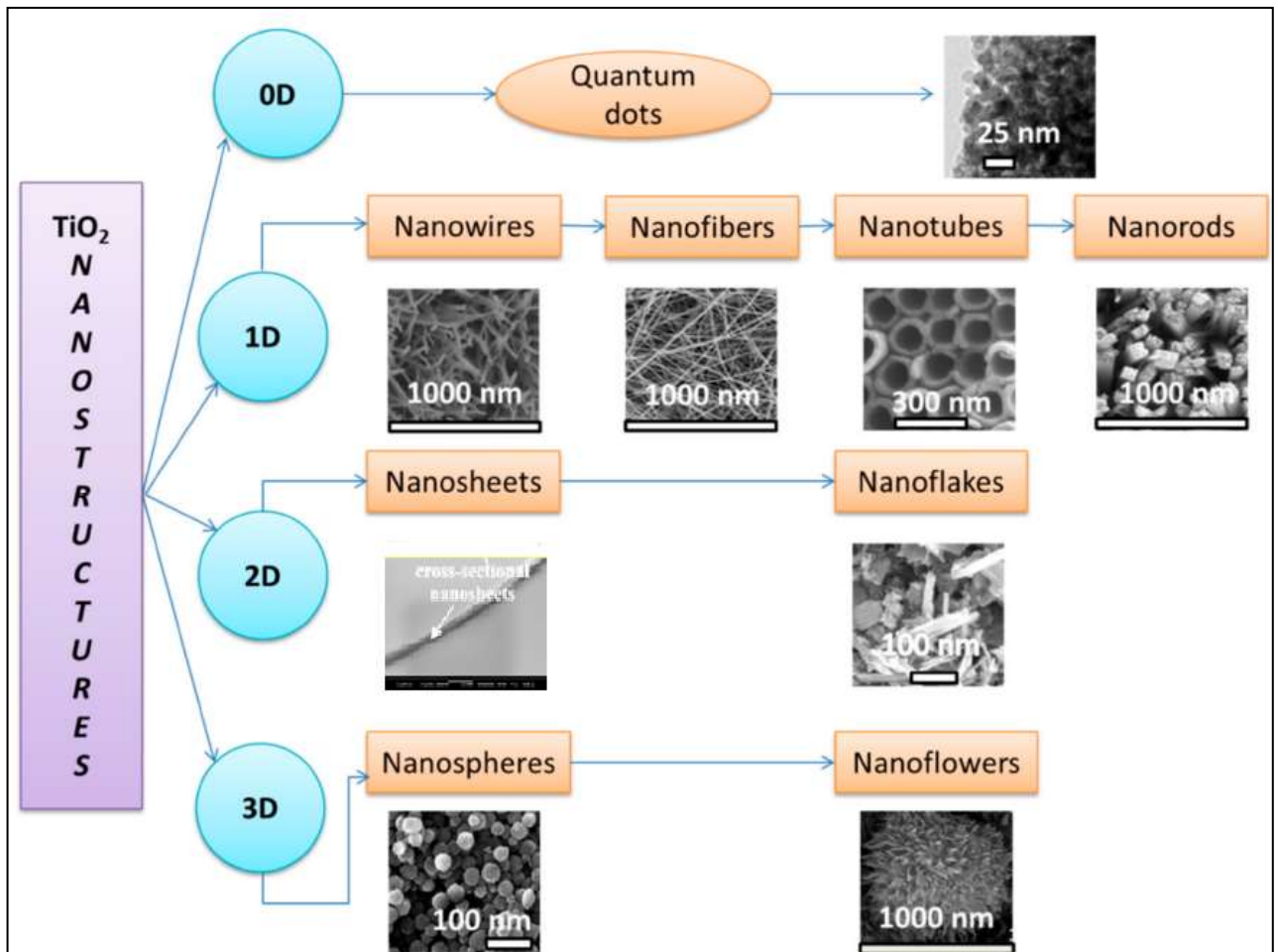


Figure I.9: TiO₂ nanostructures: 0D, 1D, 2D, and 3D.

I. 8.2. Morphological Properties

The predominant TiO₂ films utilized in practical applications have a structure that is nanocrystalline. Hence, gaining insights into how defects, both intrinsic and extrinsic, impact morphological properties becomes imperative for the purpose of engineering TiO₂ materials to make them versatile materials with applications in multiple fields, including photocatalysis, solar cells, sensors, energy storage, environmental remediation, and self-cleaning surfaces. Furthermore, the addition of dopants to TiO₂ films significantly shapes various processes, including the integration of dopants, the kinetics of crystal growth, and interactions at the surface surface Roughness, Film Thickness, porosity. Dopants have the capability to modify the nucleation and growth kinetics of TiO₂ nanocrystallites. The resulting sizes and shapes of the grown particles vary depending on factors such as the kind and amount of dopants, along with the deposition technology employed for doped TiO₂, where the dopants can promote the formation of specific crystal facets, resulting in altered particle shapes [46].

I. 8.3. Optical Properties

Optical properties of a solid are influenced by the propagation of light within it and the extent of light absorption by the material. The process is dependent on the material's dielectric permittivity, determined by the energy band gap structure and free electrons of TiO₂. All TiO₂ polymorphs exhibit elevated relative permittivity ($\epsilon_{ox} > 30$), along with a refractive index in the range of approximately 1.93 to 2.6 at a wavelength of 633 nm. They also display high transparency (about 80% transmittance) the visible spectrum range has a wide optical band gap ($E_g > 3$ eV). Metal oxides that have an energy exceeding 3 eV typically do not absorb in the visible light range. Therefore, TiO₂ emerges as a promising dielectric candidate, serving as a material possessing a high refractive index and transparency for use in multilayer optical systems. However, to fully harness Titania's potential in various applications, doping TiO₂ films with suitable atoms, whether metallic or non-metallic. These dopants influence optical characteristics by introducing energy levels within the band gap, facilitating the absorption of visible light and thereby altering the transparency of the oxide [46].

I. 8.4. Electrical Properties

Despite extensive research into the properties pertaining to both structure and optics, the understanding of TiO₂ electron transport is limited due to its considerable electrical resistance of around 10⁸ Ωcm . It functions as a band gap semiconductor, and the energy of its band gap varies depending on the crystalline phases of TiO₂. One thing that all TiO₂ films made by different technologies have in common is that they are no longer stoichiometric. Instead, it exhibits a complex defect structure with an elevated presence of intrinsic defects. These defects encompass oxygen vacancies V_O, titanium interstitials Ti_{int}, titanium vacancies V_{Ti}, and oxygen interstitials O_{int}. Most of the defects found are n-type, creating shallow donor states below the conduction band in the TiO₂ energy gap. These defects are oxygen vacancies V_O and titanium interstitials Ti_{int}. This elucidates the n-type semiconductor nature of pure TiO₂ and the nonstoichiometry. However, the authors' recent research indicates that oxidized TiO₂ might display p-type properties due to the simultaneous existence of acceptor-type defects in the form of titanium vacancies. In situations where titanium vacancies are the predominant defects, either the formulas TiO_{2+x} or Ti_{1-x}O₂ could be utilized, especially when dealing with p-type TiO₂ where Ti/O < 1/2. One may expect that the formation of TiO₂ that exhibits a deficit in the metallic sublattice may require prolonged oxidation [48, 49].

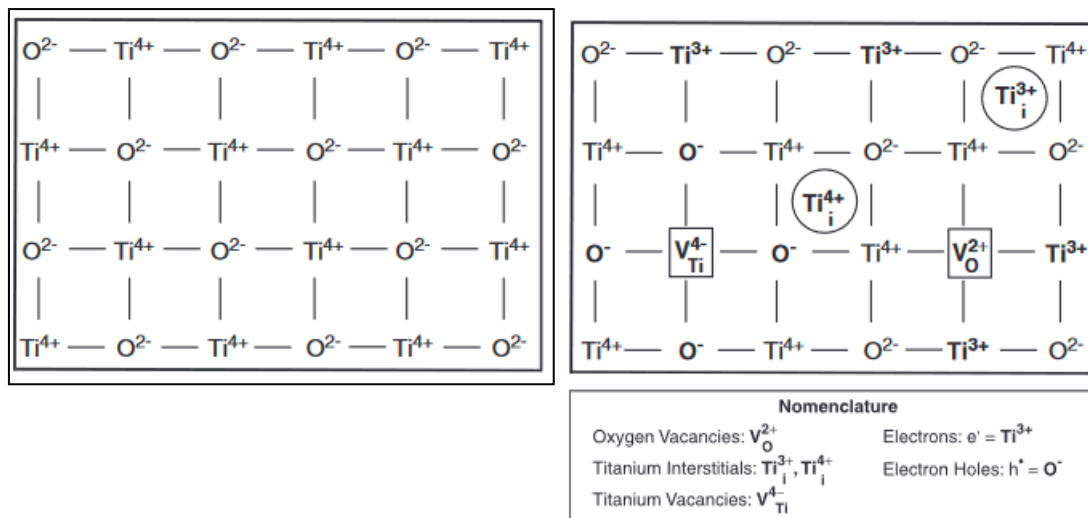


Figure I.10. Schematic of an ideal TiO₂ lattice **a)** that is free of point defects (stoichiometric) and **b).** A lattice involving point defects in both cation and oxygen sublattices (defect disorder).

Examining the impact of defect disorder on the properties of TiO₂, encompassing electrical properties as well as other properties associated with defects (**Fig.I.11**) was created solely for the purpose of providing a simple illustration of point defects. The (**Fig.I.10.a**) shows a simplified schematic of a crystalline lattice for TiO₂. In this idealized representation, there are alternating titanium Ti⁴⁺ ions and oxygen O²⁻ ions arranged in a periodic structure. (**Figure I.10.b**) shows a schematic representation of a titanium dioxide TiO₂ lattice that includes various point defects, indicating a non-stoichiometric condition or defect disorder and includes several types of defects.

The electrical conductivity (σ) of TiO₂ during the n-p transition regime comprises contributions from both electrons and electron holes:

$$\sigma = en\mu_n + ep\mu_p \dots\dots\dots (I.8)$$

Where, e represents the elementary charge, μ denotes mobility, while n and p stand for the concentrations of electrons and holes, denoted by the respective subscripts corresponding to the specific charge carriers.

I. 9. Applications of TiO₂

The bar chart in (**figure I.11**) from 2000 to 2023 reflects a consistent and significant scientific interest in the applications of TiO₂ thin films. Particularly in the past five years, a marked uptick in research publications can be observed.

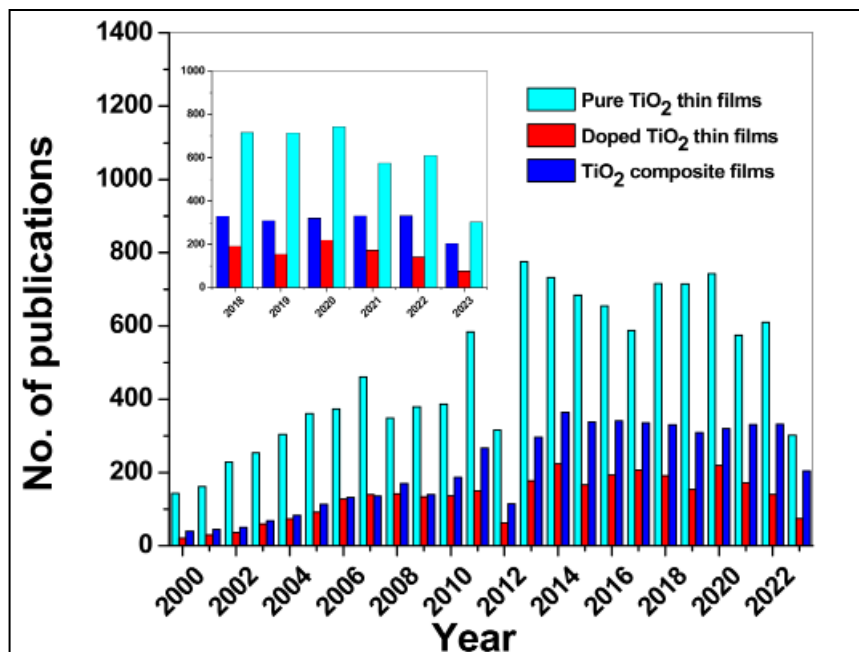


Figure I.11: A comparison of the number of publications on pure, doped, and composite TiO₂ thin films from 2000 to 2023. Inset: illustration of the last five years.

TiO₂ has a wide array of uses in various fields [50, 51, 52, 53]:

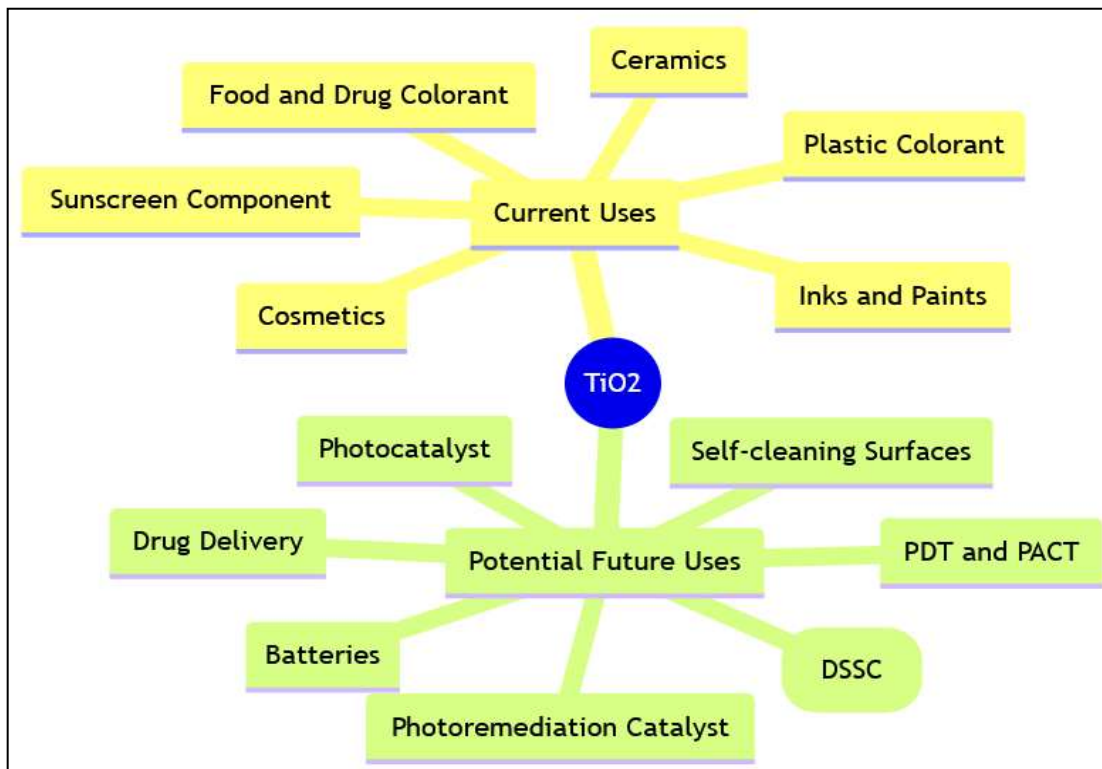


Figure.I.12. Application of TiO₂.

I. 9.1. Current uses of TiO₂

- a. **Food and Drug Colorant:** TiO₂ is used as a white pigment (E171 when used as a food colorant) to enhance the appearance and brightness of food products and pharmaceuticals. World production of TiO₂ exceeded 9 million tonnes in 2014, indicating its widespread use.
- b. **Sunscreen:** TiO₂ reflects the sun's harmful rays, protecting skin against damage and possibly cancer. It has been safely used in cosmetics for many decades and is approved by various safety agencies in the US as an over-the-counter drug. It uses UV blocking agents to reduce harmful radiation before it reaches the skin.

- c. **Cosmetics** TiO₂ plays an important role in enhancing coating strength and sun protection. Known for its unmatched coating power, TiO₂ is a preferred alloy for cosmetic products, including foundations and eye shadows. The development of skin care products has led to the development of products specifically designed to combat skin irritation. Among these, topical formulations containing antimicrobial agents such as azelaic acid have attracted considerable research attention.
- d. **Ceramics:** TiO₂ is known to be used in ceramics to improve whiteness and opacity, as well as to enhance mechanical properties.
- e. **Plastic Colorant:** TiO₂ is commonly used as a colorant in plastics, contributing to the material's whiteness, opacity, and UV resistance.
- f. **Inks and Paints:** As a pigment, TiO₂ is used in inks and paints for its ability to provide opacity and durability, thereby protecting substrates from UV light.
- g. **Self-Cleaning Surfaces:** The photocatalytic properties of TiO₂ allow it to break down organic matter when exposed to UV light, leading to self-cleaning surfaces.

I. 9.2. Potential Future Uses of TiO₂

- a. **Photocatalyst** is the use of photon energy, typically from sunlight's UV rays, within the catalyst medium to facilitate chemical reactions. This process is particularly significant in environmental remediation efforts, including water and air purification, where it breaks down pollutants under UV light exposure. TiO₂, a semiconductor with a fully occupied valence band and a wide band gap, absorbs UV light with wavelengths below 400 nm. This inherent limitation has spurred extensive research aimed at extending its absorption capabilities into the visible light spectrum. Strategies include modifying TiO₂ to sensitize it to larger band gaps or integrating it with semiconductors possessing smaller band gaps that can absorb visible light. UV light, especially with wavelengths shorter than violet light (400 nm), carries substantial destructive energy. When TiO₂ is exposed to such light, it gets activated, causing electrons to become excited and dislodge. These liberated high-energy electrons can break chemical bonds, making the process highly effective in decomposing organic substances, pollutants, and bacteria, thereby contributing to environmental cleanup efforts [54, 55].

- b. **Drug Delivery:** research is looking into using TiO₂ nanoparticles for targeted drug delivery systems due to their biocompatibility and stability.
- c. **Batteries:** TiO₂ based anodes for lithium-ion batteries are being researched to improve capacity and lifespan.
- d. **Photoremediation Catalyst:** TiO₂ could potentially be used in photoremediation to catalyze the degradation of pollutants in contaminated environments.
- e. **Dye-Sensitized Solar Cells (DSSC):** Research on TiO₂ role in DSSCs is ongoing, where it can help increase the efficiency of solar cells converting light to electricity.
- f. **Photodynamic Therapy (PDT) and Photoacoustic Therapy (PACT):** TiO₂ nanoparticles are being investigated for their potential use in medical therapies such as PDT and PACT to treat diseases by generating reactive oxygen species under light exposure.

II. 10. Metal oxides

II. 10.1. Synthesis of metal oxides

Since the mid-20th century, scientific and engineering research on transition metal oxides has attracted much interest (especially in environmental applications) due to their unique electrical, optical, gas sensor, photocatalytic, and mechanical characteristics [56]. Transition metals as electronic materials have birthed the next generation of rechargeable lithium-ion batteries. The use of oxides has been extensively studied due to their ability to increase energy and efficiency, as well as their design capabilities, safety, environment, friendliness, and low cost. However, the biggest challenge in using these materials for battery efficiency is their poor electronic wiring. Researchers have extensively investigated improving electronic connectivity by adding carbon coatings or other conductive connectors or fabricating nanoarchitected electrodes, but these methods often lead to little improvement in rate performance or face challenges with mass fabrication and high strength, which are examined. Transition metal oxides stand out particularly in this regard, such as TiO₂, Fe₂O₃, CuO, NiO, ZnO, SiO₂, Ga₂O₃, MnO₂, Cr₂O₃, and others [57, 58].

I. 10.2. Applications of metal oxides

So far, numerous metal oxides have been prepared via solid-state chemical methods and find application across diverse fields such as supercapacitors, gas sensors, solar cells, batteries, bioactivity, catalysis, semiconductors, ceramics, pigments, etc [20].

I. 10.3. Bulk structure

Transition metal oxides have a wide range of structures, compositions, and properties. However, a generalization can be made that the ionic radius of a transition metal is typically smaller than that of O^{2-} . As a result, most transition metal oxide structures consist of anions arranged in a cubic close packing pattern, with metal cations occupying the octahedral and tetrahedral (sites) within the oxide network. Transition metal oxides can be found in various crystal structures. Some of these oxides may have more than one crystal structure at room temperature [59].

I. 11. Doping of TiO_2

The optical response of any material is heavily influenced by its underlying electrical structure. For nanometer-sized materials, the electrical properties are directly related to their chemical composition (the chemical nature of the bonds between the atoms or ions), atomic arrangement, and physical dimension (carrier confinement). The chemical composition of TiO_2 can be changed through doping. To change the material's optical properties, swap either the metal (titanium) or the nonmetal (oxygen) component. It is preferable to preserve the crystal structure of the photocatalytic host material while producing favourable changes in electronic structure. It appears easier to substitute the Ti^{4+} cation in TiO_2 with other transition metals, and it is more difficult to replace the O^{2-} anion with other anions due to differences in charge states and ionic radii. The nanoparticle's small size is advantageous for the change of the chemical composition of TiO_2 due to the higher tolerance of structural distortion than that of bulk materials caused by the intrinsic lattice strain in nanomaterials [60].

I. 12. Zinc oxide (ZnO)

Transparent conducting zinc oxide (ZnO) is extremely attractive due to its good optical and electrical, chemical, thermoelectric, and mechanical properties shown in the **table I.4**, coupled with the low cost, non-toxicity, and abundance in nature of Zn [61]. ZnO is an n-type semiconductor material with a wurtzite crystal structure and a direct wide band gap of approximately 3.37 eV. It also has a high exciton binding energy of 60 meV at room temperature. Its other favorable properties include high electrochemical stability [20]. Another advantage of ZnO is that it can be easily etched using acid or alkalis, enabling the fabrication of miniaturized devices. Furthermore, by doping transition metals into ZnO, their electrical properties can be modified to suit specific requirements. In prior investigations, studies have also reported on the good electrical stability of ZnO thin films and their use as an air stable anode for organic light emitting diodes (OLEDs) [62].

Table I.4: Basic properties of zinc oxide [20, 61, 63, 64, 65, 66, 67, 68, 69, 70].

Parameters	ZnO Thin Films Value
Band gap	3.37 eV
exciton binding energy	60 meV
Density	5.606 g.cm ⁻³
Crystal structure	Wurtzite, rock salt, zinc blend
Z (Formula Units per Unit Cell)	2
Stable phase at 300K	Wurtzite
Melting point	1975°C
Nature of oxide	Amphoteric oxide
Lattice Parameters (nm)	a= 0.32495 nm, c= 0.52069 nm
Relative dielectric constant	8.66
Refractive index	2 at 600 nm
Solubility in water	0.16 mg 100 mL ⁻¹
Intrinsic carrier concentration	10 ²⁰ cm ⁻³
Melting Temperature (°C)	~1975
Hardness (Mohs Scale)	~4.5

I. 13. Coupling of TiO₂ with ZnO

To improve the efficiency of optoelectronics, researchers have been exploring the coupling of various oxides, such as WO₃, ZnO, SiO₂, SnO₂, Fe₂O₃, and MoO₃ [71]. Among these, ZnO is the best of these for coupling with TiO₂ because it has a similar photocatalytic mechanism and a band gap energy that is very close to that of TiO₂ (3.3 eV) [72]. Notably, ZnO exhibits higher electron mobility and a lower electron recombination rate compared to TiO₂, enhancing its electronic properties. The literature indicates that a ZnO layer on TiO₂ can significantly suppress electron recombination rates, particularly from TiO₂ to the electrolyte.

Aside from a single layer, in the context of solar cell applications, the combination of TiO_2 and ZnO into bilayer thin films presents a unique and promising approach [73]. The TiO_2/ZnO bilayer thin film is poised to offer excellent optical properties. These films are not only commonly utilized as electron transport layers (ETLs) [74], but their synergy also leads to enhanced charge transport [75]. This innovative combination leverages the strengths of both materials, potentially setting a new standard for optoelectronic efficiency in solar cell technology.

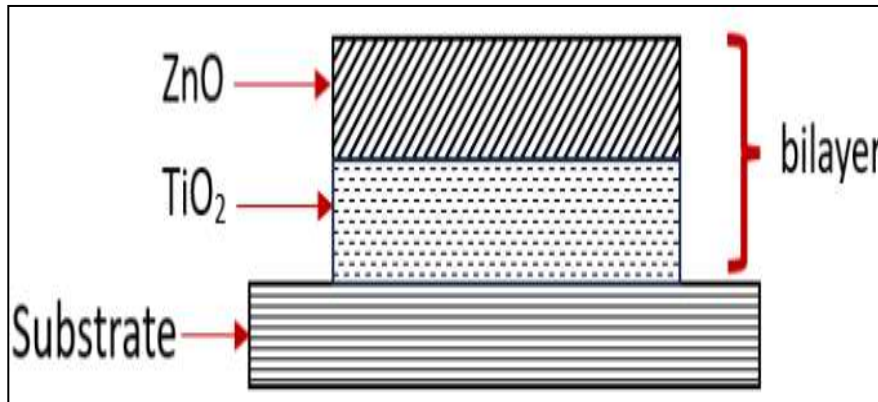


Figure II.13: illustration of TiO_2/ZnO bilayer thin film onto substrate

I. 14. Copper oxide

Copper oxides are semiconductors, low cost, deriving their versatility from the abundant natural supply of copper (Cu) and the straightforward synthesis achievable through copper oxidation. Specifically, nanostructured copper oxides display distinctive properties, rendering them appropriate for diverse applications (table.I.5), such as solar cells, serving as materials in sensors, heterogeneous catalysts, and influencing electrical and optical characteristics. In thin film applications, the prevalent copper oxides are cuprous oxide (Cu_2O) and cupric oxide (CuO) [76, 77, 78].

Table.I.5. various types of Copper oxides and their physical applications.

	Type	Band gap (eV)	Crystal structure	Application
Cu_2O	P	1.21–1.51	monoclinic	Solar Cells, Photodetectors, catalysis
CuO	P	2	cubic	Semiconductor Devices, photocatalyst due to its narrow band gap, battery Technology, gas sensors

I. 15. Iron Oxides

Iron oxides, also known as ferric oxides, are chemical compounds composed of iron and oxygen atoms. There are several different iron oxide compounds. Ferric oxide nanostructures, including Fe_2O_3 , have attracted significant interest due to their various physical properties, which depend on their composition and crystal structures. The normal stoichiometric forms of iron oxides are magnetite (hematite $\alpha\text{-Fe}_2\text{O}_3$, magnetite Fe_3O_4 , FeO , and BiFe_3O_4), (see **table.I.6**), usage as pigments [79, 80], small size, high magnetism, and low toxicity. These nanostructures have been widely used in various fields, such as medicine, cosmetics, food, magnetic storage devices, agriculture, wastewater treatment, and paint textiles [20].

Table.I.6. various types of iron oxide and their physical properties [81].

Composition (crystal structure)	ρ (Ωcm at 300 K)	T_N (K)	E_g (eV)	Physical properties
$\alpha\text{-Fe}_2\text{O}_3$ (corundum)	$\sim 3 \times 10^{-3}$	950	2.1-2.2	Photoelectrochemical response to visible light
Fe_3O_4 (spinel)	$\sim 10^{-2}$	860	-	Half metallicity
FeO (rock salt)	$\sim 3 \times 10^{-2}$	195	2.4-2.5	P-type semiconductor
BiFe_3O_4 (perovskite)	-	~ 640	2.3-2.1	Multiferroicity, Photo-voltaic effect
RFe_2O_4 (2D triangular)	$\sim 5 \times 10^2$	~ 230	-	Multiferroicity (charge-order-type)
$\text{R}_3\text{Fe}_5\text{O}_{12}$ (garget)	-	~ 600	2.7-3	Giant magneto- optical effects
$\text{MFe}_{12}\text{O}_{19}$ (magnetoplumbite)	-	~ 700	-	Hard magnetic material

I. 16. Coupling of TiO₂ with Fe₂O₃

Ferric oxide Fe₂O₃ is a semiconductor known to have a gap of about 2.22 eV, so it is easily excited by a wide range of light at wavelengths below 558 nm that cover much of the visible. Also, the Fe₂O₃ conduction band is ideally placed at a lower energy level than the TiO₂ conduction band, which gives it the quality of an electron acceptor capable of trapping the photogenerated electrons on the TiO₂ (possesses wide energy band gap) conduction band following an excitation of the latter. Ferric oxide Fe₂O₃ is often found in the degree of oxidation (III), Fe³⁺ ions are therefore the active elements in the coupled system. These ions also have an interesting property. They occupy a 0.79 Å radius volume almost equal to that of Ti⁴⁺ (0.75 Å), so they can be incorporated into the TiO₂ matrix. Ferric in its form of Fe₂O₃ oxide thus presents a good candidate for coupling with TiO₂ to reduce the phenomenon of electron/hole recombination [82].

Chapitre II: Nonlinear optics

Since we studied nonlinear properties (M-Lines), this chapter explains some of these nonlinear properties.

Laser technology has undergone decades of development, revealing significant advancements in our comprehension of generating and managing coherent and intense optical radiation. Our understanding has now reached unprecedented levels. Laser devices, in contrast to conventional light sources, offer highly directional, monochromatic, high brightness, and high photon degeneracy. The nonlinear interplay between laser beams and materials has resulted in the discovery of numerous new effects and phenomena, making the exploration of these effects and associated techniques the focal points of nonlinear optics research.

II.1 Principles of Guidance and Multimodal Fiber

Optical fibers are dielectric waveguides generally made of silica glass. They can be divided into three parts: the guiding core, the optical cladding, and the mechanical cladding, as illustrated in **Figure II.1**. Typically, the core is doped with inert ions included in the silica matrix, elevating its refractive index and allowing the electromagnetic wave to propagate through it via total internal reflection. The optical cladding, composed of undoped silica, confines the radiation within the core because of variations in refractive index. Finally, the mechanical cladding serves to protect the fiber from the external environment [83].

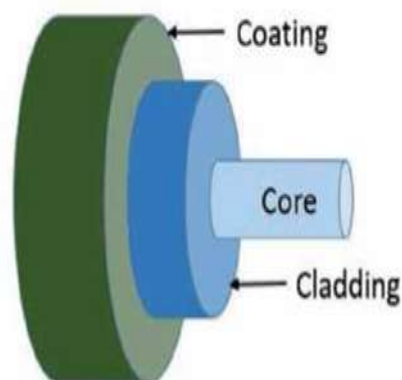


Figure II.1: Principal elements of an optical fiber [84].

It is possible to calculate the eigenmodes of the fiber by solving the Maxwell equations, as with any waveguide. In the case of optical fibers, it is possible to group transverse electric and magnetic modes (TE and TM), respectively, and hybrid modes (HE or EH) into sets of degenerate modes.

The prism coupler method, also known as the *M-lines* technique, is widely employed for assessing the optical characteristics of thin films. Enhancing current waveguide techniques for thin film parameter analysis and innovating new approaches enable the examination of the nonlinear optical characteristics of guiding films.

II.2 Nonlinear optics

Nonlinear optics (NLO) is the first and the most expansive field created as a result of the laser's invention. Nonlinear optics primarily explores novel optical phenomena and effects resulting from the interactions between concentrated coherent optical radiation and substances. The term "nonlinear optics" has historical significance, rooted in the fact that, before the 1960s, many fundamental mathematical equations in conventional optics exhibited a linear characteristic. To illustrate this linear aspect of traditional optics, let's examine three examples. Firstly, when interpreting phenomena such as refraction, dispersion, scattering, and birefringence in the propagation of light through a medium, a crucial physical quantity to consider is the electric polarization generated in the medium. In traditional optics, it was commonly assumed that the electric polarization vector \mathbf{P} was directly proportional to the electric field strength \mathbf{E} of an incident optical wave...

$$\tilde{p}(t) = \epsilon_0 \chi^1 \tilde{E}(t) \dots\dots\dots \text{(II. 1)}$$

The variable ϵ_0 represents the vacuum space permittivity and χ denotes the susceptibility of a specific medium. Maxwell's laws, based on this linear presumption, generate a series of linear differential equations that only include terms linearly proportional to the field ' \mathbf{E} '. Consequently, as light beams or various monochromatic components pass through a medium, they do not couple or affect each other in any way. Simply put, when multiple monochromatic light waves, varying in frequency, travel simultaneously via a medium, there is no generation of coherent radiation at any new frequency. (The tilde (\sim) represents a rapidly changing amount over time; quantities that remain constant change slowly, and Fourier amplitudes are represented without a tilde).

The optical reaction can be expressed as a generalization of equation (II. 1) by includes polarization. $\mathbf{P}(\mathbf{t})$ is a series of powers of the field strength $\mathbf{E}(\mathbf{t})$.

$$\tilde{\mathbf{P}}(\mathbf{t}) = \tilde{\mathbf{P}}^1(\mathbf{t}) + \tilde{\mathbf{P}}^2(\mathbf{t}) + \tilde{\mathbf{P}}^3(\mathbf{t}) + \dots \dots \dots \text{(II. 2)}$$

The values $\chi^{(2)}$ and $\chi^{(3)}$ represent the optical susceptibilities of the second and third orders, respectively. To simplify Eqs (II. 1) and (II. 2) we assumed fields $\tilde{\mathbf{P}}(\mathbf{t})$ and $\tilde{\mathbf{E}}(\mathbf{t})$ were values represented by scalars.

Second order polarization,

$$\tilde{P}^2(t) = \epsilon_0 \chi^2 \tilde{E}^2(t)$$

Differs from polarization of the third order

$$\tilde{P}^3(t) = \epsilon_0 \chi^3 \tilde{E}^3(t)$$

Furthermore, demonstrate that nonlinear optical second-order interactions solely arise in noncentrosymmetric crystals, i.e., crystals without inversion symmetry. Because fluids, amorphous solids (like glass), and significant number crystals have inversion symmetry, $\chi^{(2)}$ disappears identically. As a result, these substances cannot induce second-order nonlinear optical effects. Nonlinear optical effects of the third order, which are shown by a $\chi^{(3)}$ susceptibility, can happen in both crystals with inversion symmetry and noncentrosymmetric media [85].

The response $\tilde{P}^{(1)}$ occurs when the field is applied \tilde{E} has an amplitude comparable to the characteristic atomic electric field strength

$$E_{at} = e / (4\pi\epsilon_0 a_0^2)$$

Where e is the charge of the electron,

$$a_0 = 4\pi\epsilon_0 \hbar^2 / me^2$$

a_0 is the radius of the hydrogen atom according to Bohr

m represents the electron's mass , $\hbar = \frac{h}{2\pi}$, h represents Planck's constant.

We calculate E_{at} as $5.14 \cdot 10^{11}$ V/m. Under nonresonant stimulation, we anticipate that the susceptibility of the second- order $\chi^{(2)}$ will be about equal to $\chi^{(1)} / E_{at}$. In condensed matter systems, $\chi^{(1)}$ is of the order of unity. Therefore, we expect $\chi^{(2)}$ to be on the order of $1 / E_{at}$, or that $\chi^{(2)} \approx 1.94 \times 10^{-12} m / V$.

Similarly, we expect $\chi^{(3)}$ to be approximately $\chi^{(1)} / E_{at}^2$, which, in condensed matter, is approximately

$$\chi^{(3)} \approx 3.78 \times 10^{-24} m^2 / V^2$$

These forecasts are remarkably precise when compared to observed values of $\chi^{(2)}$ and $\chi^{(3)}$. It is advantageous to express $\chi^{(2)}$ and $\chi^{(3)}$ in relation to fundamental physical constants. In condensed matter, $\chi^{(1)}$ is of the order of unity. This finding can be explained empirically or rigorously by observing that $\chi^{(1)}$ is derived from the product of atomic number density and polarizability.

Condensed matter has a number density of $(a_0)^{-3}$ and a non-resonant polarizability equal to $(a_0)^3$. Based on this, we can conclude $\chi^{(1)}$ is on the order of unity. The above-mentioned formula for \mathbf{E} yields [86].

$$\chi^{(2)} \approx (4\pi\epsilon_0)^3 \hbar^4 / m^2 e^5 \text{ And } \chi^{(3)} \approx (4\pi\epsilon_0)^6 \hbar^8 / m^4 e^{10}$$

To describe nonlinear optical phenomena, the polarisation $\tilde{P}(t)$ is typically expressed depending on the electric field applied strength $\tilde{E}(t)$, as indicated in Eq. (II. 1). Polarisation is important in the modelling of nonlinear optical processes because it can operate as a source of additional electromagnetic field components over time. For example, it is found that the wave equation in a nonlinear optical medium frequently has the form

$$\nabla^2 \tilde{E} - \frac{n^2}{c^2} \frac{\partial^2 \tilde{E}}{\partial t^2} = \frac{1}{\epsilon_0 c^2} \frac{\partial^2 \tilde{P}^{NL}}{\partial t^2} \dots\dots\dots \text{(II. 3)}$$

Here, n represents the typical linear refractive index, while c stands for the velocity of light in a vacuum. This statement can be seen as a wave equation with inhomogeneous, with the

polarisation \tilde{P}^{NL} from the nonlinear response acting as a origin for the electric field \tilde{E} , $\frac{\partial^2 \tilde{P}^{NL}}{\partial t^2}$ represents the acceleration of the medium's charges.

The equation aligns with Larmor's theorem of electromagnetism, stating that accelerated charges emit electromagnetic radiation.

II.3 Materials for nonlinear optics

Nonlinear effects are pivotal in determining the frequency, enabling the transformation of optical radiation from one frequency to another and thereby expanding the range of potential applications. These effects rely on specific materials with nonlinear properties. Our long-term objective is to achieve optical functions at short wavelengths through frequency conversion, with a focus on nonlinear that are second-order phenomena that can only take place in materials non-centrosymmetric [87].

The required properties of materials for the envisaged application are as follows:

1. High NLO coefficients to achieve significant conversion rates,
2. Wide transparency range for the relevant wavelengths, particularly in the UV,
3. High optical damage threshold for use in high-power lasers,
4. Moderate to very low birefringence,
5. Low walk-off angle to prevent divergence of the produced light beam,
6. Bandwidth, angular, spectral, and temperature tolerance to expand the range of operating conditions,
7. Good chemical stability,
8. Good mechanical stability,
9. Simplicity of growth to promote industrial production,
10. Low cost for broad utilization.

II.4 Fiber characteristics

This section outlines the distinctive characteristics of optical fibers and their significance in the investigation of nonlinear optical phenomena [88].

II.5 Nonlinear fiber optics

The inquiry into the use of fibers in nonlinear optics stems from the limitations of prevalent nonlinear materials like silica glass. Silica glass lacks significant second-order susceptibility due to the inversion symmetry in SiO₂, leading to its predominant nonlinear effects being controlled by the third-order susceptibility $\chi^{(3)}$. However, these effects are notably smaller compared to various crystals and liquids, in silica fibers, involving Raman- and Brillouin-gain coefficients exhibiting quantities significantly lesser than other commonly used nonlinear media.

The solution to this challenge lies in the extended distances over which fibers can sustain elevated intensities optical. Despite the modest values of nonlinear coefficients, optical fibers demonstrate nonlinear effects at modest power levels. This capability is attributed to two essential traits of single-mode fibers: a diminutive spot size (mode diameter <10 μm) and exceptionally minimal losses (less than 1 dB/km) within the wavelength from 1.0 to 1.6 μm [89, 90].

Optical intensity, denoted as I_0 , and L_{eff} , which represents the effective length sustaining high intensity, are crucial factors in this context. When light is concentrated onto a region with a radius w_0 , the relationship holds

$$I_0 = P_0 / (\pi w_0^2) \dots\dots\dots (II.4)$$

Where P_0 signifies the incident optical power. It is evident that focusing light to reduce w_0 enhances I_0 . Yet, this tight focusing leads to a reduced L_{eff} due to the diminishing length of the focal region.

$$(I_0 L_{\text{eff}})_{\text{bulk}} = \left(\frac{P_0}{\pi w_0^2} \right) \frac{\pi w_0^2}{\lambda} = \frac{P_0}{\lambda} \dots\dots\dots (II.5)$$

In the case of a Gaussian beam, $L_{\text{eff}} \approx \pi w_0^2 / \lambda$, and this product remains independent of the size of the spot w_0 . For a single mode fiber, the spot size w_0 depends on the core diameter and the refractive index contrast between the cladding and core. Notably, a consistent the size of the spot can be preserved throughout the complete length of the fiber L . In this scenario, the effective interaction length L_{eff} is restricted by the fiber's loss parameter

α . The relationship $I(z) = I_0 e^{-\alpha z}$ is employed, where I represents the intensity of the beam, and z is the variable indicating the direction of propagation, α is a constant within a specific medium [89, 91]. This expression suggests that for a given propagation length of $z = L$, the transmitted intensity $I(L)$ is directly proportional to the initial intensity $I=I(0)$. Consequently, the product $I_0 L_{eff}$ is established [89].

$$(I_0 L_{eff})_{fiber} = \int_0^L I_0 e^{-\alpha z} dz = \frac{P_0}{\pi w_0^2 \alpha} (1 - e^{-\alpha L}) \dots\dots\dots (II.6)$$

A comparison of equations (II.5) and (II.6), it becomes evident that, for optical fibers of considerable length, the efficacy the outcome of a nonlinear process may enhanced by a factor.

$$\frac{(I_0 L_{eff})_{fiber}}{(I_0 L_{eff})_{bulk}} = \frac{\lambda}{\pi w_0^2 \alpha} \dots\dots\dots (II.7)$$

Assuming $\alpha L \gg 1$, a significant enhancement factor is observed in the visible region, reaching approximately 10^7 for specific parameters such as $w_0=2$, $\lambda=0.53 \mu m$, and $\alpha=2.5 \times 10^{-5} cm^{-1}$ (10 dB/km). In the wavelength vicinity of $1.55 \mu m$ ($\alpha=0.2$ dB/km), the enhancement factor can potentially reach 10^9 . This remarkable increase in the efficacy of nonlinear phenomena establishes silica fibers serving as an appropriate nonlinear medium for observing a diverse range of the impact of nonlinear phenomena at modest power levels.

When exposed to strong electromagnetic fields, a dielectric's reaction to light becomes nonlinear. The transparent area of optical fibres experiences The third-order susceptibility, $\chi^{(3)}$, causes the lowest order nonlinear effects. These phenomena include third-harmonic production, four-wave mixing (FWM), and nonlinearity in refraction. The most significant of them is nonlinear refraction, which refers to the intensity dependency of the refractive index. The fibre mode's effective refractive index follows a form [88].

$$\tilde{n}(w, I) = n(w) + n_2 I \dots\dots\dots (II.8)$$

II.6 Origin of Nonlinear Effects in optical Fibers

Nonlinear effects in **Figure II.2**, with the exception of SPM and CPM, benefit one channel while extracting energy from another. SPM and CPM solely influence signal phase, resulting in spectrum broadening and dispersion. Recent academic studies have focused on nonlinear effects in optical fibres [92].

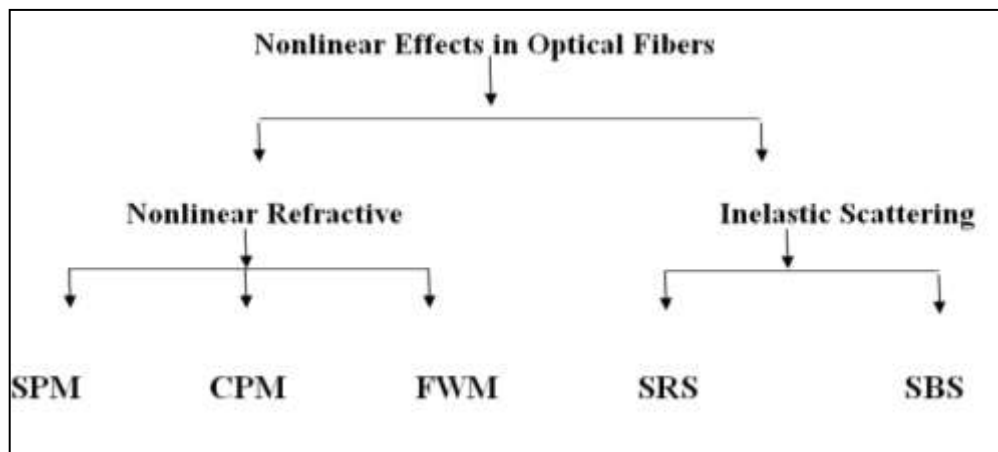


Figure II.2. Diagram of nonlinear effects in optical fibers.

II.7 Theory of Four-Wave Mixing

FWM is a form of optical **Kerr** effect, happening when light comprising two or more distinct wavelengths is thrown into a fiber. FWM occurs when light with three distinct wavelengths is launched into a fiber, resulting in the generation of a novel wave (referred to as an idler) with a wavelength that does not overlap with any of the other wavelengths. FWM is one example of optical oscillation parametric. Third-order polarization: $P^{NL} = \epsilon_0 \chi^{(3)}$. EEE (**Kerr** nonlinearity) [93, 94].

FWM is a nonlinear phenomenon that transforms energy from pump waves into signal and idler waves in **figure II.3**.

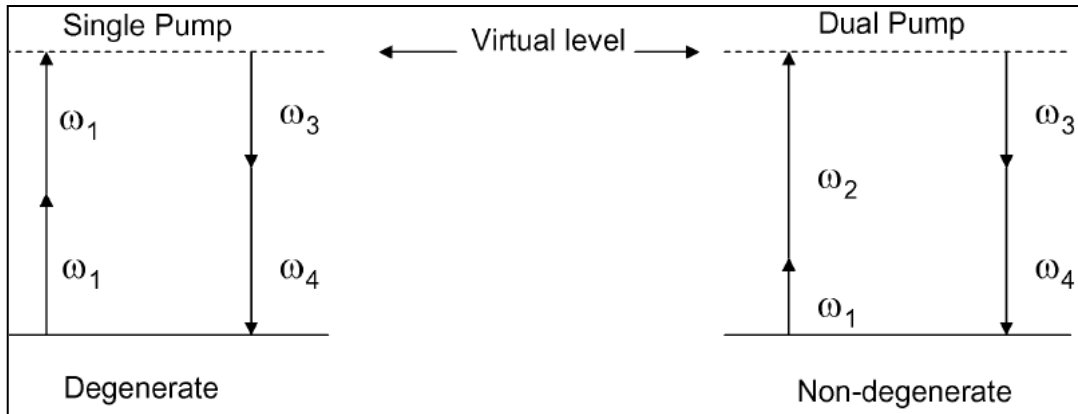


Figure II.3. Single pump and dual pump.

FWM mandates the conservation of (notation $E = \text{Re}[Ae^{i(\beta z - \omega t)}]$)

Energy $\omega_1 + \omega_2 = \omega_3 + \omega_4$

Momentum $\beta_1 + \beta_2 = \beta_3 + \beta_4$

Degenerate FWM: Single pump ($\omega_1 = \omega_2$).

$$E = \frac{1}{2} \hat{x} \sum_{j=1}^4 F_j(x, y) A_j(z, t) \exp[i(\beta_j z - \omega_j t)] + c.c. \dots\dots\dots (II.9)$$

The four slowly varying amplitudes satisfy

$$\frac{dA_1}{dz} = \frac{in_2\omega_1}{c} \left[\left(f_{11}|A_1|^2 + 2 \sum_{k \neq 1} f_{1k}|A_k|^2 \right) A_1 + 2f_{1234}A_2^*A_3A_4e^{i\Delta kz} \right] \dots\dots\dots (II.10)$$

$$\frac{dA_2}{dz} = \frac{in_2\omega_2}{c} \left[\left(f_{22}|A_2|^2 + 2 \sum_{k \neq 2} f_{2k}|A_k|^2 \right) A_2 + 2f_{2341}A_3^*A_4A_1e^{i\Delta kz} \right] \dots\dots\dots (II.11)$$

$$\frac{dA_3}{dz} = \frac{in_2\omega_3}{c} \left[\left(f_{33}|A_3|^2 + 2 \sum_{k \neq 3} f_{3k}|A_k|^2 \right) A_3 + 2f_{3412}A_4^*A_1A_2e^{-i\Delta kz} \right] \dots\dots\dots (II.12)$$

$$\frac{dA_4}{dz} = \frac{in_2\omega_4}{c} \left[\left(f_{44}|A_4|^2 + 2 \sum_{k \neq 4} f_{4k}|A_k|^2 \right) A_4 + 2f_{4312}A_3^*A_1A_2e^{-i\Delta kz} \right] \dots\dots\dots (II.13)$$

II.8 Single-Mode Fiber

In a single-mode fiber, the size of the spot w_0 is dictated by both the core diameter and the contrast in refractive index between the core and cladding. The optical fiber is comprised of a slender of glass yarn, with a central core covered by a sheath with a refractive index marginally lower than the core both the core and cladding are composed of silica spent, a vitreous substance of about $1.5 \mu\text{m}$ a it loses very little (roughly 0.2 dB/km) within the near-infrared (NIR). Is well known for the difference in refractive index between the core and cladding, which includes the choice of the dopant during fabrication. Dopants like P_2O_5 and GeO_2 are used to increase the refractive index of pure silica, making it suitable for the core. In contrast, coatings are made with materials such as boron and fluorine that reduce the refractive index of silica. Even a modest difference in refractive index between the core and cladding, usually below 1%, facilitates along the length of the fiber via the established principle of total internal reflection. The optical fiber's guiding characteristics are quantified by a unitless parameter defined as

$$v = a(w/c)(n_1^2 - n_2^2)^{1/2} \dots\dots\dots (\text{II.6})$$

In the given formula, with "**a**" representing the radius of the core, " **ω** " denoting the light's frequency, and both the core and cladding contain refractive indexes of " **n_1** " and " **n_2** ", **V** plays an essential role in determining the the supported modes of the fiber. When $V < 2.405$, the optical fiber exclusively supports a single mode and is categorized as a single-mode fiber. These fibers typically feature a microscopic core (**$a < 5 \mu\text{m}$**) and find widespread use in various applications, particularly in optical communications.

Chapitre III: Experimental Procedures.

This chapter is devoted to outlining the experimental technique employed throughout this thesis. The subsequent sections primarily concentrate on the techniques utilized for sample preparation and characterization. Each instrument's fundamental principles and setup are succinctly explained. Notably, all samples have been prepared as thin films, deposited onto either glass or silicon substrates.

III.1. Experimental protocols

Glass is a compelling choice for the field of integrated optics due to its inexpensiveness, exceptional transparency, and ability to withstand optical damage. Additionally, glass is highly rigid, and its amorphous nature allows for the production of polarization insensitive components. Also, most glass materials used in integrated optics have almost the same refractive index as optical fibers. This means that there aren't many losses when light travels through glass waveguides and optical fibers. Also, silicon is an ideal substrate for imaging, experimentation, and micro-fabrication applications. It is supplied as wafers, diced wafers, or smaller chips (pieces). Silicon resembles glass in biological applications, making it an appropriate substrate for cell growth and/or mounting. Thin films were deposited on both glass and silicon substrates (see **Table.III.1**). A comparison of glass substrate and silicon substrate.

Table.III.1: comparison of glass substrate and silicon substrate [95, 96, 97].

property	Glass Substrate	Silicon Substrate
Material Composition	Made of silica (SiO ₂) and other elements.	Pure elemental silicon.
Electrical Conductivity	Insulator does not conduct electricity.	Semiconductor, conductivity can be modified with doping.
Thermal Conductivity	Glass has a lower thermal conductivity compared to that of silicon and varies depending on its composition. The thermal conductivity of glass can vary significantly depending on the type, such as soda-lime glass, which is around [1-2] W/mK at room temperature, and borosilicate glasses, which typically have slightly higher thermal conductivity, ranging from [1.1-1.5] W/mK.	Its higher conductivity makes it suitable for heat-sensitive applications. At room temperature, single-crystal silicon typically exhibits a thermal conductivity of approximately 150 W/mK.
Optical Transparency	Transparent in visible and near-infrared spectrums.	Opaque in visible light, transparent in infrared.
Mechanical Strength	Varies with type (e.g., annealed, tempered), generally less robust than silicon.	Higher, more robust and resistant to mechanical stress.
Thermal Expansion Coefficient (CTE)	Higher thermal expansion coefficient than silicon ranges from around [5×10^{-6} - 10^{-5}] /°C.	Lower, which is advantageous for high-temperature processes is approximately 2×10^{-6} /°C.
Cost	Generally less expensive than silicon.	More expensive, cost influenced by purity and manufacturing process.

III.1.1 Steps for Cleaning Substrates

III.1.1 Steps for Cleaning Substrates

1. Glass substrate

The glass substrates were cleaved by a special pen, either manually or with a micro-cutting machine, with surfaces approximately $\sim 2.5 \text{ cm}^2$ and a thickness of 1 mm. The glass substrates can be cleaned by following these steps:

- Rinse with distilled water and then with acetone for 15 minutes;
- Rinse with distilled water;
- Wash the glass in methanol at room temperature in an ultrasonic bath for 15 min to remove any contaminants;
- then clean them in a bath of distilled water in the ultrasonic bath;
- Dry the glass substrates using optical paper to ensure that no water remains.

2. Si substrate

HF (hydrofluoric acid) is employed to eliminate native SiO_2 from the si substrate. Due to its hazardous nature, it is crucial to wear protective equipment while using HF, as it is a dangerous chemical. We prepare 1 HF: 10 H_2O . It is important to avoid using a glass beaker when working with HF, as HF has attacks on glass. The process involves dipping si substrate in the HF solution for 2 min, followed by a wettability test with distilled water rinse or blow dry.

III.2. Synthesis procedure thin films

III.2.1 Materials

Undoped and doped thin films were synthesized by the soft chemical method sol-gel by spin coating technique. The reactants (sol-gel) used are listed below in **table.III.2**

Table.III.2 List of chemicals employed in the study.

Name	Formula	source	Purity (%)	Density(g/cm ³)
Titanium isopropoxide (TTIP)	Ti(OCH(CH ₃) ₂) ₄	Aldrich	97	0.96
Isopropanol	CH ₃ CHOH CH ₃	Prolabo	99.99	0.786
Zinc acetate dihydrate	C ₄ H ₁₂ O ₆ Zn.2H ₂ O	Biochem	99.99	1.735
copper(II) diacetate hydrate	(Cu(CH ₃ COO) ₂ ·H ₂ O)	Biochem	98	1.88
Acetic acid	CH ₃ COOH	Prolabo	99.99	1.05
Methanol	CH ₃ OH	Prolabo	99.99	0.792
Diethanolamine	HN(CH ₂ CH ₂ OH) ₂	Biochem	99	1.097

III.2.2 Deposition by Sol-Gel

Thin films are deposited using a spin-coating apparatus in the sol-gel process. **Figure III.1** presents a photograph of the specific device used for this purpose.



Figure.III.1. Experimental spin coating device for thin films.

III.2.3 Synthesis of undoped TiO₂ film

The synthesis procedure for undoped TiO₂ film consists of adding TTIP mixed with isopropanol, and the mixture is vigorously magnetically stirred for 10 minutes at room temperature. Next, we added acetic acid and continued stirring for 15 minutes. Finally, we added several millilitres of methanol and continued stirring for an additional hour, which was then deposited on cleaned glass substrates by a spin coating method at a speed of 2000 rpm for 30 s for each layer, followed by preheating at 120 °C for 10 min to evaporate solvent content. The spin coating process was continued for 5 layers, and finally, the films were annealed at 500 °C for 90 min.

III.2.4 Synthesis of Zn-doped TiO₂ films

The experimental procedure for the synthesis of zinc-doped TiO₂ thin films involved dissolving it in a suitable methanol solvent, along with C₄H₁₂O₆Zn.2H₂O, to achieve the desired weight ratio of 3.7%. After that, the undoped TiO₂ solution, which was prepared beforehand, was added to the mixture. The resulting solution was then stirred for 1 hour. Afterward, the solution was applied onto cleaned glass substrates using a spin coating technique. Each layer was spin-coating at a speed of 2000 rpm for 30 seconds. To remove the solvent, the coated layers were preheated at 120 °C for 10 min. This spin coating process was repeated for a total of 5 layers. Finally, the films were subjected to annealing at 500 °C for 90 min, the resulting formation was Zn:TiO₂ with Zn²⁺/Ti⁴⁺ mass ratios of 3, and 7% wt.

III.2.5 Synthesis of metallic oxides and pair oxides based on TiO₂ thin films

Always, we used the same sol-gel method to synthesize of metallic oxides and pair oxides based on TiO₂ thin films (ZnO/TiO₂, and CuO/TiO₂ thin films). Titanium isopropoxide (TTIP), C₄H₁₂O₆Zn.2H₂O, and C₄H₈CuO₅ were employed as the sources of TiO₂, ZnO, and CuO, respectively.

III.2.5.1. Preparation of ZnO, and CuO solutions

- ✓ **For ZnO and CuO:** dissolve C₄H₁₂O₆Zn.2H₂O, and Cu (CH₃COO)₂·H₂O , respectively in a solvent ethanol and DEA was used as a catalyst

- ✓ Synthesis of (50% TiO₂:50% ZnO) and (50% TiO₂:50% CuO) thin films:

In a 1:1 volume ratio, mix the ready-made undoped TiO₂ solution with ZnO or CuO solutions.

- ✓ Synthesis of bilayer ZnO/TiO₂, and CuO/TiO₂ thin films:
 - Prepare a solution of undoped TiO₂ as described earlier.
 - Deposit a thin film of undoped TiO₂ onto the substrate using the deposition Spin-coating technique
 - Prepare a solution of ZnO, or CuO as described earlier.
 - Deposit a thin film of ZnO or CuO the respective onto the previously coated TiO₂ layer using the same deposition Spin-coating technique.

We used the spin coating method to deposit thin films of ZnO/TiO₂ and CuO/TiO₂. The thin films were deposited on glass and silicon substrates for 30 seconds at a speed of 2000 rpm. Subsequently, we preheated them at 200°C for 10 min to evaporate the solvent content. The spin coating process was repeated for five layers. Finally, we annealed the films at 500°C for 90 min using a Nabertherm muffle furnace with controller **figure III.2** to enhance their microstructure and, consequently, their optical characteristics.



Figure III.2. A photograph of the furnace for the thermal treatment.

III.3 Characterization of deposited thin films

III.3.1 X-ray Diffraction

X-ray diffraction (XRD) is an effective and non-destructive technique extensively employed as one of the most prevalent methods for analyzing and characterizing crystalline materials in the field of material science. XRD was used to analyze and characterize the crystallographic structure of a very wide range of sample types, such as minerals, nanomaterials, polymers, inorganic compounds, and to identify unknown materials, thereby highlighting the various crystalline phases present in films.

III.3.1.1. Principle of XRD

Relies on the constructive interference between monochromatic X-rays and a crystalline sample. In 1912, Max von Laue discovered that crystalline substances function as 3D diffraction gratings for X-ray wavelengths comparable to the intervals between planes in a crystal lattice. These X-rays are created using a cathode ray tube and then filtered to generate monochromatic energy. The radiation is subsequently collimated to concentrate and aimed at the sample [98]. The interaction between the incident photons and the sample results in constructive interference, leading to the production of a diffracted ray, contingent upon the fulfillment of Bragg's Law [99].

$$n\lambda = 2d \sin \theta \dots\dots\dots (III.1)$$

n: represents the integer, λ : wavelength, d: represents the interplanar spacing generating the diffraction, θ : Diffraction angle ($^{\circ}$). The analyses were performed on a BRUKER-AXS type D8 diffractometer, employing a $\text{CuK}\alpha$ radiation source with a wavelength of $\lambda = 1.54098 \text{ \AA}$. The X-ray tube cathode was powered at 40 KeV voltage and 40 mA current, while a scintillation counter detector was used. Film crystallinity was evaluated by measuring low-angle diffraction angles ranging from 0.5 to 1.5 degrees.

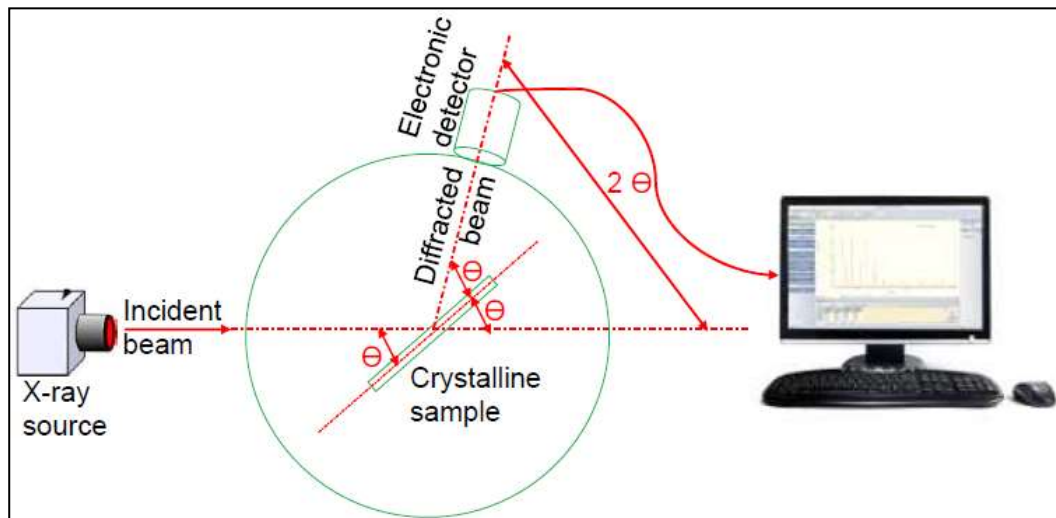


Figure.III.3 XRD instrument schematic.

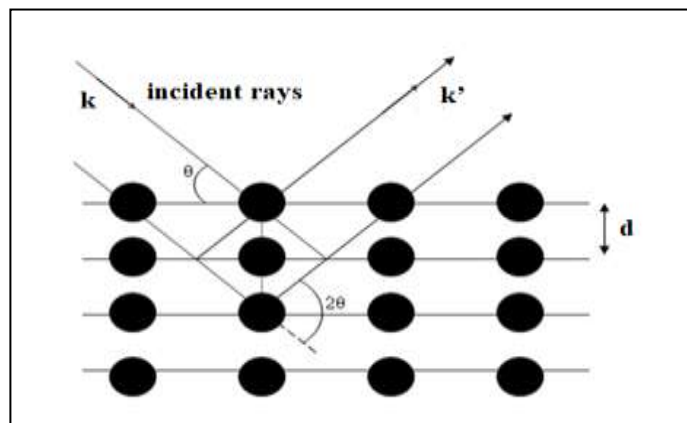


Figure.III.4 X-ray diffraction pattern by a family of lattice planes.

The diffractogram is a recording of the diffracted intensity based on the 2θ angle formed with the direct beam. The study of the diffractogram allows for obtaining a large amount of information about the structural and microstructural characteristics of the sample. This includes details about the crystalline structures of different phases, their proportions, the grain size, and rates of structural defects, macro and micro-strains, and the presence of texture [100]. Scherer's equation is used in the field of materials science to determine the crystallite size domains in a polycrystalline material using on X-ray diffraction data. The equation relates the broadening of X-ray diffraction peaks to the crystallite size and is particularly applicable to crystallites that exhibit broadened diffraction peaks due to their finite size.

The Scherrer equation is given by

$$D = \frac{k\lambda}{\beta \cos \theta} \dots\dots\dots (III.2)$$

Or modified Scherrer equation

$$\ln \beta = \ln \frac{k\lambda}{D \cos \theta} \dots\dots\dots (III.3)$$

The crystallite size (D) (Å) of the synthesized samples is established. Where k is a constant (typically between 0.9 and 1, depending on the crystallite shape), and (β) is the integral breadth (peak position /peak area) of the reflection peak, β: Full width at half maximum (FWHM) of the diffraction peak (in radians) [101, 102].

The strain ε values can be analysed utilizing the subsequent relationship:

$$\varepsilon = \frac{\beta \cos \theta}{4} \dots\dots\dots (III.4)$$

The provided equation by **Williamson and Smallman**, which uses a straightforward method of calculation, describes the dislocation density as the length of dislocation lines within the crystal per unit volume [103].

$$\delta = \frac{1}{D^2} \dots\dots\dots (III.5)$$

The lattice spacing d is determined using Bragg's formula

$$d_{(hkl)} = \frac{\lambda}{2 \sin \theta} \dots\dots\dots (III.6)$$

Comparing a diffraction pattern with **JCPDS files [No. 21-1272]** allows for the determination of lattice parameters. In the case of TiO₂ (tetragonal lattice for anatase and rutile), the

relationship between the interplanar distances of the (hkl) planes and the crystallographic parameters is as follows:

$$d_{(hkl)} = \frac{ac}{\sqrt{a^2c^2 + c^2(h^2 + k^2)}} \dots\dots\dots (III.7)$$

III.3.2 Raman spectroscopy

Raman spectroscopy is a technique employed for examining the rotational, vibrational, and other low-frequency modes of molecules. It provides information on the molecular structure and chemical composition of a material by measuring the scattering of light.

When a molecule interacts with monochromatic light, it undergoes two forms of light scattering, elastic and inelastic scattering. Elastic scattering refers to the state where the photon's frequency, wavelength, and energy remain unchanged. On the contrary, inelastic scattering involves a change in the frequency of the photon caused by the excitation or deactivation of molecular vibrations. This change in frequency can lead to the photon either losing or gaining a certain quantity of energy. Consequently, three different phenomena can occur [104], as illustrated in **figure.III.5**

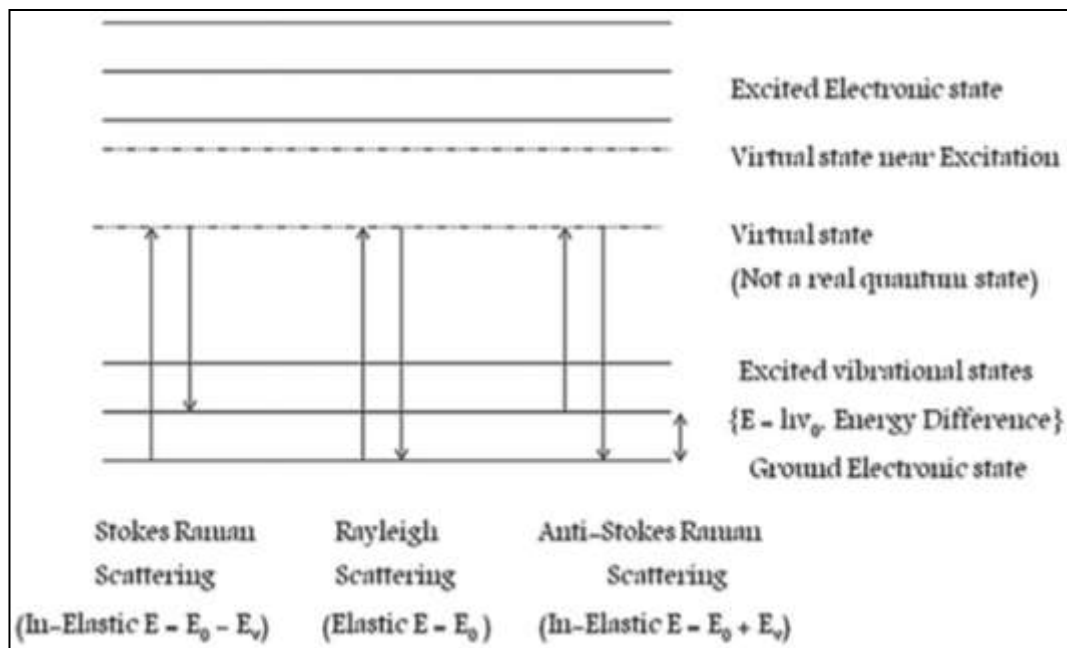


Figure. III.5. Mechanism of Raman scattering.

III.3.2.1 Rayleigh scattering

Occurs when light is incident on a molecule and interacts with it, yet there's no overall energy exchange ($E=0$). Consequently, the frequency of the dispersed light remains equal to that of the incident light ($E = E_0$).

III.3.2.2 Anti-Stokes Raman scattering

It occurs when light interacts with a molecule, resulting in the transfer of energy equal to one molecular vibration. If the interaction causes the light photon to acquire vibrational energy from the molecule, the frequency of the scattered light will be greater than the frequency of the incident light ($E = E_0 + E_v$).

III.3.2.3 Stokes Raman scattering

It occurs when the interaction between the light and the molecule causes the molecule to gain energy from the photon. This results in a scattered light frequency that is lower than the incident light ($E = E_0 - E_v$).

III.3.3 UV–Vis spectroscopy

UV-Vis spectroscopy is a versatile and non-destructive technique that offers valuable insights into the electronic characteristics of materials. This technique finds applications across various scientific fields and industries. It involves analyzing the absorption or transmission of specific UV or visible light wavelengths by a sample, comparing it to a reference or blank sample. For certain molecules and atoms, incoming photons possess adequate energy to induce transitions between distinct electronic energy levels. The absorbed light's wavelength matches the energy needed to elevate an electron from a lower to a higher energy level. These shifts lead to absorbance bands of narrow width at wavelengths distinctive of the energy level discrepancy of the absorbing species. However, for molecules, vibrational and rotational energy levels are superimposed on the electronic energy levels. Due to the possibility of numerous transitions with varying energies, the bands are broadened.

The transmission curves of the studied thin films are obtained using a double beam spectrophotometer, UV-Vis type V-730, as shown in **Figure III.6**, controlled by a computer. It can perform a scan between 300 nm and 1000 nm.



Figure.III.6. V-730 Uv-visible spectrophotometer.

The device measures the amount of light absorbed, transmitted, or reflected by the sample across each wavelength [105].

III.3.3.1 Optical phenomena of thin films

To assess the optical properties, we employ a grating spectrometer to measure transmission and reflection spectra. Subsequently, these spectra undergo analysis to extract information on absorption, refractive index, and film thickness. Two prominent characteristics within the films aid in determining thickness and band gap: strong interference and notable absorption at the band gap. The interference fringes result from internal reflections within the film. Examining the periodicity and size of these fringes in both transmission and reflection spectra enables the determination of film thickness (d). After establishing the thickness, absorption is deduced by eliminating the fringes from the transmission spectra, utilizing Beer's law equation (III.8), and solving for the absorption coefficient $\alpha(\lambda)$.

$$I = I_0 e^{-\alpha d} \dots\dots\dots (III.8)$$

III.3.3.2 The index refraction

The spectra characteristics of optical transmission in thin films at different wavelengths are illustrated. Utilizing *Swanepoel's* method, rooted in the concept proposed by *Manifacier et al.* [106], of forming boundaries around the interference maxima and minima **Figure. III.7** presents the optical transmittance within the range of 250–2500 nm of wavelengths for thin films.

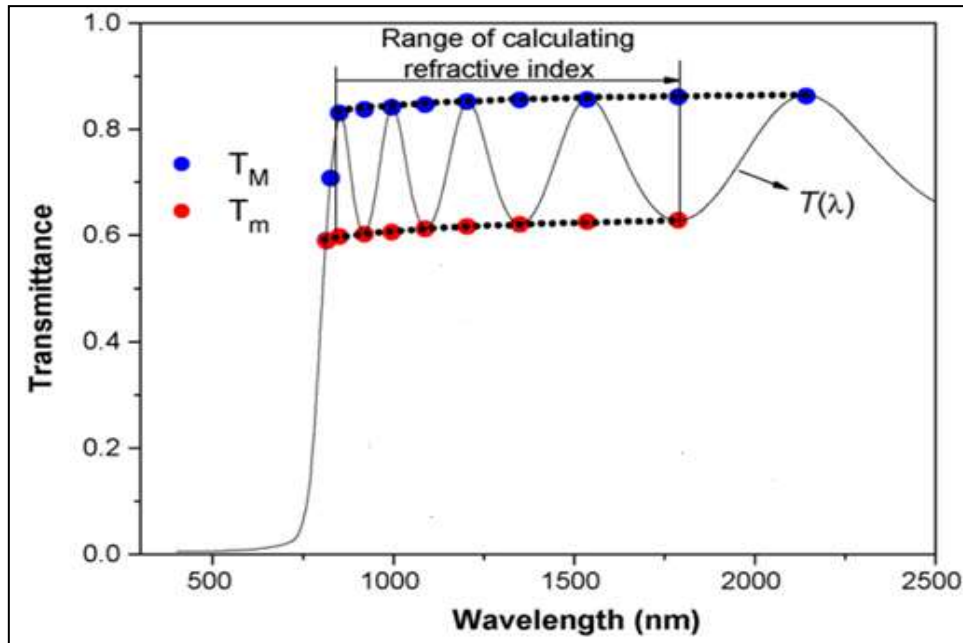


Figure.III.7 Transmission spectrum for thin films.

The refractive index values (n_1, n_2) can be determined for the film in the wavelength range where absorption is medium to weak. This calculation is performed using the following expression:

$$n_{1,2} = \sqrt{N + \sqrt{N^2 - n_s^2}} \dots\dots\dots (III.9)$$

Where:

$$N_{1,2} = 2n_s \frac{T_M - T_m}{T_M T_m} + \frac{n_s^2 + 1}{2} \dots\dots\dots (III.10)$$

T_M and T_m represent the maxima and minima of the envelope in the transmittance spectra, respectively, while n_s denotes the necessary refractive index values of the substrate. This can be calculated based on the transmittance spectrum of substrate T_s , utilizing the equation:

$$n_s = \frac{1}{T_s} + \left(\frac{1}{T_s} - 1 \right)^{1/2} \dots\dots\dots (III.11)$$

The precision of this initial refractive index estimation enhances following the computations of thickness d , as elucidated later. At this point, consideration must be given to the fundamental equation governing interference fringes.

$$2nd = m\lambda \dots\dots\dots (III.12)$$

In this context, the order numbers m take integer values for maxima and half integer values for minima. Additionally, if n_1 , n_2 represent the refractive index at two consecutive maxima (or minima) occurring at λ_1 and λ_2 , respectively, the expression defining the film thickness is as follows:

$$d = \frac{\lambda_1 \lambda_2}{2(n_1 \lambda_2 - n_2 \lambda_1)} \dots\dots\dots (III.13)$$

III.3.3.3 Band gap

The band gap is the smallest energy difference between the highest state in the valence band (VB) and the lowest state in the conduction band (CB). The strong absorption region points out the band gap. Determining the band gap involves employing the Tauc method. This method revolves around linearizing the absorption, assuming a parabolic density of states to be linearized through the use of a square-root function. When the conduction band aligns directly above the valence band, it's termed a direct gap transition in **FigureIII.8a**. In **figure III.8b**, the term "indirect gap" refers to the situation where the conduction and the valence band in momentum space are shifted in opposite directions. The absorption is linearized using the function $(\alpha E)^n$, where n is 2 for direct gap materials and 1/2 for indirect gap materials. To ensure dimensionless quantity, the coefficient for absorption α is multiplied by the energy E [107, 108].

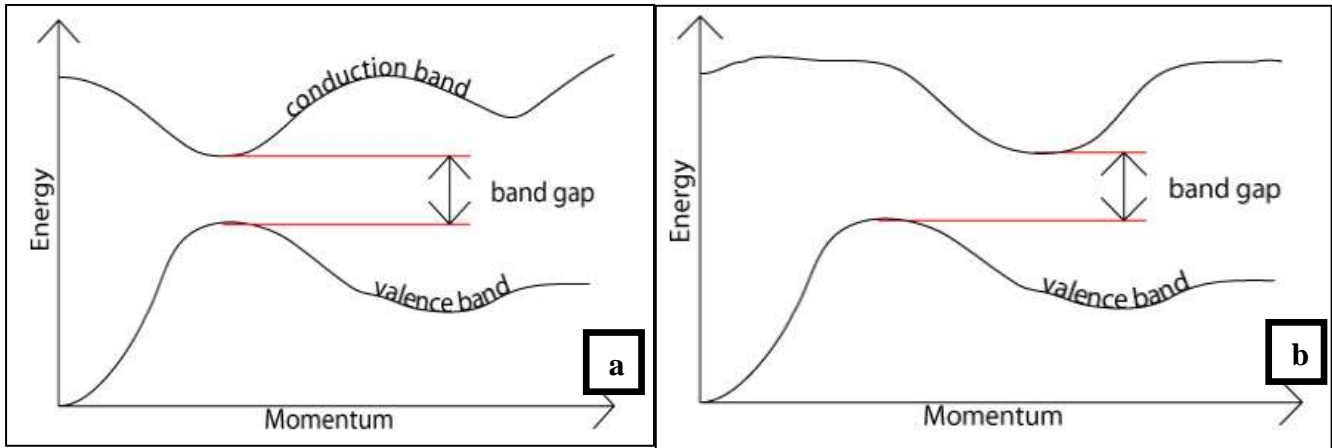


Figure.III.8 Comparison of indirect and direct band gaps.

III.3.3.4 Calculation of the band gap

The coefficient for absorption (α) values were determined utilizing Lambert's Law, expressed by the following equation

$$\alpha = \frac{1}{d} \ln\left(\frac{100}{T\%}\right) \dots\dots\dots (III.14)$$

Here, T represents the transmittance, and d denotes the thickness of the film. To determine the optical band gap E_g , we have used Tauc plot

$$(\alpha h\nu) = A(h\nu - E_g)^m \dots\dots\dots (III.15)$$

A is a function of the refractive index of the material, speed of light, and reduced mass, is a proportionality constant that depends on the substance [109], ν denotes the frequency of the light, h is energy of the photon, and E_g represents the optical band gap. Furthermore, Different authors [110, 111] have proposed varying values of m for different types of glasses. For the majority of crystalline semiconductors (direct transition), a common suggestion is $m = 1/2$ whereas in the case of the majority of amorphous semiconductors (indirect transition), the proposed value is $m = 2$.

III.3.4 Fourier Transform Infrared Spectroscopy (FTIR)

The favored technique for infrared (IR) analysis is FTIR. Is a spectroscopy technique that employs the mathematical method of Fourier transforms to analyze the wavelengths absorbed by materials.

III.3.4.1 Principle of FTIR

In FTIR analysis, Infrared light emitted from the light source traverses a Michelson interferometer along the optical pathway. The Michelson interferometer consists of a beam splitter, a moving mirror, and a s fixed mirror. The beam splitter divides the light beam into two segments, each of which is reflected by the moving and fixed mirrors, respectively. before being recombined. As the moving mirror makes reciprocating movements, the optical path difference to the fixed mirror varies, causing the phase difference to shift over time. The Michelson interferometer recombines the light beams to create interference light. An interferogram records the intensity of the interference light, as well as the optical path difference along the horizontal axis. The computer then analyzes these data points backward to determine the absorption at each wavelength [112]. The schematic representation of FTIR is illustrated in **Fig.III.9**.

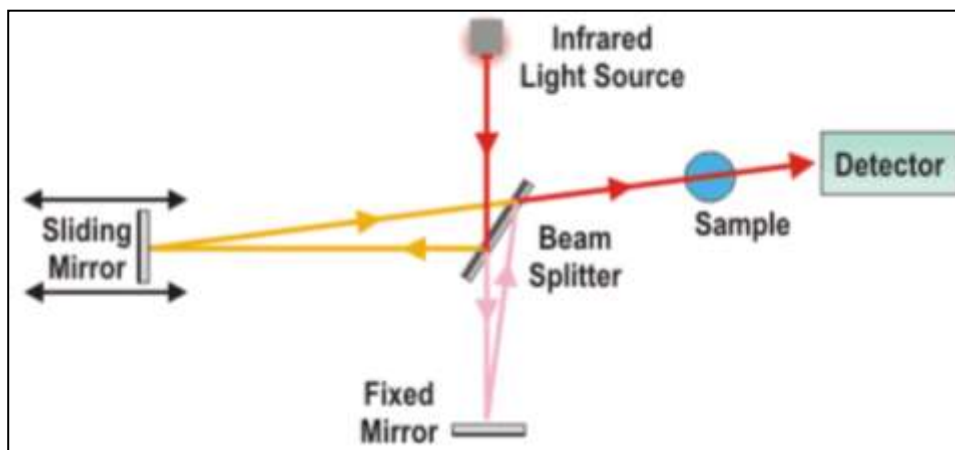


Figure III.9 The schematic depiction of FTIR <https://www.tribonet.org/wiki/fourier-transform-infrared-spectroscopy/>

III.3.5 M-line spectroscopy (MLS)

In this thesis, M-Line is a technique used in the study of guided optical modes in planar waveguide structures. This method is particularly common in the field of integrated

optics and photonics, where planar waveguides are essential components for guiding and manipulating light on a chip-scale platform. MLS stands out as one of the most precise methods for determining optogeometric characteristics such as waveguide film thickness and refractive index. It enables the determination of refractive index with a precision of up to 10^{-4} . The precision of measuring film thickness is similarly high, typically within the range of (10^{-2} - 10^{-3}). MLS employs a similar fundamental principle as prism coupling. Compared to alternative methods, MLS offers several advantages, including the demand for simple angular measurements, the advantages of MLS encompass determining the layer's anisotropy, alongside its non-destructive nature. Conversely, its drawbacks involve the necessity for the film to be sufficiently thick to sustain a minimum of two guided modes, the requirement for the substrate to be transparent at the specified wavelength, the layer's hardness to enable pressing against a prism's base, and the imperative to minimize the film's roughness to enhance accuracy.

The principle consists of coupling a laser beam into the guide to be studied. It usually employs solely utilizing a single wavelength (the most popular is 632.8 nm, He-Ne laser) via a prism (isosceles or straight) placed near the surface of the guide. The refractive n_p index of the prism is greater than the guide index n . Pressure is exerted on the back of the substrate using a pneumatic piston in order to optimize the air gap between the guide and the prism. The prism's base is where the incident beam converges, and it is there that it reflects with an angle of m , which is directly related to the angle of external incidence i_m according to Descartes' law. This total reflection is accompanied by the coupling point (where the air gap is adjusted) of an evanescent wave, which is coupled in the guide by the optical tunnel effect, a multi-wavelength MLS (MWMLS) has been created. **Figure III.10** shows the schematics of MLS and MWMLS. Using the step-index model, we can compute the refractive index n_f and thickness d of a thin layer [113].

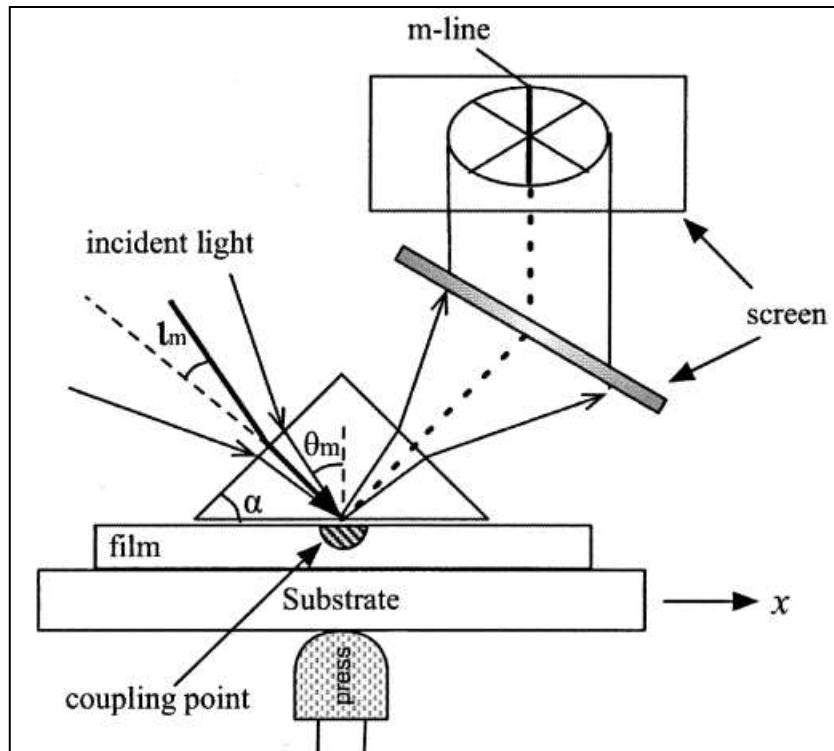


Figure.III.10. Scheme of prism coupling in the MLS and MWMLS apparatus [114].

III.3.6. scanning electron microscopy SEM

Is a potent analytical technique that combines the capabilities of SEM with various spectroscopic methods to obtain comprehensive data regarding the composition and characteristics of materials at the micro or nanoscale. SEM spectroscopy offers valuable insights into the elemental composition, chemical bonding, and electronic structure of a sample. The basic principle behind SEM spectroscopy involves the sample surface to bombardment using a concentrated beam of high-energy electrons generated by an electron gun for generating a topographic image and determining relative composition. When the electrons interact with the sample, various signals are emitted or generated, which can be identified and examined to collect information on the composition of the sample [115].

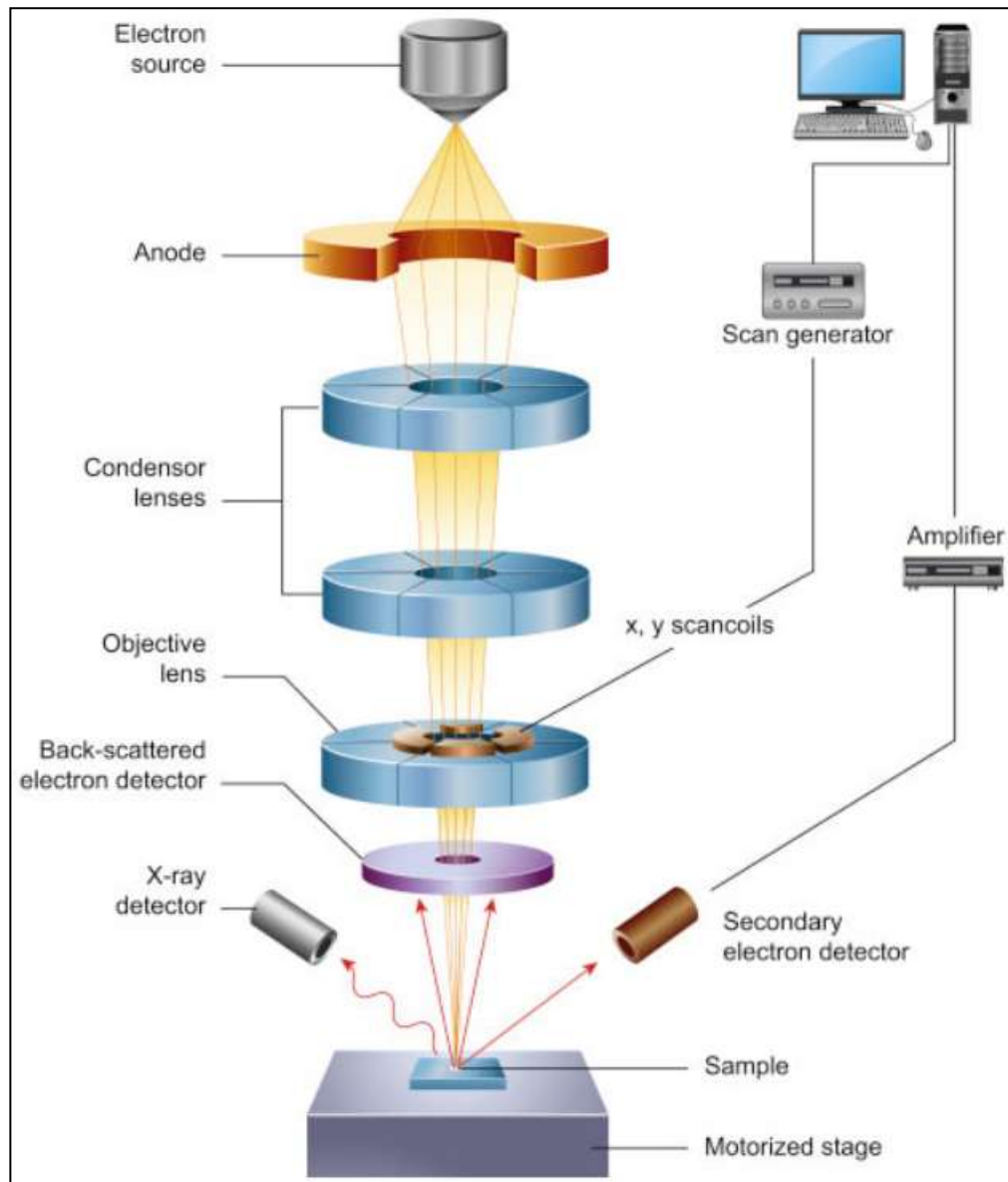


Figure.III.11. Schematic diagram of SEM [116].

The primary SEM components are:

1. Electron source (gun)
2. Condenser lenses
3. Objective lens
4. X-Y scan coils & scan generator
5. Detectors
6. Sample stage
7. Computer and display to view the images
8. External vacuum pump(s)

The electron gun emits electrons at the column's apex (**figure.III.9**), which subsequently undergo acceleration through the column via a predetermined accelerating voltage (ranging from 1 keV to 30 keV). Condenser lenses and apertures help to lower the beam diameter. The objective lens is the column's final lens, and it directs the beam towards the surface of the sample. The beam diameter in a SEM may range from less than 1 to 20 nanometers, contingent upon factors such as the electron gun, accelerating voltage, and lens arrangement. The electron beam's placement on the sample is regulated by scan coils positioned above the objective lens. These coils facilitate the beam's scanning across the surface of the sample along the X-Y plane. As the scanning beam interacts with the sample, it generates various signals including secondary electrons, backscattered electrons, and characteristic X-rays. These signals are subsequently captured by the corresponding detectors.

The most commonly used SEM techniques are Energy-Dispersive X-ray spectroscopy (EDS) and Electron Energy Loss Spectroscopy (EELS).

III.3.7. Energy Dispersive X-ray Spectrometry (EDX or EDS)

is a standard X-ray analytical technique utilized for analyze the chemical properties of samples by analyzing elements. When used together with SEM, the incorporation of an EDX detector enhances the amount of information about the sample compared to relying solely on SEM. EDX can provide the elemental atomic number of a sample. In a properly equipped electron microscopy (SEM, TEM) technique. The working principle of the technique of EDX involves focusing an electron beam onto a sample, leading to the transfer of some of the beam's energy to the atoms of the sample. If such a transition occurs, electrons in an inner shell become excited and create positively charged holes in lower energy shells. These voids subsequently draw in electrons with negative charges from higher energy orbitals. When the higher energy shells are filled with holes in the lower energy shell, the energy disparity resulting from this transition can be discharged in the form of an X-ray (**FigureIII.12**). An energy dispersive spectrometer can quantify both the number and energy of these emitted X-rays. The energy of the X-ray is distinct to the particular element and transition involved [98].

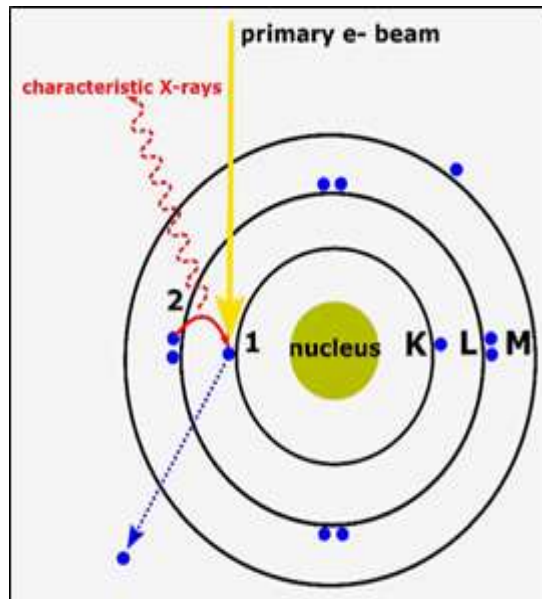


Figure.III.12. General Mechanism of emitting X-ray [117].

In order to obtain results, the X-rays produced in this process are gathered by a silicon drift detector (made from several Semiconductor materials including silicon Si and germanium Ge), which gauges the the signal and interprets it through software. Essentially, there are multiple formats to represent chemical information, such as line scans and elemental mapping. This approach enables the identification of each element present in a given sample using x-rays.

EDX analysis is now widely adopted in various industries, spanning manufacturing, research, energy and resource management, and consumer-packaged goods. Its practicality has grown to the extent that it has become an integral component of owning a SEM. By employing an SEM for EDX analyses, researchers can enhance production quality and save valuable time, making it an uncomplicated yet essential experiment in various applications.

III.3.8. Atomic force microscopy (AFM)

Is a vital imaging instrument for the fields of nanotechnology and biology [118]. It's an exceptional method that allows for the detection and measurement of surface structures with unparalleled resolution and accuracy. An AFM enables the capture of images showing the organization of individual atoms within a material or the configuration of individual molecules [119]. The capabilities of AFM have advanced to offer localized spectroscopic, chemical, and physical property information, alongside topographic imaging. We can gather

images as small as minute as 5 nm, which include merely 40–50 individual atoms, to analyze the crystal structure of materials, as well as images as vast as 100 micrometers.

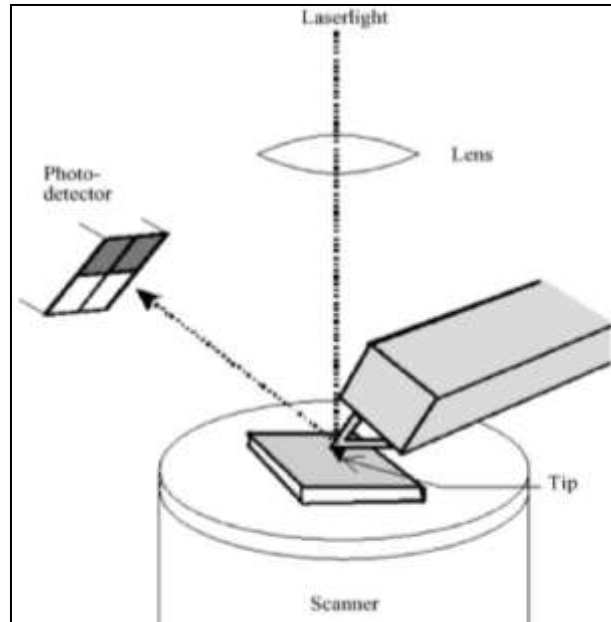


Figure.III.13. Schematic of an atomic force microscope [116].

AFM operates by maneuvering a sharp probe tip across the sample's surface and assessing the forces between the tip and the surface. These interactions give information about the sample's topographical, mechanical, and electrical properties. The concept of AFM relies on the interaction forces between tip and sample. The most frequent operational mode is contact mode AFM, wherein the tip directly contacts the surface. As the tip moves across the surface, it encounters both attracting and repulsive interactions among the atoms or molecules on the tip and those on the surface. These forces deflect a cantilever, which is a small beam attached to the tip. The cantilever's deflection is measured using a laser beam reflected off its back, and this data is utilized to build a picture of the surface [120].

Chapitre IV: Results and discussions

From the findings, two sections of results have been discussed which are fabrication of Zn-doped TiO₂ films and metallic oxides and pair of oxides based on TiO₂ thin films onto glass substrate by sol–gel spin coating method.

IV.1 Zn-doped TiO₂ thin films

This study utilized sol-gel method of spin-coating to synthesize Zn-doped TiO₂ films. The research delves into the film's structural, microstructural, and optical characteristics. However, it examines the waveguides of the Zn-doped TiO₂ films.

IV.1.1 X-ray Diffraction Analysis

XRD (Figure IV.1a, b, and c) results are compared with the TiO₂ data sheets from the American Society for Testing and Materials (ASTM) (JCPDS).

Figure.IV.1 displays the XRD patterns of films deposited on glass substrates as deposited and annealed at 500°C. The analysis of the undoped TiO₂ film in **Figure.IV.1a** reveals a diffraction peak at $2\theta = 25.18^\circ$. Indicating crystallization in the anatase (101) phase of TiO₂ is consistent with JCPDS files [No. 83–2243]. Additionally, in the same figure, a few weak diffraction peaks are also noticed, which refer to the anatase and brookite phases [JCPDS file No.76-1936]. It can be observed that the peaks at 36.06° and 47.88° correspond respectively to the crystalline planes (103), (200) of the Anatase phase of TiO₂, and the peaks at 30.25° and 46.14° correspond respectively to the crystalline planes (121), (032) of the Brookite phase of TiO₂ JCPDS file [No. 76–1936], *Li-ying QIAO et al.* [121]. A peak of brookite B (121) appears. The XRD diffraction peak is weak and broad, suggesting a low degree of crystallinity. While *Kuznetsova, I. N., et al.* [122]. They distinctly observed this peak in their XRD spectra, and *Tamgadge et al.* [123] also found this peak clearly in their XRD spectra, but did not index it. Furthermore, the brookite phase has consistently been commonly found with the anatase phase in TiO₂ thin films made using the sol-gel process [121, 124, 125].

Figure.IV.1b, the 3% wt. Zn-doped TiO₂ film exhibited two diffraction peaks at 2θ , values of 25.41° and 48.32° in the XRD patterns. These peaks showed reflections from the A (101) and A (200) crystal planes. However, because of the weakness of these anatase peaks and

incomplete, it is possible that the TiO_2 film only partially transitioned from a crystalline to an amorphous state. Further increases in zinc content prevented crystal formation in TiO_2 films. This may be attributed to an increase in lattice parameters caused by the substitution of Ti^{4+} (0.68 Å) with the larger ionic radius of the doping element Zn^{2+} (0.74 Å). Also, *Arunachalam et al.* [126] demonstrated that the formation of Zn-Ti-O linkages inhibits crystal growth.

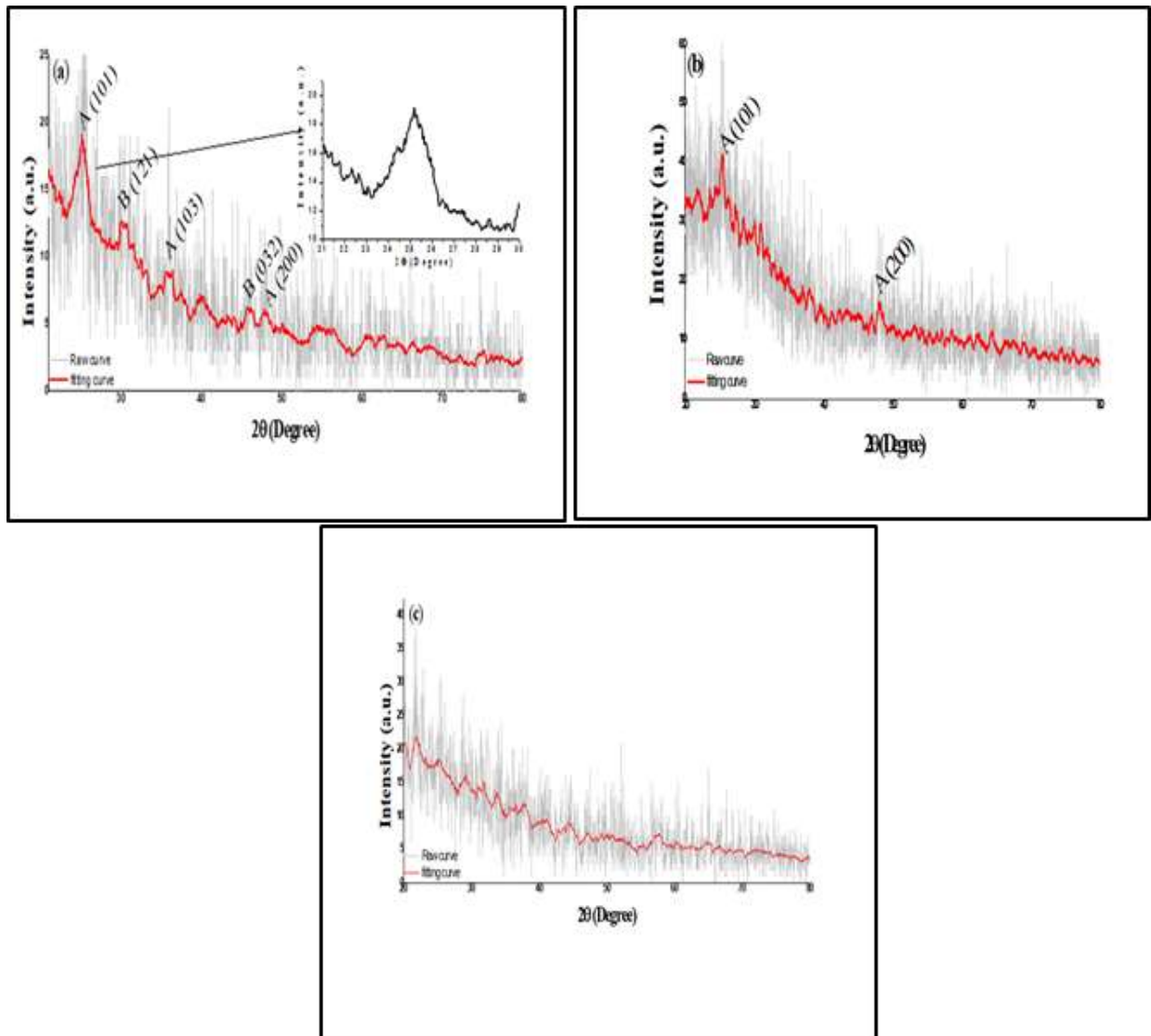


Figure.IV.1: XRD pattern of **a)** undoped TiO_2 thin films, **b)** 3wt. % Zn: TiO_2 thin film, **c)** 7wt. % Zn: TiO_2 thin film.

Further increases in zinc concentration prevented crystal growth in TiO_2 films. The film became amorphous because the zinc concentration was 7wt%. *Tang Bo-Wen et al.* [127] showed that the intensity of the diffraction peak A(101) diminishes as the quantity of Zn doping increases (according to varied $\text{Zn}^{2+}/\text{Ti}^{4+}$ atomic ratios ranging from 0 to 3% wt.),

while simultaneously increasing lattice distortion. Analysis of the entire FWHM and the strain of A (101) peak using relationship (III.4), the values are shown in the **table. IV.1** and using the Scherrer equation (III.2) produced grain sizes of 5.23 and 16.56 nm for undoped and 3 wt% Zn doped TiO₂ thin films. It is observed that as the doping concentration increases, so does the dislocation density, which is attributed to variances in ionic radii among Ti⁴⁺ and Zn²⁺.

Table.IV.1 Microstructural properties of Zn: TiO₂ thin films.

Sample	hkl	2θ (deg)	FWHM (rad)	Strain × 10 ⁻³ ε	d _{hkl} (Å)	crystallite size.(nm)	δ × 10 ¹⁵ (lines/m ²)
TiO₂ undoped	A(101)	25.18	0.2716	66.3	3.5340	5.23	36.5
3 wt% Zn doped TiO₂	A(101)	25.41	0.08	19.5	3.5028	16.56	3.64

Doping with zinc in TiO₂ thin films can lead to an increase in the crystallite size of the anatase phase. This effect is attributed to the incorporation of Zn atoms into the TiO₂ lattice, which can influence the growth kinetics of the anatase crystallites during film deposition or subsequent annealing processes. The presence of Zn atoms can act as a crystallization promoter, facilitating the formation and growth of larger anatase crystallites. It can be inferred that the addition of zinc dopant resulted in an increase in the crystallite size of the anatase phase and delayed of the transition from the amorphous phase to anatase.

IV.1.2 Morphology analysis

SEM images of undoped TiO₂ film and TiO₂ doped with 7% wt. Zn were annealed at 500 °C on glass substrates using the spin coating technique. The films' microstructure, as shown by SEM, generally revealed cracks. The surface of the films did contain voids, cracks, and any other serious defects, as shown in **Fig IV.2**, at the microscale due to strains during the drying technique spin coating or annealing step at 500 °C, but there is also a substantial variation between the undoped and doped states.

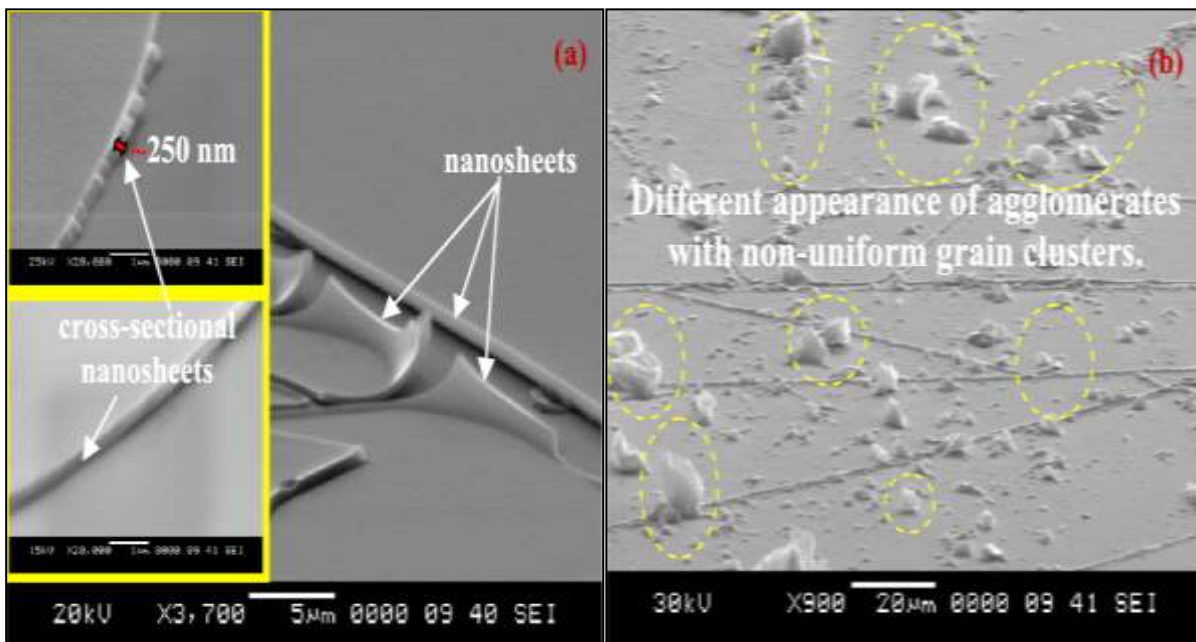


Figure.IV.2 SEM images of the: a) undoped TiO₂ and b) 7 wt% Zn: TiO₂ films.

The undoped TiO₂ films (**Fig.IV.2a**) had nanosheets ~250 nm thick with a compact morphology and granular particles, which are attributed to TiO₂ nanoparticles as shown in (**Fig. IV.2a**) and a smooth surface with defined edges. Zinc concentrations up to 7% **Fig.IV.2b** result in a completely different microstructure, with the production of discontinuously distributed particles on nanosheets with varying shapes and sizes, containing several agglomerates of microcrystals. Furthermore, as seen in the XRD patterns (**Fig.IV.1c**), high zinc doping at 7% in the titanium dioxide film hindered crystal growth, thus, the appearance of these agglomerates with visible grain clusters (**Fig.IV.2b**) is most likely connected to amorphous mixed oxides. Similar findings were observed by *Sreedhar et al.* [128]. The shapes are distorted as the doping concentration of the deposited films increases,

and the sizes are much larger than those in the undoped TiO₂ film as shown in **Fig.IV.2b**. Furthermore, the surface morphology of films in photocatalytic applications is an important element influencing the photoreaction on the Zn: TiO₂ surface, hence increasing surface roughness improves photocatalytic performance. *Karthick, A., et al.* [129].

IV.1.3 Optical analysis

Figure.IV.3 shows the optical transmission spectra of TiO₂ thin films with different Zn²⁺ doping concentrations in the wavelength range of 200-900 nm. At 350 nm, the transmittance of TiO₂ thin films with Zn²⁺ doping increases by approximately 10% compared to undoped TiO₂ films, resulting in interference fringes due to increased interactions between atoms or molecules [130]. *Sreedhar et al.* [128] observed a similar trend in the increase of transmittance (%) and the surface morphology of TiO₂ films, which is strongly dependent on Zn dopant concentration. The surface morphology of TiO₂ films gradually changed with the introduction of Zn²⁺ into the structure, which is in good agreement with the results obtained from SEM analysis. Undoped TiO₂ films have a relatively higher transmittance of about 90% at 500 and 600 nm.

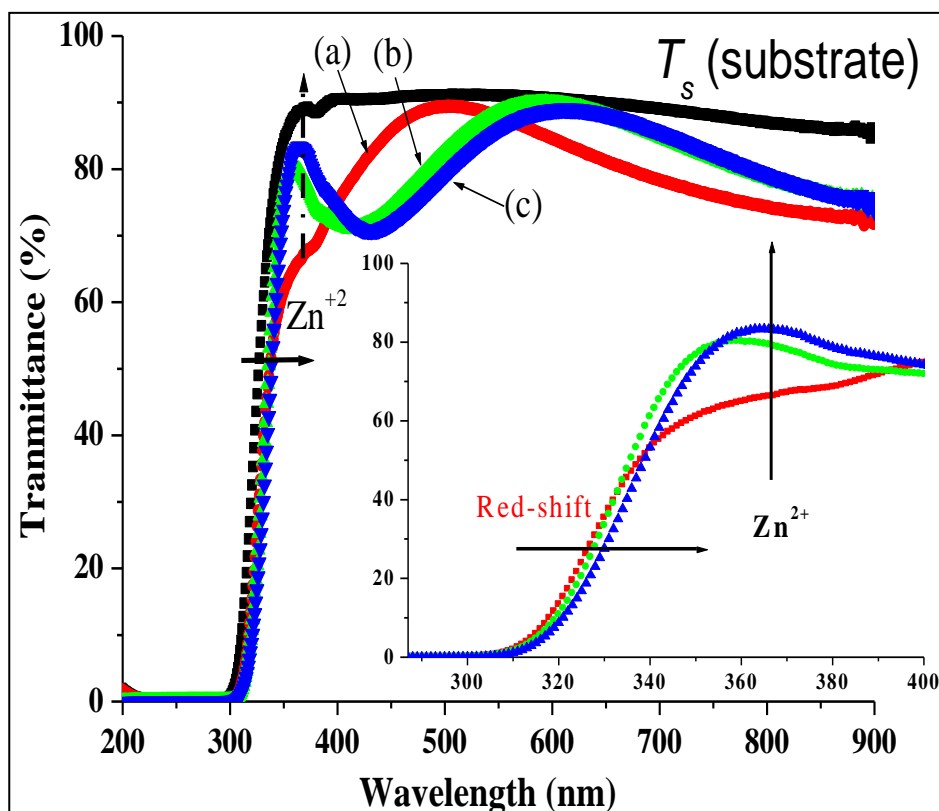


Figure.IV.3 Transmittance spectra of the Zn: TiO₂ films of (a) 0 wt% Zn: TiO₂, (b) 3 wt% Zn: TiO₂, and (c) 7 wt% Zn: TiO₂.

In terms of Swanepoel's method, which is based on the idea of *Manificier et al.* [131], using (III.9, III.10, III.11, and III.13) equations, we calculate the thickness.

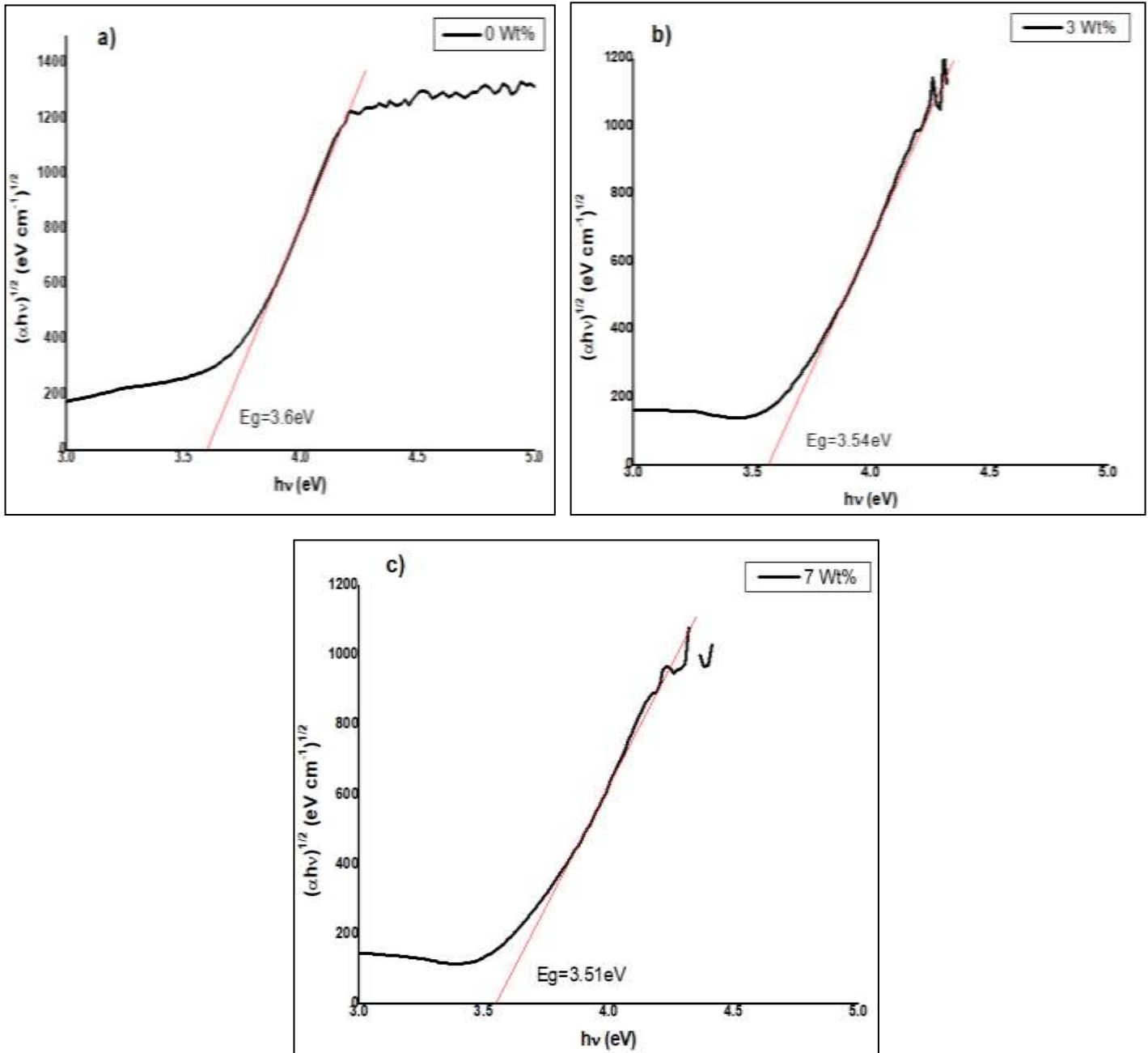


Figure.IV.4 Indirect band gap energy (Tauc's plot) estimations of Zn:TiO₂.

The calculated band gaps according to **Eq.III.15** from the intercept of the tangents of the graphs in the current work are 3.6, 3.54, and 3.51 eV for undoped, 3 and 7 wt% Zn-doped

TiO₂, respectively. (Figure IV.5) shows the variation in optical gap as a function of Zn doping level. The optical gap is clearly reduced as a result of the defect levels created by zinc doping, which also causes an absorption edge shift (i.e., red shift) in the transmittance of these films, as seen in Fig. IV.4. Prathvi *et al.* [132] observed the same conclusion in Zn-doped TiO₂ films created by spin coating, as did Arunachalam *et al.* [133] in Zn-doped TiO₂ thin films prepared by spray pyrolysis. However, Tang Bo-Wen *et al.* [127] reported that zinc doped at concentrations less than 3% has a blue shift of the absorption edge compared with the reference TiO₂, which reflects a slight increase in the optical gap, but the decreased trend in the band gap was generally more observed in the literature [123, 126, 132, 133,134].

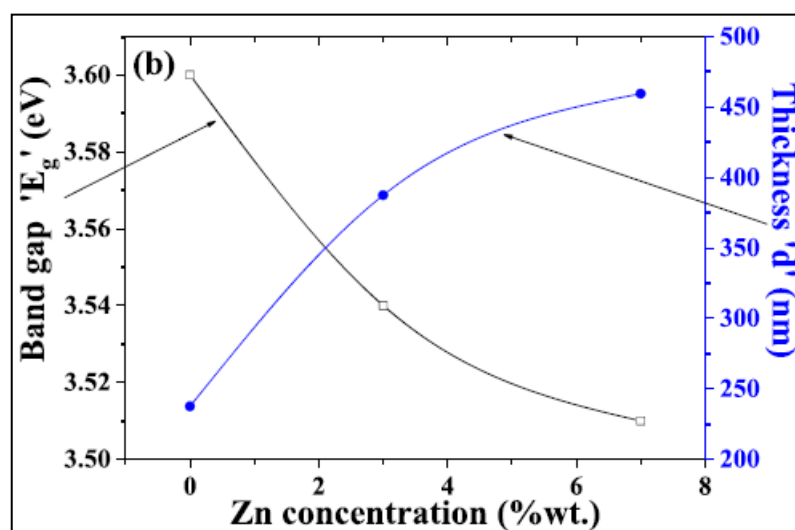


Figure.IV.5 Thickness and band gap.

In addition, the estimated indirect band gaps of the produced Zn: TiO₂ thin films are all larger than the value reported in the literature for bulk TiO₂. The undoped TiO₂ thin film has a 0.4 eV shift from the reported value of ~3.2 eV. This could be attributed to quantum size effects caused by the small size of Zn: TiO₂ nanocrystallite in thin film, which shifts the absorption edge to a shorter wavelength of radiation [133, 135]. Several writers [136, 137] have adapted the effective mass approximation (EMA) model of Brus [138] to study the link between band gap shift (ΔE_g) and radius (R) of quantum-sized particles.

$$\Delta E_g = \frac{h^2}{8R^2} \left[\frac{1}{m_e^*} + \frac{1}{m_h^*} \right] - \frac{1.8e^2}{\epsilon R} \dots\dots\dots (IV.1)$$

Where h is Plank's constant, m_e^* effective electron and m_h^* hole masses (1.20 m_e and 0.7 m_e , respectively), e is electron charge, and ϵ dielectric constant (1.84) of TiO₂ [139]. Therefore,

$$\Delta E_g = [1.35 \times 10^{-37}]x^2 - [2.5 \times 10^{-38}]x, \left(\frac{1}{x} = R, \Delta E_g \text{ in Joule and R in Meter} \right).$$

Table .IV.2 Thickness, band gap, shift in band gap and grain size calculated from transmittance spectra.

Zn (wt. %)	Thickness (nm)	bandgap (eV)	Shift in bandgap (eV)	Grain size from EMA (nm)
0	237.57	3.6	0.4	2.92
3	387.43	3.54	0.34	3.15
7	459.48	3.51	0.31	3.25

Table.IV.2 shows the predicted particle diameters of the Zn: TiO₂ thin films, which ranged between 2.92 and 3.25 nm. It was also observed that as thickness increased (**Fig. IV.5**) band gap energy decreased while particle size increased, whether calculated using the Scherrer equation or the **EMA** model, whereas SEM images revealed that the surface of the Zn: TiO₂ thin films was full of visible agglomerates with non-uniform grain clusters in number and size, when Zn doping increased up to 7 wt% (**Fig. IV.2**)

IV.1.4 M-lines analysis

The optical waveguide characteristics are investigated using m-lines spectroscopy. M-lines spectroscopy is a technique used to evaluate the optical waveguide parameters of a material or structure [140, 141]. In this technique, the measurements are performed using TE (transverse electric) and TM (transverse magnetic) linear polarizations of the incident laser beam, which are coupled into the waveguide films by a prism. The reflected intensity is measured for both TE and TM polarizations as a function of the incidence angle. For each polarization, the reflected intensity will exhibit distinct behavior as a function of the incidence angle due to the different waveguide modes supported by the structure. These modes can be characterised by their respective propagation constants and field distributions. The M-lines obtained through this measurement technique provide valuable information about the optical properties of the waveguide, such as the effective refractive index, waveguide thickness, and propagation losses.

The propagation constants of the guided modes are deduced from the positions of the synchronous angles, and then the refractive index n_{TE} and n_{TM} are determined by solving the dispersion equations.

The mode effective index N_{eff} can be calculated using the equation [142]:

$$N_{eff} = n_p \sin \left[A_p + \arcsin \left(\frac{\sin \theta_i}{n_p} \right) \right] \dots\dots\dots (IV.2)$$

With n_p (2.5822(TM), 2.8639 (TE)) is the refractive index of the prism, A_p (44.60°), is the prism angle and θ_i is the incident angle [114, 143],

Such as calculated N_{eff} of TiO_2 undoped

- For TE, $N_{eff} = 2.8639 \times \sin \left[44.60^\circ + \arcsin \left(\frac{\sin(-29.64^\circ)}{2.8639} \right) \right] = 1.6285$
- For TM, $N_{eff} = 2.5822 \times \sin \left[44.60^\circ + \arcsin \left(\frac{\sin(-22.95^\circ)}{2.5822} \right) \right] = 1.5146$

The values are summarised in the *Table.IV.3*

Table.IV.3 valuable for N_{eff} Zn: TiO₂ thin films.

Zn (wt %)	N_{eff} (TE)	N_{eff} (TM)
0	1.6285	1.5146
3	1.6293	1.5103
7	1.8305	1.7240

Figure.IV.6. (a-c) shows the registered TE and TM mode spectra. One guided mode ($m=0$) was aroused for each case.

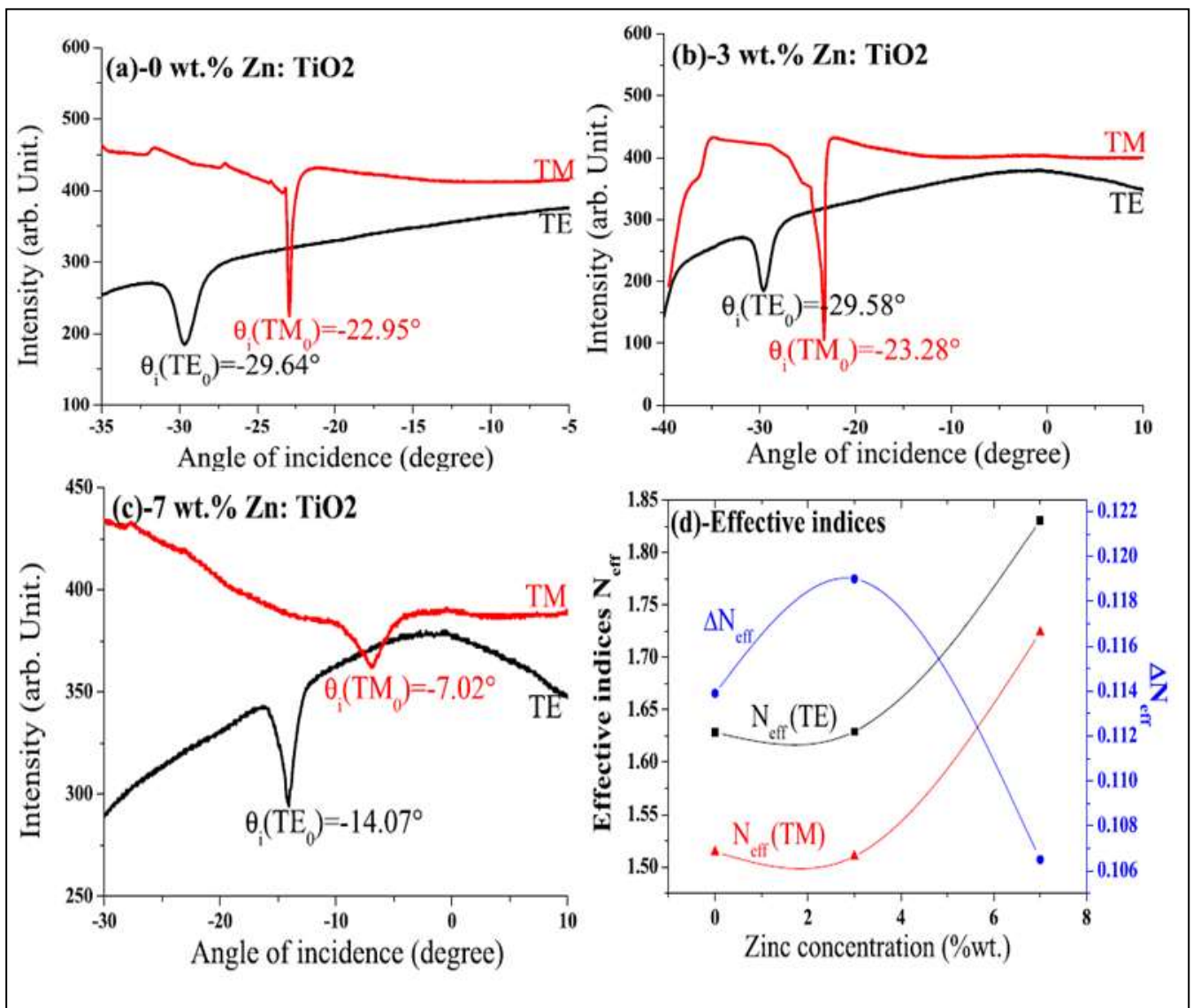


Figure.IV.6. TE and TM mode spectra of Zn: TiO₂ films (a) 0, (b) 3, (c) 7 wt% Zn; (d) effective indices vs. Zn concentration.

If the waveguides under investigation are mono-mode, meaning they support only a single guided mode, it can indeed be challenging to calculate the refractive indexes before knowing their thickness. In such cases, an estimation of the refractive index (n) can be made based on the assumption that the optical materials are isotropic. For isotropic materials, it is assumed that the refractive index is the same for both TE and TM polarizations, i.e., $n = n_{TE} = n_{TM}$. However, it's important to note that this assumption may not hold true for optical materials that are anisotropic, where the refractive index can vary with the propagation direction in the material.

The process of calculating the refractive index and thickness together is commonly employed to evaluate the accuracy of refractive index values obtained from experimental measurements. This approach involves multiple steps, we first used the thickness values calculated by the Swanepoel method and the refractive index measured ‘ N_{eff} ’, and finally, we used dispersion equation of the planar dielectric guide [140, 144]:

For TE polarization:

$$\frac{2\pi}{\lambda} d \sqrt{n^2 - N_{eff}^2} = \arctan\left(\sqrt{\frac{N_{eff}^2 - n_a^2}{n^2 - N_{eff}^2}}\right) + \arctan\left(\sqrt{\frac{N_{eff}^2 - n_s^2}{n^2 - N_{eff}^2}}\right) \dots\dots\dots (IV.3)$$

For TM polarization:

$$\frac{2\pi}{\lambda} d \sqrt{n^2 - N_{eff}^2} = \arctan\left(\frac{n^2}{n_a^2} \sqrt{\frac{N_{eff}^2 - n_a^2}{n^2 - N_{eff}^2}}\right) + \frac{n_c^2}{n_s^2} \arctan\left(\sqrt{\frac{N_{eff}^2 - n^2}{n^2 - N_{eff}^2}}\right) \dots\dots\dots (IV.4)$$

Where n , $n_a = 1$, and $n_s = 1.44$ are the film, air, and substrate refractive indexes, respectively, d is the thickness of the film, and $\lambda = 632.8$ nm is the wavelength of the He-Ne laser beam utilised. Furthermore, the refractive index values are invariably lower than those of bulk anatase TiO₂ ($n_b = 2.54$), possibly due to either the size of the nanoparticles or their porosity [145, 146]. Thus, since $n_s(1.44) < n_f < n_b(2.54)$

By plotting the curves (IV.3) and (IV.4), we can therefore determine the refractive indices in each type of polarization,

Figure.IV.6 shows the variation in refractive indices and birefringence as a function of zinc content. The refractive indices for TiO₂, having a tetragonal structure, exhibit different values

for TE polarization (n_{TE}), and TM polarization (n_{TM}). These findings are in line with previous studies referenced in the literature [147, 148].

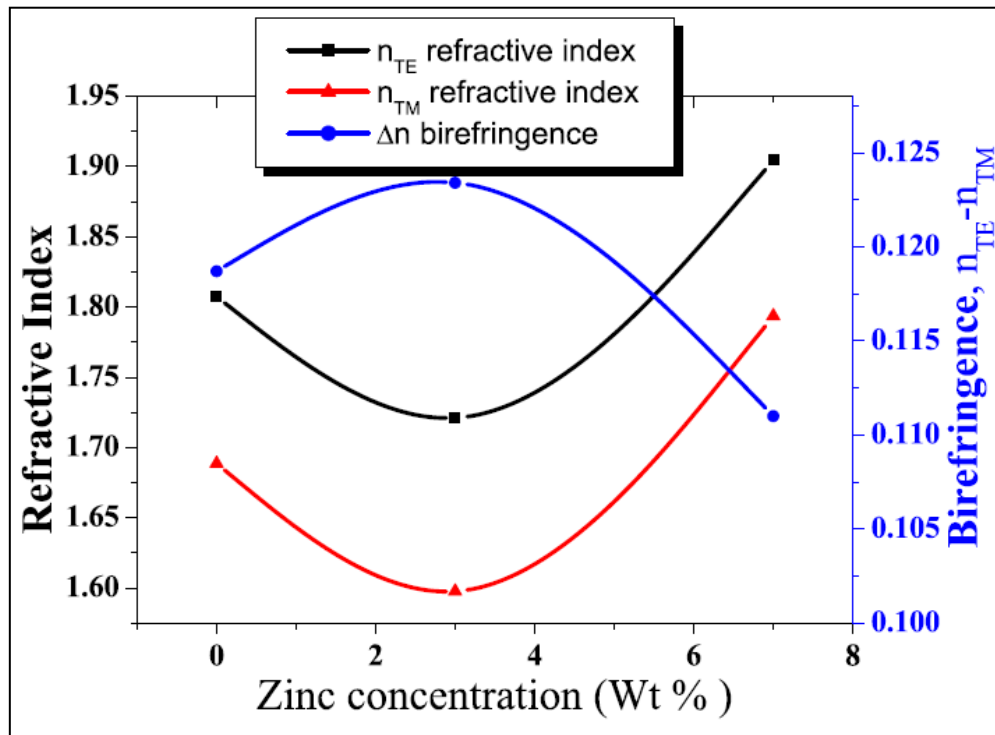


Figure.IV.7 n_{TE} and n_{TM} refractive indexes and birefringence of Zn: TiO₂ thin films.

The results shown in **Figure.IV.7** clearly demonstrate that increasing the zinc concentration (wt %) leads to an increase in the refractive index for both TE and TM polarizations. This indicates that the doping of zinc improves the waveguiding properties of the material. This increase in refractive index can be attributed to a decrease in the band gap. The band gap values measured for undoped TiO₂, 3 wt% Zn:TiO₂, and 7 wt% Zn: TiO₂ are 3.6 eV, 3.54 eV, and 3.51 eV, respectively. The refractive index is an important optical property for materials used in optical devices. Therefore, it is necessary to estimate the refractive index using a key parameter in semiconductors, which is the band gap energy (E_g). Many models have been proposed in the literature to describe the inverse relationship between the refractive index and the band gap.

In **table.IV.3**, the models proposed by *Hervé and Vandamme* [149] are presented.

$$n^2 = 1 + \left(\frac{13.6}{E_g + 3.4} \right)^2 \dots\dots\dots (IV.5)$$

Moss. [150]

$$n \equiv \left(\frac{95}{E_g} \right)^{1/4} \dots\dots\dots (IV.6)$$

Reddy and Ahammed. [151]

$$n = \left(\frac{154}{E_g - 0.365} \right)^{1/4} \dots\dots\dots (IV.7)$$

Ravindra et al. [152] have presented a linear relationship between E_g and n . This empirical relation is given by:

$$n \equiv 4.084 - 0.62E_g \dots\dots\dots (IV.8)$$

Table.IV.4. Comparison of the calculated values of refractive index from various models.

Zn (wt.%)	Band gap (eV)	Refractive index					
		Eq (IV.5)	Eq(IV.6)	Eq(IV.7)	Eq(IV.8)	n_{TE}	n_{TM}
0	3.6	2.18	2.26	2.62	1.85	1.8073	1.6886
3	3.54	2.20	2.27	2.63	1.88	1.7211	1.5977
7	3.51	2.21	2.28	2.64	1.90	1.9046	1.7936

Table IV.4 clearly indicates that a decrease in band gap energy results in an increase in refractive index. As a result of these computations, we can establish that the proposed models' behaviour between E_g and n is correct [153]. Despite their general consistency in behaviour between them, sometimes this behaviour is not necessarily always correct, according to the results obtained utilizing the m-lines spectroscopic observations of *Hanini et al.* [154] in Al-doped TiO_2 prepared by PLD and *Khodja et al.* [155]. In ZnO prepared by sol-gel, they discovered a clear increase in these two parameters, which could be the result of a decrease in the surface roughness (root mean square roughness, RMS) of the thin films whose values were already recorded in their research, and thus a relative increase in the refractive index despite an increase in the band gap. As a result, it is desirable to use experimental techniques that enable the characterisation of thin film optical characteristics. For example, we employed transmission and reflection coefficient measurements [156], spectroscopic ellipsometry [157],

In addition, we used m-lines spectroscopy to accurately describe characterize our thin films [140, 158, 159]. Furthermore, **Table IV.3** clearly shows that the values extracted from **Eq. IV.8** are almost the same as those extracted from the MLS measurements. It is likely that this is due to the fact that these films developed by the sol-gel process are porous and therefore have slightly lower refractive indexes compared to other methods such as PLD, sputtering, and MBE, whose refractive index may align with previous models.

The comparison results shown in **Table 3** are just an illustration of the significance of this experimental result acquired using MLS. It should be noted that our major conclusions for the refractive indices (n_{TE} and n_{TM}) are based solely on MLS measurements at 632.8 nm wavelength, although all thin film planar waveguides indicated a well-guided single mode for both TE and TM. Such a comparison can aid in the future understanding and development of these numerous proposed models, in addition to the band gap, which is the primary reason for the optical properties on which the various proposed models are built. It must be understood that the microstructure of the material is taken into account when reformulating it, because the optical properties also depend strongly on: particle shapes, surface roughness, porosity, grain size, and grain boundaries [160].

Furthermore, as the zinc concentration increased up to 7wt%, the birefringence of the films, as shown in **figure.IV.6**, was reduced. This means that the refractive indexes n_{TE} and n_{TM} became closer to each other. This change suggests two things: firstly, it indicates a decrease in the crystallinity or significant alterations in the microstructure of the TiO_2 films [147]. Secondly, it reflects the approach to the truth of isotropic optical properties in amorphous materials, which aligns with the XRD and SEM results of the Zn: TiO_2 thin films [161].

IV.2. Synthesis metallic oxides and pair of oxides based on TiO₂ thin films

This study utilized the sol-gel method of spin-coating to synthesis metallic oxides and pair of oxides based on TiO₂ thin films. The research aimed to investigate the effects of these films on their structural, optical, and topological properties. Thin films were characterized using Raman, ultraviolet–visible spectroscopy, and atomic force microscopy, respectively.

IV.2.1. Raman Analysis

Figure IV.8 shows the Raman spectra of TiO₂ thin film prepared on glass and silicon substrates, ZnO and CuO thin films, and ZnO/TiO₂ and CuO/TiO₂/ bilayer thin films on glass substrates. With excitation at 532 nm, we observe several peaks explains in **table IV.5**

Table. IV.5 Modes vibration of TiO₂, ZnO, and CuO.

A-TiO ₂		R-TiO ₂		ZnO	CuO
Mode Wavenumber (cm ⁻¹)		Mode	Wavenumber (cm ⁻¹)	Mode	Mode
E _g	144	B _{1g}	143	E ₂ (low)	2B _g
E _g	197	E _g	447	E ₂ (high)- E ₂ (low)	A _g
B _{1g}	399	A _{1g}	612	A ₁ (TO)	B _g
A _{1g}	513	E _g	826	E ₁ (TO)	
B _{1g}	519	-	-	E ₂ (high)	
E _g	639	-	-	2xLA A ₁ (LO) E ₁ (LO)	

The Raman spectrum of a single crystal of anatase TiO₂. Showing six characteristic modes allowed at 144, 197, 399, 513, 519, and 639 cm⁻¹, characterizing the absorption of anatase TiO₂ [143]. The ZnO it is well known that he Brillouin zone, in which the A₁+ E₁+ 2E₂ modes show Raman activity. Moreover, the A₁ and E₁ modes split into longitudinal (LO) and

transverse (TO) optical components with different frequencies due to the macroscopic electric fields of the LO phonons. Copper (II) oxide (CuO) falls into the C_{2h}^6 space group with two molecules in each primitive cell. It exhibits nine zone-center optical phonon modes, characterized by symmetries $4A_u + 5B_u + A_g + 2B_g$. Among these, only three $A_g + 2B_g$ modes are Raman active [162], as explained in **table.IV.5**.

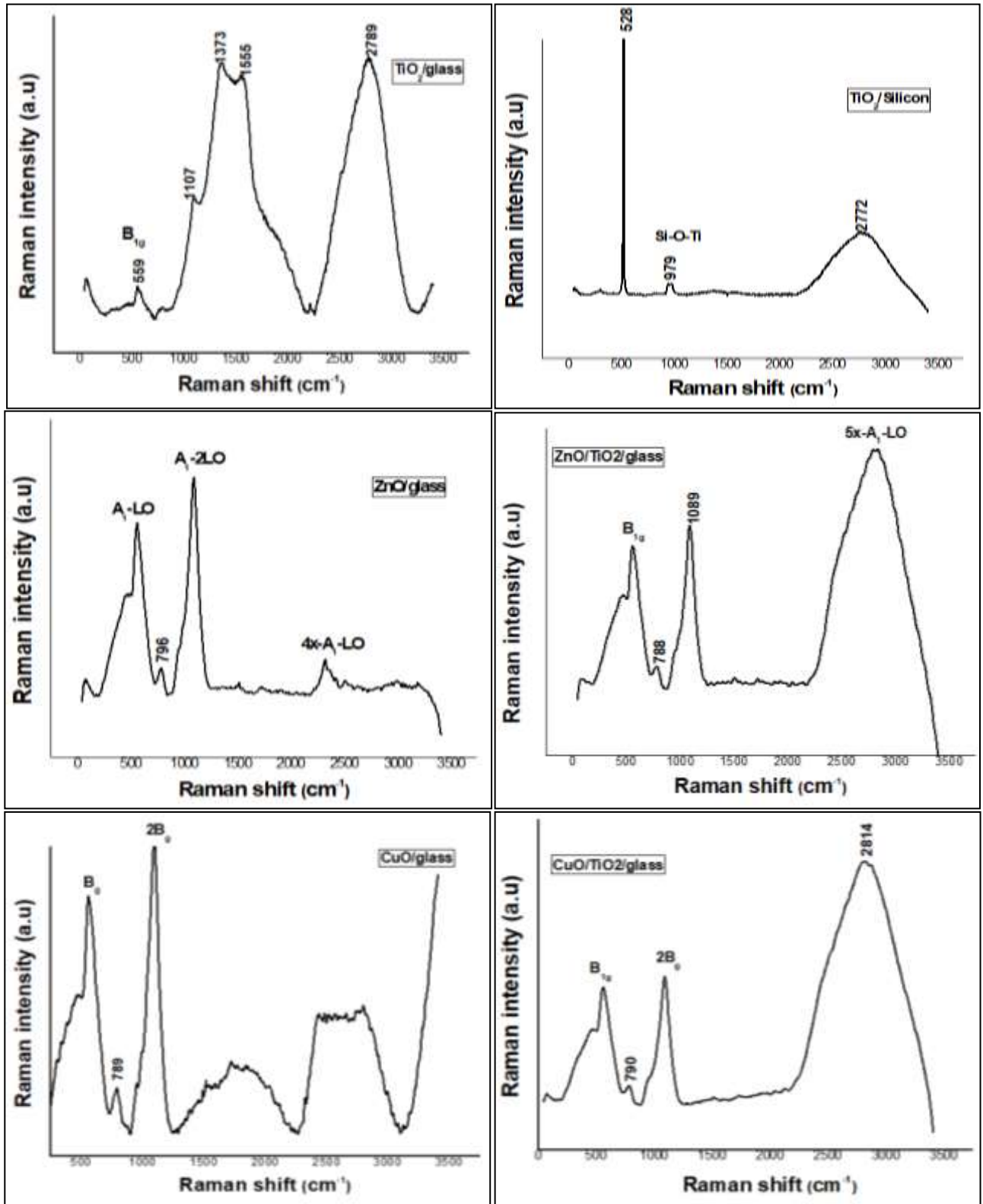


Figure.IV.8 Results of the Raman spectroscopy analyses for the synthesized thin films.

Table.IV.6 Positions and FWHM of Raman peaks for as prepared for monolayers and bilayers based on TiO₂ thin films.

	Wavenumber(cm ⁻¹)	FWHM (cm ⁻¹)	Phase
TiO₂/glass	559.07	65.3	A-TiO ₂ - B _{1g}
	1107.67	33	A-TiO ₂
	1373.41	52.41	A-TiO ₂
	1555.37	65	A-TiO ₂
	2789.74	506.98	A-TiO ₂
TiO₂/ silicon	528.46	6	A-TiO ₂
	979.59	41	A-TiO ₂
	2772.019	429	A-TiO ₂
ZnO/glass	560.31	51.56	ZnO- A ₁ -LO
	796.72	51.56	-
	1101.23	110	ZnO- A ₁ -2LO
	2314.44	19.77	ZnO- 4x A ₁ -LO
ZnO/TiO₂/glass	554.29	58.43	A-TiO ₂ -B _{1g}
	788.02	45.54	-
	1089.15	116.86	-
	2820.35	630.72	ZnO- 5x-A ₁ -LO
CuO/glass	564.71	84.21	CuO- B _g
	789	46.2	-
	1093.93	103.97	CuO- 2B _g
	2817	707	-
CuO/TiO₂/ /glass	559.07	60	A-TiO ₂ -B _{1g}
	790.27	38.67	-
	1095.59	130.61	CuO- 2B _g
	2814	657.36	-

The band observed for TiO₂ on silicon substrates at 528 cm⁻¹ has a stronger intensity and narrower line-width, which is characteristic of the vibration modes of the silicon substrate. A broad band centred at 979 cm⁻¹ is observed, and it is attributed to the formation of a silicon-oxygen-titanium complex, Si-O-Ti [163], indicating a strong interaction between the titanium oxide film and the silicon substrate. Thin films of ZnO with a hexagonal wurtzite structure and good crystal quality exhibit a peak at approximately 1101 cm⁻¹ has a stronger intensity and narrower line-width, corresponding to a 2LO phonon mode process. Similar to **Zhuo, R, et al.**'s findings, excitation by laser lines at 325 nm indicates dominance by the 1LO and multi-LO modes [164, 165]. The bands observed in CuO thin films at 564 cm⁻¹ and 1093 cm⁻¹ correspond to B_g and 2B_g, respectively [166]. The intensity of the bands increases notably when comparing the ZnO/TiO₂ and CuO/TiO₂ bilayer thin films (554, 794, 560 cm⁻¹, and 790 cm⁻¹) to those of ZnO and CuO monolayer thin films respectively. Additionally, in this case, the intensity of the main band is significantly elevated at 2820.35 cm⁻¹ and 2814 cm⁻¹.

IV.2.2. FTIR analysis

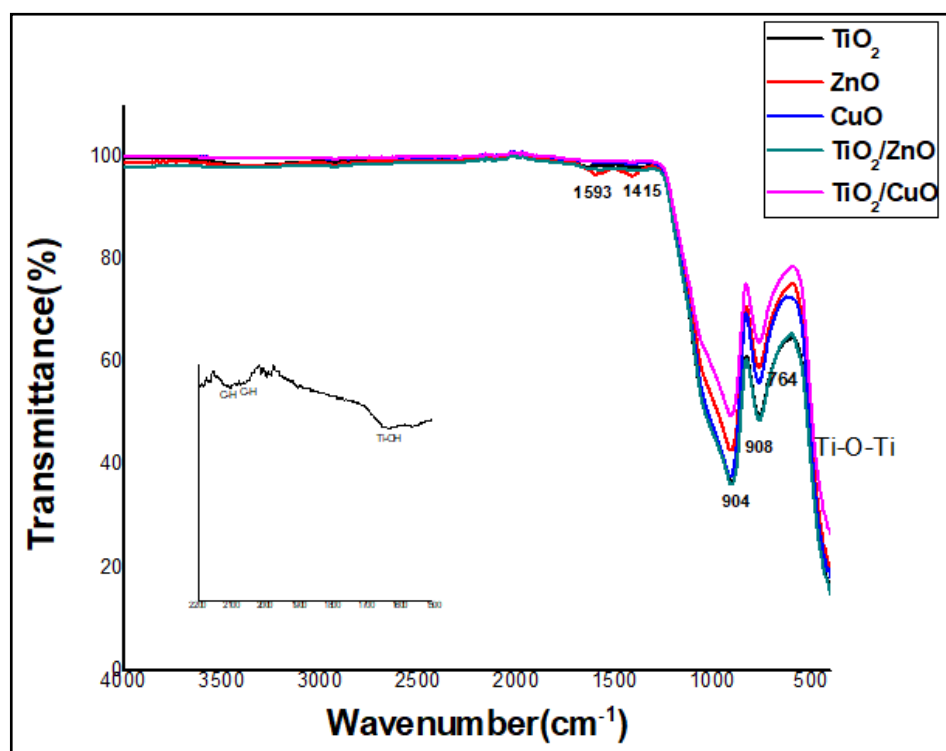


Figure.IV.9. FTIR measurement patterns for monolayers and bilayers based on TiO₂ thin films.

FTIR is an effective method to analyze the composition of compounds or products. The FTIR spectra of the films were obtained using a Fourier transmission infrared spectrometer (Nicolet Avatar 360) in the range of 400-4000 cm^{-1} . **Figure.IV.9** shows the FTIR spectrum of TiO_2 , ZnO, CuO, ZnO/ TiO_2 , and CuO/ TiO_2 thin films. The main bands were observed at the following positions of TiO_2 : $\sim 750, 902, 1632, 2105 \text{ cm}^{-1}$. The band at 1632 cm^{-1} is associated with the rotation of H_2O and Ti-OH bonds. The localized band at 2105 cm^{-1} corresponds to the C-H bond of organic compounds. The peaks in transmittance occurring within the range of 450 to 600 cm^{-1} were attributed to the Ti-O-Ti bonding. These results well agree with earlier [143]. For the ZnO thin film, it is inferred that the samples have absorption peaks in the range of $764 \text{ cm}^{-1}, 908 \text{ cm}^{-1}, 1415 \text{ cm}^{-1}, 1593 \text{ cm}^{-1},$ and 2917.29 cm^{-1} . The peak at 1593 cm^{-1} corresponds to the vibration modes of aromatic nitro compounds and alkyl, and the peak at 2917.29 cm^{-1} is ascribed to the stretching vibration of hydroxyl compounds [167], The additional peaks at 764 cm^{-1} and 908 cm^{-1} indicate the presence of ZnO and organic groups, which could be due to the presence of zinc-hydroxyl-acetates [168]. Also characteristic peaks can indicate the presence of Ti-O and Zn-O bonds. In thin film copper oxide, the bands are at $744 \text{ cm}^{-1}, 904 \text{ cm}^{-1}, 1640 \text{ cm}^{-1}, 2089 \text{ cm}^{-1}, 2852 \text{ cm}^{-1},$ and 3409 cm^{-1} . The presence of the peak at 1639 cm^{-1} indicates the stretching vibration of the Cu-O bond in copper (II) oxide. The appearance of the peak at 3409 cm^{-1} is associated with OH stretching present as a result of the hydroxyl group on the surface of the CuO [169, 170]. A similar behavior for both diagrams is observed ZnO and ZnO/ TiO_2 thin films, as well as CuO and CuO/ TiO_2 thin films.

Table. IV.7 Modes of TiO_2 , ZnO, and CuO.

Thin films	Wavenumber (cm^{-1})	Mode
TiO₂	1632	H ₂ O and Ti-OH
TiO₂	2105	C-H
TiO₂	450-600	Ti-O-Ti
ZnO	1593	Aromatic nitro compound
ZnO	2917.29	Hydroxyl compound
ZnO	764 and 908	Zinc-hydroxyl-acetates
CuO	1639	Cu-O
CuO	3409	OH

IV.2.3. AFM analysis

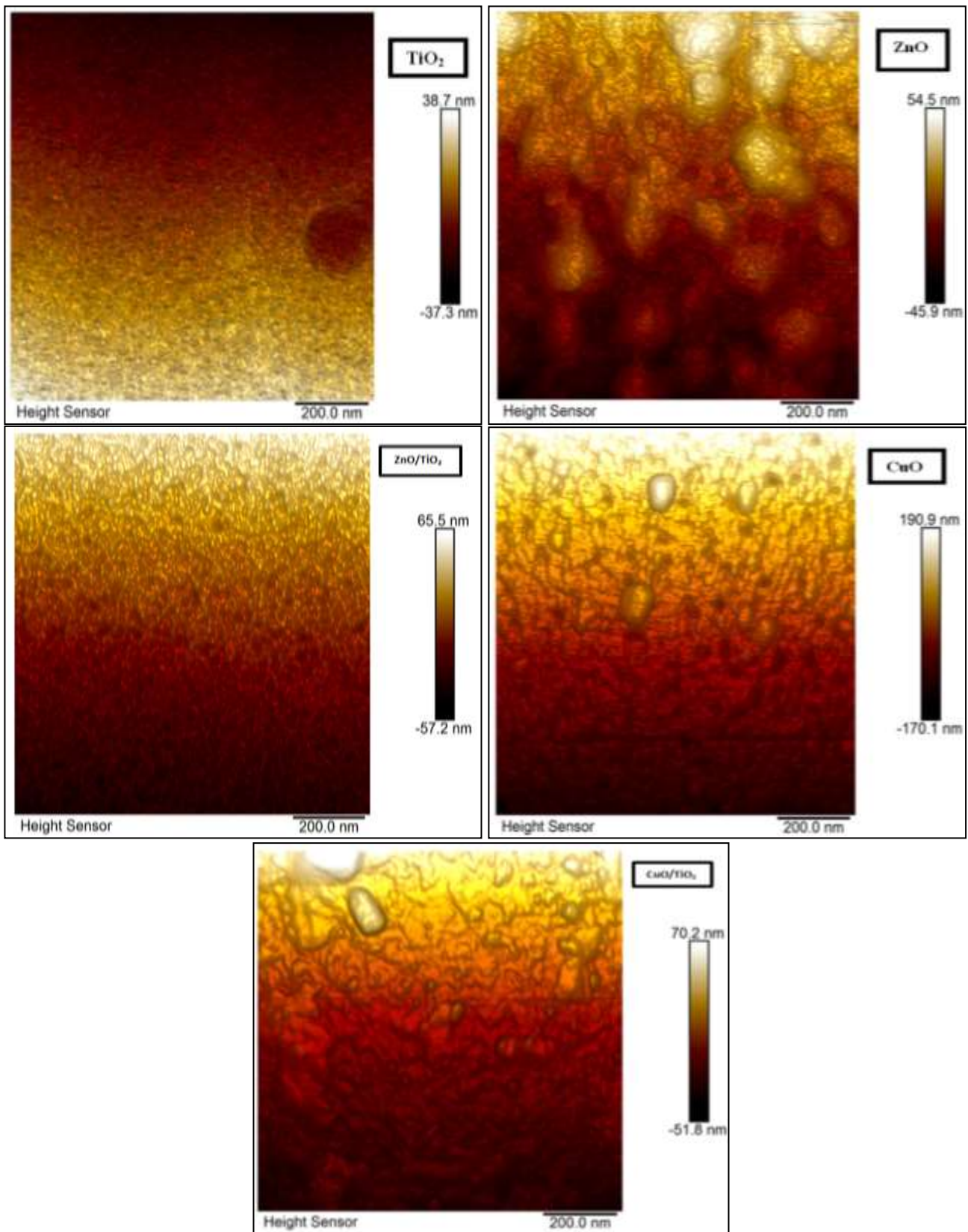


Figure.IV.10 The AFM results surface images of 2D for monolayers and bilayers based on TiO_2 thin films.

The topological surface properties were characterized using AFM by scanning an area of $1 \times 1 \mu\text{m}$ for analysis. **Figure IV.10** displays AFM images of thin films of TiO_2 , ZnO , and CuO . There are also thin film bilayers of ZnO/TiO_2 and CuO/TiO_2 . **Table.IV.7** tabulates the obtained roughness parameters. The surface roughness, as measured by the average roughness value (R_a), provides an indication of the deviation of a surface from its ideal form. TiO_2 demonstrated the lowest average roughness among the materials mentioned, with a R_a value of 1.70 nm. This suggests a relatively smooth surface compared to the other materials. CuO exhibited the highest average roughness, with a R_a value of 5.92 nm. The rough surface of CuO increases the surface area. This indicates that the CuO surface is relatively rough, with significant deviations from its ideal form. ZnO showed a comparable average roughness with a R_a value of 4.83 nm. While slightly lower than CuO , it still suggests a relatively rough surface. Thin film bilayers of CuO/TiO_2 displayed an average roughness of 3.97 nm. This value indicates a lower roughness compared to both CuO . Thin film bilayers of ZnO/TiO_2 exhibited a further decrease in average roughness, with a R_a value of 2.24 nm. This indicates a smoother surface compared to the previous thin films. The Root mean square roughness **RMS** and maximum roughness (R_{max}) for CuO were observed to be ~ 7.56 nm and ~ 82.2 nm respectively.

Table.IV.8 Roughness parameters.

Thin films	Roughness average (R_a)	Root mean square roughness (R_q)	Maximum roughness (R_{max})
TiO_2	1.70 nm	2.27 nm	23.8 nm
ZnO	4.83 nm	6.07 nm	35.7nm
ZnO/TiO_2	2.24 nm	2.78 nm	19.8 nm
CuO	5.92 nm	7.56 nm	82.2 nm
CuO/TiO_2	3.97 nm	5.26 nm	39.3 nm

IV.2.3. Optical analysis

The optical transmittance for monolayers and bilayers based on TiO₂ thin films has been plotted versus wavelength in the range of 250–900 nm (**Figure IV.11**).

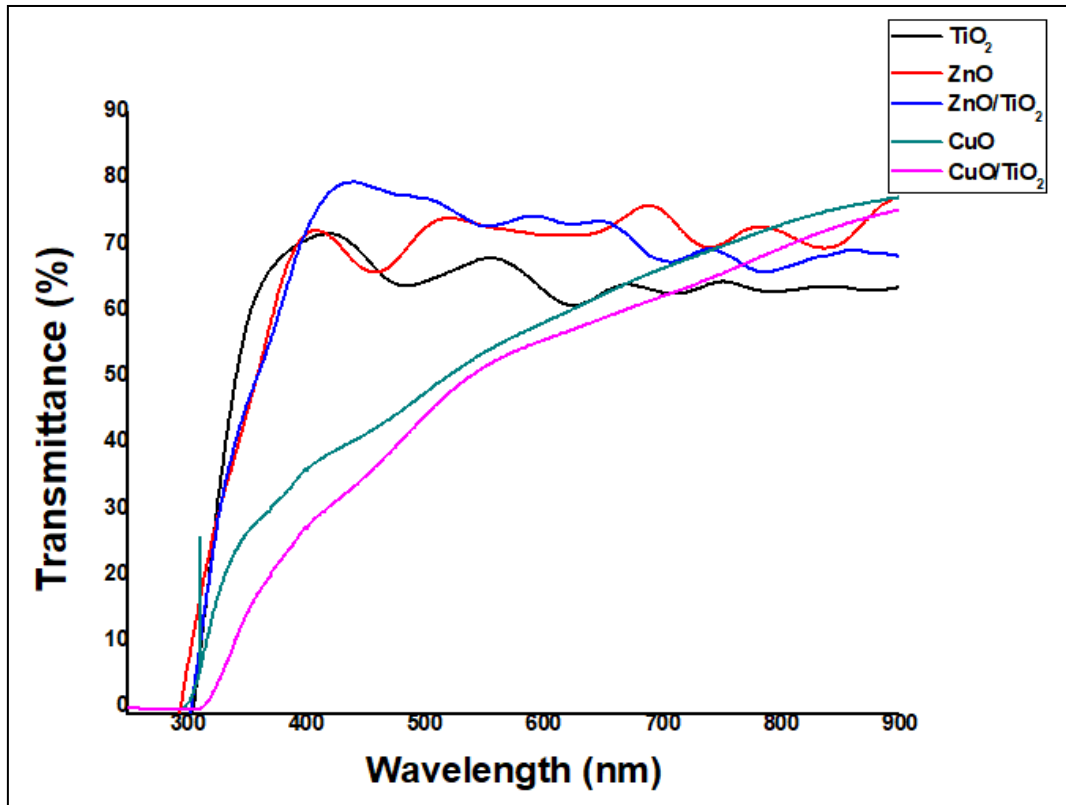


Figure IV.11. The transmittance spectra for monolayers and bilayers based on TiO₂ thin films.

It is observed that TiO₂, ZnO, and ZnO/TiO₂ thin films exhibit high transmittance, ranging from 60 to 80%. On the other hand, CuO and CuO/TiO₂ thin films show low transmittance. The ZnO/TiO₂ bilayer thin film demonstrates the highest transmittance spectrum, reaching 75%. A similar value was observed by *Arifin et al.* [8]. This represents a notable improvement compared to the transmittance levels of TiO₂ and ZnO monolayer thin films, which have a difference of approximately 10% in the transmittance spectrum, attributed to the highly transparent nature of the high-quality structural and surface morphology of the thin film. Thus, this sample allows more incident light to penetrate because it requires a significant number of photons to reach the interface in a heterojunction thin film. Also, the increase in the transmittance value after the creation of ZnO/TiO₂ bilayer thin films indicates an

improvement in the crystallinity of the films, which is also confirmed by AFM measurements. Furthermore, a sharp absorption edge is observed in the wavelength range of 255–310 nm. This suggests that the thin films have significant absorption at these wavelengths. This combination enhances the overall performance of the thin film for various applications. The ZnO/TiO₂ bilayer structure in solar cells can function as an electron transport layer or as a component of the photoactive layer [8]. CuO/TiO₂ bilayer thin films have been studied for photocatalytic [9]. The band gap energy can be measured by the extrapolation technique using the *Tauc* plot (**figure.IV.12.**). The calculated E_g is shown in **table.IV.8**, where the values are similar [8, 171]. The examination of transmittance spectra and derived optical band gaps supports the notion that the ZnO/TiO₂ layer shows promise as a mesoporous ETL (electron transport layer). Its notable transparency and well-suited band gap align well with the energy requirements of perovskite solar cells, indicating its potential effectiveness [172]. We determined the refractive index (**table.IV.8**) values using **Equation IV.8**, which we used in the first part because the values were equivalent to MLS.

Table.IV.9. band gap and refractive index for monolayers and bilayers based on TiO₂ thin films.

Film	TiO₂	ZnO	ZnO/TiO₂ direct	ZnO/TiO₂ indirect	CuO	CuO/TiO₂ direct	CuO/TiO₂ indirect
Band gap	3.69	3.12	3.98	3.73	4.05	3.78	3.33
Refractive index	1.7962	2.1496	1.6164	1.7714	1.573	1.7404	2.0194

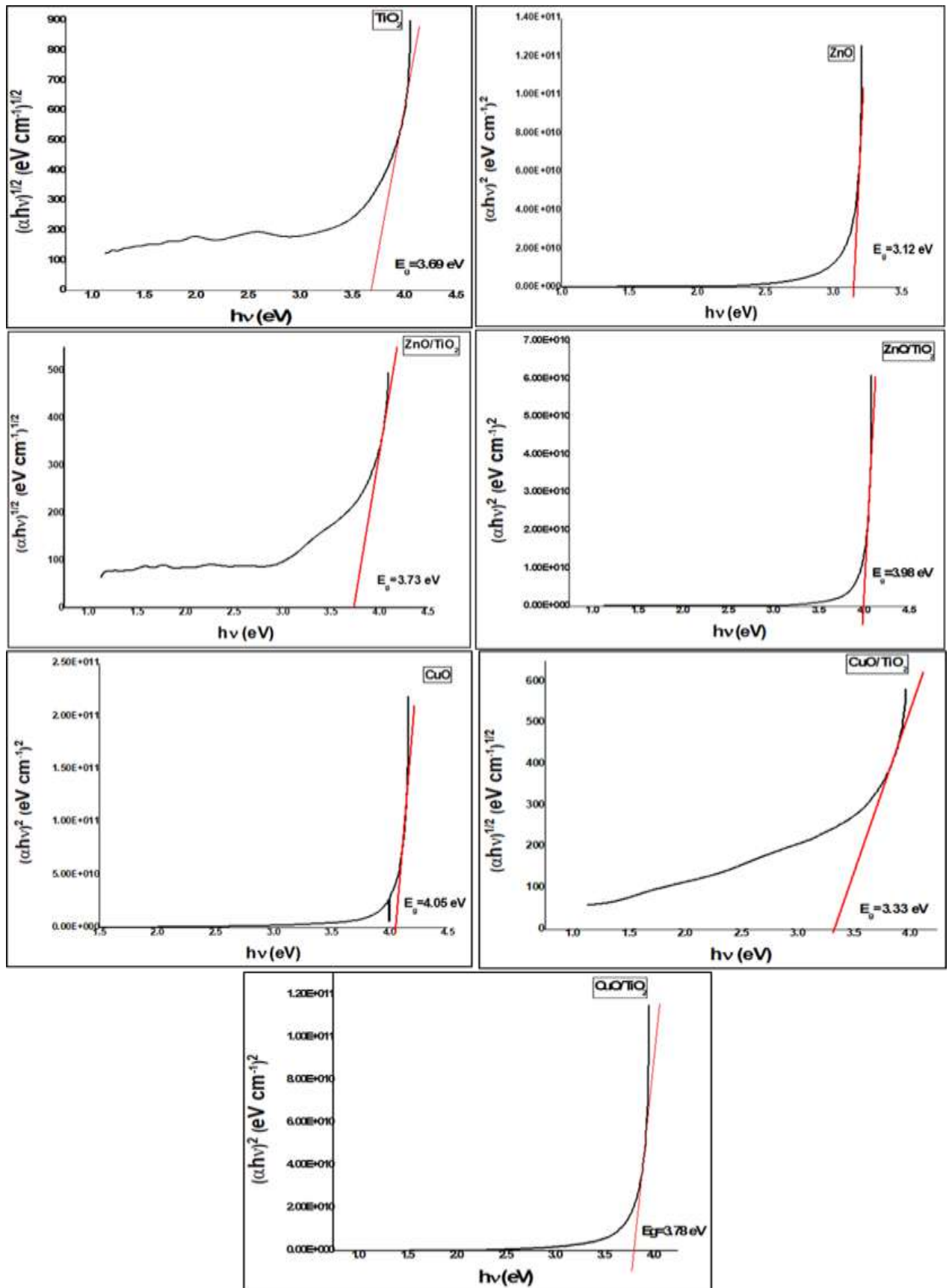


Figure .IV.12. The band gap energy for monolayers and bilayers based on TiO₂ thin films is estimated from the tauc plot.

Conclusion

This study that we have undertaken as part of this thesis has as its main objective the optimization of the parameters inherent to the sol-gel method of the synthesis, on the one hand of Zn doped nanocrystallite TiO₂ films waveguide properties and on the other hand to study metallic oxides and pair of oxides based on TiO₂ thin films. The spin-coating technique was adopted for the production of all films. For the characterization of the developed layers, we report the structural, microstructural, topological, and optical properties of the film. We used a panel of experimental investigation methods: X-ray diffraction (XRD), scanning electron microscopy (SEM), atomic force microscopy (AFM), optical transmission spectrophotometry (UV-Vis), Raman spectroscopy, m-lines, and Fourier transform infrared spectroscopy (FTIR).

The results were as follows:

- I. For Zn doped TiO₂ thin films were deposited on glass substrates
 - ✓ The XRD analysis revealed that the TiO₂ is composed of anatase and Brookite phases with a preferential orientation following the direction (101) for anatase. The addition of zinc concentrations up to 7 wt% significantly reduced the crystallinity ratio to amorphous. The increase in Zn has the effect of increasing grain size from 5.23 to 16.56 nm for undoped and 3 wt% Zn doped TiO₂ thin films.
 - ✓ SEM images demonstrate that zinc additions can cause significant microstructure changes in titanium dioxide films, leading to distorted shapes and significantly larger sizes.
 - ✓ The UV-Vis analysis reveals that all TiO₂ thin films are transparent and have an average transmittance of more than 80% in the visible region. The band gap of TiO₂ thin films deposited on glass are 3.6, 3.54, and 3.51 eV for undoped, 3 and 7 wt% Zn doped TiO₂, respectively. It is clear that the optical gap is reduced due to the defect levels introduced by zinc doping, and this also induces an absorption edge shift (red shift) in the transmittance of these films.
 - ✓ The MLS characterization demonstrated that all thin film planar waveguides exhibit single well-guided mode propagation for both TE and TM polarizations. Furthermore, the refractive index (n_{TE} and n_{TM}) of Zn: TiO₂ thin films increases, suggesting that the Zn

doping improves the waveguiding properties. With concentrations up to 7 wt%, the birefringence decreases.

II. For metallic oxides and pair of oxides based on TiO₂ thin films

- ✓ According to Raman spectroscopic studies, the structural properties of monolayers and bilayers based on TiO₂ thin film compounds have been reviewed with to the results of Raman spectroscopic studies. These results suggest that the A₁ phonon mode and the B_{1g} phonon mode can be used to analyse the ZnO/TiO₂ thin film.
- ✓ The AFM morphological observation measures the surface roughness of monolayers and bilayers based on TiO₂ thin films using the root mean square roughness (RMS), with values ranging from 2.27 to 7.56 nm.
- ✓ The optical observations indicate that thin films of TiO₂, ZnO, and ZnO/TiO₂ have a high transmittance range of 60 to 80%. However, the CuO and CuO/TiO₂ thin films recorded low transmittance.
- ✓ The refractive index was estimated to be 1.79 and 2.01 for TiO₂ and CuO/TiO₂ thin films, respectively.

Ultimately, there were two crucial aspects that needed to be elaborated upon in the context of this study: (i) The results demonstrated that it was possible to modify TiO₂ films by incorporating doping or coupling of metal oxides based on TiO₂ thin films.; (ii) The future prospects include the utilisation of these metallic oxides and pair of oxides based on TiO₂ thin films for photocatalytic applications.

References

- [1] A.Omar, M.S.Ali, N.A.Rahim. Sol Energy 207:1088–1121. **2020**.
- [2] L.Khoroshko, V.Borisenko, P.Baltrukovich, S. Nurmonov, O.R. muradov. J Sol-Gel Sci Technol. **2022**.
- [3] B.C. Sertel, N.A. Sonmez. M.D. Kaya, S. Ozcelik. Ceram Int 45(3):2917–2921.**2019**.
- [4] V. Etacheri, C.D. Valentin, J. Schneider, D. Bahnemann, S.C. Pillai. Advances in theory and experiments. J Photochem Photobiol C: Photochem Rev 25:1–29.**2015**.
- [5] N. Serpone. The Journal of Physical Chemistry B, 110(48), 24287-24293.**2006**.
- [6] A.A. Galil, H. Ali, A.Atta, M. Balboul. J Radiat Res Appl Sci 7(1):36–43.**2014**.
- [7] P. Ezati, Z.Riahi, J.W.Rhim. . Food Hydrocoll 122:107104.**2022**.
- [8] N.M.Arifin, E.E.M.Noor, F.Mohamad, N.Mohamad. Coatings, 14(1), 73.**2024**.
- [9] C.K.N.Peh, X.Q.Wang, G.W.Ho. Procedia engineering, 215, 171-179.**2017**.
- [10] M.Ghoughali. Doctoral dissertation, University of Mohamed Khider, BISKRA.**2019**.
- [11] M.Balaish, R.Gonzalez, K.J.Kim, Y.Zhu, Z.D.Hood, J.L.Rupp. Nature Energy, 6(3), 227-239.**2021**.
- [12] I.Martinko. Doctoral dissertation, Université Paul Sabatier-Toulouse III.**2018**.
- [13] H.Adachi, K.Wasa. Nano-Materials and MEMS., 3-39.**2012**.
- [14] T.J.Kunene, L.K.Tartibu, K.Ukoba, T.C.Jen. Materials today: proceedings, 62, S95-S109.**2022**.
- [15] K.M.Thom. the University of Texas at Austin.**2009**.
- [16] A.Crisbasan. Doctoral dissertation, Université Bourgogne Franche-Comté.**2017**.
- [17] J.A.Venables, G.D.T.Spiller, M.Hanbucken, Reports on progress in physics, 47(4), 399.**1984**.
- [18] L.Makkonen. Journal of Physics: Condensed Matter, 28(13), 135001.**2016**.
- [19] J.Venables. Cambridge university press.**2000**.
- [20] Metal oxides book
- [21] C.Subramanian, A.K.Strafford. Wear, 165(1), 85-95.**1993**.
- [22] V. Monnier. Doctoral dissertation, Université Joseph-Fourier-Grenoble I.**2006**.

- [23] C.J.Brinker, G.W.Scherer. Sol-Gel Science, 3, 115-119.**1990**.
- [24] L.Znaid. Materials Science and Engineering: B, 174(1-3), 18-30.**2010**.
- [25] D.Wang, G.P.Bierwagen. Progress in organic coatings, 64(4), 327-338.**2009**.
- [26] B.G.Camacho. **2006**.
- [27] R.Sato, T.Kawai, K.Kifune. Journal of non-crystalline solids, 356(25-27), 1300-1304.**2010**.
- [28] A.Dehghanhadikolaei, J.Ansary, R.Ghoreishi. (2018).. *Proc. Nat. Res. Soc*, 2(1), 02008-02029.**2018**.
- [29] K.T.Chaudhary. In Thin Films. IntechOpen.**2021**.
- [30] E.Y.Muslih, B.Munir. Emerging Solar Energy Materials, 45-57.**2018**.
- [31] W.J.Daughton, F.L.Givens. Journal of the Electrochemical Society, 129(1), 173.**1982**.
- [32] E.Rahmani. IntechOpen.**2023**.
- [33] L.E.Scriven. MRS Online Proceedings Library (OPL), 121, 717.**1988**.
- [34] M.Biswas, P.C.Su. Modern technologies for creating the thin-film systems and coatings.2017.
- [35] L.Li, C.Xu, Y.Zhao, K.Ziegler. J.Advances in Condensed Matter Physics. 903294: 1-6.**2014**.
- [36] N.M.Ndamitso, A.S.Abdulkareem, J.O.Tijani. **2020**.
- [37] M.Zhou. Doctoral dissertation, Université Montpellier.**2015**.
- [38] A.Fujishima, X.Zhang, D.A.Tryk. Surface science reports, 63(12), 515-582.**2008**.
- [39] R.Katal, S.P.Masudy, M.Tanhaei, M.H.D.A.Farahani, H.Jiangyong. Chemical Engineering Journal, 384, 123384.**2020**.
- [40] V.Shklover, M.K.Nazeeruddin, S.M.Zakeeruddin, C.Barbe, A.Kay, T.Haibach, M. Grätzel. Chemistry of materials, 9(2), 430-439.**1997**.
- [41] R.Hengerer, B.Bolliger, M.Erbudak. M.Grätzel. Surface science, 460(1-3), 162-169.**2000**.
- [42] S.F.Shaikh, B.G.Ghule, U.T.Nakate, P.V.Shinde, S.U.Ekar, C.O'Dwyer, R.S.Mane. Scientific Reports, 8(1), 11016.**2018**.
- [43] M.Gopal, W.J.M.Chan, L.C.D.Jonghe, L. C. Journal of Materials Science, 32, 6001-6008.**1997**.
- [44] M.Ramamoorthy, D.Vanderbilt, R.D.King-Smith. Physical Review B, 49(23), 16721.**1994**.
- [45] A.Beltran, L. Gracia, J. Andres. The Journal of Physical Chemistry B, 110(46), 23417-23423.**2006**.
- [46] M.Gartner, A.Szekeres, H.Stroescu, D.Mitrea, M.Covei. Molecules, 28(23), 7828.**2023**.

- [47] A.Kaur, A.Umar, S.K.Kansal. Journal of colloid and interface science, 459, 257-263.**2015**.
- [48] M.K.Nowotny, T.Bak, J.Nowotny. The Journal of Physical Chemistry B, 110(33), 16270-16282.**2006**.
- [49] J.Nowotny, T.Bak, M.K.Nowotny, L.R.Sheppard. International journal of hydrogen energy, 32(14), 2630-2643.**2007**.
- [50] https://www.safefoodadvocacy.eu/wp-content/uploads/2022/06/Press-release_E171.pdf
- [51] Z.A.Lewicka, W.Y.William, B.L.Oliva, E.Q.Contreras, V.L.Colvin. Journal of Photochemistry and Photobiology A: Chemistry, 263, 24-33.**2013**.
- [52] H.J.Leong, S.G.Oh. Journal of Industrial and Engineering Chemistry, 66, 242-247.**2018**.
- [53] Innovative Applications of Titanium Dioxide in Ceramics" in Ceramics International
- [54] R.K.Sonker, S.R.Shabajet, R.Johari, B.Yadav. Gas Sensors, 81.**2019**.
- [55] H.Park, Y.Park, W.Kim, W.Choi. Journal of Photochemistry and Photobiology C: Photochemistry Reviews, 15, 1-20.**2013**.
- [56] J.L.G.Fierro. CRC press.**2005**.
- [57] L.W.Tack, M.A.Azam, R.N.A.R.Seman. The Journal of Physical Chemistry A, 121(13), 2636-2642.**2017**.
- [58] S.F.Zheng, J.S.Hu, L.S.Zhong, W.G.Song, L.J.Wan, Y.G.Guo. Chemistry of Materials, 20(11), 3617-3622.**2008**.
- [59] K.Frikha. Doctoral dissertation, Université de Haute Alsace-Mulhouse.**2020**.
- [60] J.V.Hernandez. Doctoral dissertation, Le Mans Université.**2017**.
- [61] C.Habis. Doctoral dissertation, Université de Lorraine.**2022**.
- [62] E.Muchuweni, T.S.Sathiaraj, H.Nyakoty. Heliyon, 3(4). **2017**.
- [63] F.P.Koffyberg, F.A.Benko. Journal of Applied Physics, 53(2), 1173-1177.**1982**.
- [64] D.C.Reynolds. Applied Physics Letters, 75, 2594-2596.**1999**.
- [65] B.D.Cullity, S.R.Stock. Prentice Hall.**2001**.
- [66] C.Klingshirn. Chem Phys Chem, 8, 782-803.**2007**.
- [67] L.Zhang. ZnO nanostructures for dye-sensitized solar cells. Advanced Materials, 20, 4253-4268.**2008**.

- [68] T.Yamamoto. Dover Publications.**2002.**
- [69] Z.L.Wang. Journal of Physics: Condensed Matter, 16, R829.**2004.**
- [70] D.C.Look. Materials Science and Engineering: B, 80, 383-387.**2001.**
- [71] M.I.Khan, S.Imran, M.Saleem, S.U.Rehman. Results in physics, 8, 249-252.**2018.**
- [72] Y.Ku, Y.H.Huang, Y.C.Chou. Journal of Molecular Catalysis A: Chemical, 342, 18-22.**2011.**
- [73] N.M.Arifin, F.Mohamad, R.Hussin, A.Z.M.Ismail, S.A.Ramli, N.Ahmad, M.Izaki, Journal of Sol-Gel Science and Technology, 100, 224-231. **2021.**
- [74] S.Pitchaiya, N.Eswaramoorthy, M.Natarajan, A.Santhanam, V.M.Ramakrishnan, V.Asokan, D.Velauthapillai. New Journal of Chemistry, 44(20), 8422-8433.**2020.**
- [75] V.J.Garcia, C.M. Pelicano, H.Yanagi. Thin Solid Films, 662, 70-75.**2018.**
- [76] S.Sundar, G.Venkatachalam, S.J.Kwon. Nanomaterials, 8(10), 823.**2018.**
- [77] G.Papadimitropoulos, N.Vourdas, V.E.Vamvakas, D.Davazoglou. In journal of physics: conference series (Vol. 10, No. 1, p. 182). IOP Publishing.**2005.**
- [78] F.P.Koffyberg, F.A.Benko. Journal of Applied Physics, 53(2), 1173-1177.**1982.**
- [79] M.Aronniemi, J.Lahtinen, P.Hautojärvi. Journal devoted to the development and application of techniques for the analysis of surfaces, interfaces and thin films, 36(8), 1004-1006.**2004.**
- [80] J.D.Uribe, J.Osorio, C.A.Barrero, D.Girata, A.L.Morales, A.Hoffmann. Microelectronics Journal, 39(11), 1391-1393.**2008.**
- [81] M.Seki. Iron Ores and Iron Oxide Materials, 255. **2018.**
- [82] M.Ismail. Doctoral dissertation, Institut National Polytechnique de Lorraine-INPL; Institut National des Sciences Appliquées et de Technologie.**2011.**
- [83] E.Deliantcourt. Doctoral dissertation, Université de Limoges.**2021.**
- [84] G.Huerta-Cuellar, R.Imani. Books on Demand.**2020.**
- [85] R.W.Boyd, A.L.Gaeta, E.Giese. Cham: Springer International Publishing.**2008.**
- [86] R.W.Boyd. journal of modern optics, 46(3), 367-378.**1999.**
- [87] Y.R.Shen. Principles of nonlinear optics.**1984.**
- [88] G.P.Agrawal. Heidelberg: Springer Berlin Heidelberg.**2000.**
- [89] G.P.Agrawal. JOSA B, 28(12), A1-A10.**2011.**

- [90] S.Q.Wersand. Doctoral dissertation, Université Paul Verlaine-Metz.**2006.**
- [91] G.He, S.H.Liu. Physics of nonlinear optics. World Scientific.**1999.**
- [92] S.Singh, N.Singh. progress in Electromagnetics Research, 73, 249-275.**2007.**
- [93] O.Aso, M.Tadakuma, S.Namiki. dEp, 1(2).**1999.**
- [94] G.Agrawal. Institute of Optics, University of Rochester, Rocheste, NY, United States.**2007.**
- [95] J.Zou. The University of Texas at Austin.**2004.**
- [96] H.R.Shanks, P.D.Maycock, P.H.Sidles, G.C.Danielson. Physical Review, 130(5), 1743.**1963.**
- [97] D. R. Lide. CRC Handbook of Chemistry and Physics, 91st Edition. Boca Raton, FL: CRC Press/Taylor and Francis, **2010.**
- [98] A.Tsogoo. Doctoral dissertation, Le Mans Université; Mongol Ulsyn Ih Surguul'(Ulaanbaatar)).**2023.**
- [99] A.A.Bunaciu, E.G.UdriŞTioiu, H.Y.Aboul-Enein. Critical reviews in analytical chemistry, 45(4), 289-299.**2015.**
- [100] N.Belhamra. Doctoral dissertation, Université Mohamed Khider Biskra.**2014.**
- [101] V.Dhiman, N.Kondal, P.Choudhary. Environmental Research, 216, 114751.**2023.**
- [102] A.Monshi, M.R.Foroughi, M.R.Monshi. World journal of nano science and engineering, 2(3), 154-160.**2012.**
- [103] G.B. Williamson, R.C. Smallman. Mag. 1.34.**1956.**
- [104] R.S.Das, Y.K.Agrawal. Vibrational spectroscopy, 57(2), 163-176.**2011.**
- [105] A.Shahmanesh. **2022.**
- [106] J.C.Manifacier, J.Gasiot, J.P.Fillard. Journal of Physics E: Scientific Instruments, 9(11), 1002.**1976.**
- [107] Direct and indirect band gap semiconductors.
<http://www.doitpoms.ac.uk/tlplib/semiconductors/direct.php> Copyright © 2004-2015 University of Cambridge].
- [108] R.A.Lance. **2018.**
- [109] E.S.Tüzemen, S.Eker, H.Kavak, R.Esen. Applied Surface Science, 255(12), 6195-6200.**2009.**
- [110] E.R.Shaaban, N.Afify, A.El-Taher. Journal of Alloys and Compounds, 482(1-2), 400-404.**2009.**

- [111] E.R.Shaaban, M.A.Rahman, M.T.Dessouky. *Thin Solid Films*, 515(7-8), 3810-3815. **2007**.
- [112] A.Dutta. *Spectroscopic methods for nanomaterials characterization*, 73-93. **2017**.
- [113] D.X.C.Tong, X.C.Tong. *Advanced Materials for Integrated Optical Waveguides*, 53-102. **2014**.
- [114] Y.C.Wu, M.V.Ibañez, C.L.Luyer, J.Shen, J.Mugnier. In *Optical Materials and Applications* (Vol. 5946, pp. 396-407). SPIE. **2006**.
- [115] M.A.Mutalib, M.A.Rahman, M.H.D.Othman, A.F.Ismail, J.Jaafar. In *Membrane characterization* (pp. 161-179). Elsevier. **2017**.
- [116] <https://www.nanoscience.com/techniques/scanning-electron-microscopy/>
- [117] N.Antonis. **2019**.
- [118] M.S.Anderson. *Biomicrofluidics*, 17(3). **2023**.
- [119] P.Eaton, P.West. Oxford university press. **2010**.
- [120] H.J.Butt, B.Cappella, M.Kappl. *Surface science reports*, 59(1-6), 1-152. **2005**.
- [121] L.Y.Qiao, F.Y.Xie, M.H.Xie, C.H.Gong, W.L.Wang, J.C.Gao. *Transactions of Nonferrous Metals Society of China*, 26(8), 2109-2116. **2016**.
- [122] I.N.Kuznetsova, V.Blaskov, I.Stambolova, L.Znaidi, A.Kanaev. *Materials Letters*, 59(29-30), 3820-3823. **2005**.
- [123] Y.S.Tamgadge, G.G.Muley, K.U.Deshmukh, V.G.Pahurkar. *Opt Mater* 86:185–190. **2018**.
- [124] S.M.El-Sheikh, G.Zhang, H.M.El-Hosainy, A.A.Ismail, K.E.O'Shea, P.Falaras, D.D.Dionysiou. *Journal of hazardous materials*, 280, 723-733. **2014**.
- [125] D.Nassoko, Y.F.Li, J.L.Li, X.Li, Y.Yu. *International Journal of Photoenergy*.**2012**.
- [126] A.Arunachalam, S.Dhanapandian, C.Manoharan, M.Bououdina, G.Ramalingam, M.Rajasekaran, A.M.Ibraheem. *Ceram Int* 42:11136–11149. **2016**.
- [127] T.Bo-Wen, N.Shan, S.Chuan, L.Zhi-Qiang, S.Xiao-hua, W.Shu. *Ferroelectrics* 549:96–103. **2019**.
- [128] M.Sreedhar, I.N.Reddy, C.V.Reddy, J.Shim. *Mater Sci Semicond Process* 85:113–121. **2018**.
- [129] A.Karthick, G.Umadevi, B.Baskar, A.S.Enigochitra.
- [130] K.Benzouai, M.Mahtali, Z.Daas, A.Bouabellou. *Optik* 229:166270. **2021**.
- [131] J.C.Manifacier, J.Gasiot, J.P.Fillard. *J. Phys. E* 9, 1002.**1976**.

- [132] S.A.Bhandarkar, A.Kompa, D.Kekuda, M.S.Murari, M.P.Telenkov, K.K.Nagaraja. *Surf Interfaces* 23:100910. **2021**.
- [133] A.Arunachalam, S.Dhanapandian, C.Manoharan, G.Sivakumar. *Spectrochim Acta Part A Mol Biomol Spectrosc* 138:105–112. **2015**.
- [134] T.C.Paul, J.Podder, M.H.Babu. *Surf Interfaces* 21:100725. **2020**.
- [135] L.P.R.Pala, V.Uday, D.Gogoi, N.R.Peela. *J Environ Chem Eng* 8:104267. **2020**.
- [136] Chukwuocha, E. O., Onyeaju, M. C., & Harry, T. S. (2012). Theoretical studies on the effect of confinement on quantum dots using the brus equation.
- [137] A.K.Shahi, B.K.Pandey, B.P.Singh, R.Gopal. *Adv Nat Sci Nanosci Nanotechnol* 7:035010. **2016**.
- [138] Brus. *J Phys Chem* 90:2555–2560. **1983**.
- [139] C.Kormann, D.W.Bahnemann, M.R.Hoffmann. *J Phys Chem* 92:5196–5201. **1988**.
- [140] R.Ulrich, R.Torge. *Appl Opt* 12:2901–2908. **1973**.
- [141] Z.Zhang, Q.I.Zhi-Mei. *J.Chin. J Anal Chem* 38:1538–1543. **2010**.
- [142] Y.C.Wu, M.V.Ibaez, C.LLuyer, J.Shen, J.Mugnier. In *Optical Materials and Applications* 5946: 396–407 SPIE. **2006**.
- [143] F.HANINI. Doctoral dissertation, Thèse de Doctorat, Université Constantine 1. **2014**.
- [144] A.V.E.Khomchenko. Elsevier Academic Press, Amsterdam. **2005**.
- [145] L.Martinu, D.Poitras. *J Vac Sci Technol A: Vac, Surf, Films* 18:2619–2645. **2000**.
- [146] S.J.Darzi, A.R.Mahjoub, A.Nilchi. *Phys E Low Dimens Syst Nanostruct* 42:176–181. **2009**.
- [147] T.Touam, L.Znaidi, D.Vrel, N.I.Kuznetsova, O.Brinza, A.Fischer, A.Boudrioua. *Coatings* 3:49–58. **2013**.
- [148] Y.Bouachiba, A.Taabouche, A.Bouabellou, A.M.Zemieche, N.Ghellil, H.Serrar, C.Boukentoucha. *Semiconductors* 55:S72–S79. **2021**.
- [149] P.Herve, L.K.J.Vandamme. *Infrared Phys Technol* 35:609–615. **1994**.
- [150] T.S.Moss. *Phys Status Solidi (b)* 131:415–427. **1985**.
- [151] R.R.Reddy, Y.N.Ahammed. *Infrared Phys Technol* 36:825–830. **1995**.
- [152] N.M.Ravindra, S.Auluck, V.K.Srswastava. *Phys Stat Sol (b)* 93:K155–K160. **1979**.
- [153] F.Naccarato, F.Ricci, J.Suntivich, G.Hautier, L.Wirtz, G.M.Rignanese. *Phys Rev Mater* 3:044602. **2019**.
- [154] F.Hanini, Y.Bouachiba, F.Kermiche, A.Taabouche, A.Bouabellou, T.Kerdja, K.Boukheddaden. *Int J Nanopart* 11:132–142. **2013**.

- [155] S.Khodja, T.Touam, A.Chelouche, F.Boudjouan, D.Djouadi, Z.Hadjoub, A.Boudrioua. *Superlattices Microstruct* 75:485–495. **2014**.
- [156] H.G.Tompkins, W.A.McGahan, New York. **1999**.
- [157] A.Martnez, Juan. *Appl Opt* 39:4557–4568. **2000**.
- [158] J.Fick, B.Ménaert, J.Zaccaro, P.Moretti. *Opt Commun* 270.2:229–232. **2007**.
- [159] E.Auguściuk. In *Laser Technology 2012: Progress in Lasers* 8702: 21–26. SPIE. **2013**.
- [160] U.Selvaraj, A.V.Prasadarao, S.Komarneni, R.Roy. *J Am Ceram Soc* 75:1167–1170. **1992**.
- [161] L.E.Regalado, D.Malacara. Chapter *Isotropic Amorphous Optical Materials*; 1st edn. CRC Press. **2001**.
- [162] J.F.Xu, Z.Ji, W.X.Shen, Z.S.Li, S.H.Tang, X.R.Ye, X.Q.Xin. *Journal of Raman spectroscopy*, 30(5), 413-415. **1999**.
- [163] R.Mechiakh, N.B.Sedrine, M.Karyaoui, R.Chtourou. *Applied surface science*, 257(13), 5529-5534. **2011**.
- [164] M.Schumm. Doctoral dissertation, Universität Würzburg. **2008**.
- [165] R.F.Zhuo, H.T.Feng, Q.Liang, J.Z.Liu, J.T.Chen, D.Yan, G.H.Yue. *Journal of Physics D: Applied Physics*, 41(18), 185405. **2008**.
- [166] W.Wang, Q.Zhou, X.Fei, Y.He, P.Zhang, G.Zhang, . W.Xie. *CrystEngComm*, 12(7), 2232-2237. **2010**.
- [167] N.Jayarambabu, B.S.Kumari, K.V.Rao, Y.T.Prabhu. *Int. J. Curr. Eng. Technol*, 4(5), 3411-3416. **2014**.
- [168] U.Vijayalakshmi, M.Chellappa, U.Anjaneyulu, G.Manivasagam, S.Sethu,. *Materials and Manufacturing Processes*, 31(1), 95-106. **2016**.
- [169] O.P.Keabadile, A.O.Aremu, S.E.Elugoke, O.E.Fayemi. *Nanomaterials*, 10(12), 2502. **2020**.
- [170] P.K.Raul, S.Senapati, A.K.Sahoo, I.M.Umlong, R.R.Devi, A.J.Thakur, V.Veer. *Rsc Advances*, 4(76), 40580-40587. **2014**.
- [171] N.M.Basith, J.J.Vijaya, L.J. Kennedy, M.Bououdina. *Materials science in semiconductor processing*, 17, 110-118. **2014**.
- [172] A.Drygała, Z.Starowicz, K.G.Ñeček, M.Karolus, M.Lipiński, P.Jarka, T.Tański. *Molecules*, 28(15), 5656. **2023**.